

**Naval Research Laboratory**

Washington, DC 20375-5320

**AD-A269 687**



NRL/FR/8105--93-9564

20000920218

## **Ultraviolet Plume Instrument Calibration and Sensor Assessment**

E. R. MALARET  
J. G. CARDON  
L. PEREZ  
H. W. SMATHERS  
D. M. HORAN

*SDI Office  
Space Systems Development Department*

September 1, 1993

**DTIC**  
**ELECTE**  
**SEP 22 1993**  
**S E D**

**Reproduced From  
Best Available Copy**

93 9 21 064

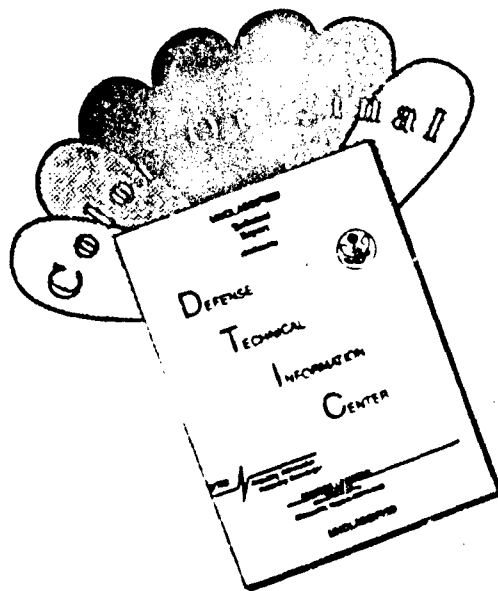
Approved for public release; distribution unlimited.

951  
950  
**93-21944**



116pg

# DISCLAIMER NOTICE



THIS DOCUMENT IS BEST QUALITY AVAILABLE. THE COPY FURNISHED TO DTIC CONTAINED A SIGNIFICANT NUMBER OF COLOR PAGES WHICH DO NOT REPRODUCE LEGIBLY ON BLACK AND WHITE MICROFICHE.

REPORT DOCUMENTATION PAGE			Form Approved OMB No. 0704-0188	
Public reporting burden for this collection of information is estimated to average 1 hour per response, including the time for reviewing instructions, searching existing data sources, gathering and maintaining the data needed, and completing and reviewing the collection of information. Send comments regarding this burden estimate or any other aspect of this collection of information, including suggestions for reducing this burden, to Washington Headquarters Services, Directorate for Information Operations and Reports, 1215 Jefferson Davis Highway, Suite 1204, Arlington, VA 22202-4302, and to the Office of Management and Budget, Paperwork Reduction Project (0704-0188), Washington, DC 20503.				
1. AGENCY USE ONLY (Leave Blank)	2. REPORT DATE  September 1, 1993	3. REPORT TYPE AND DATES COVERED  Interim		
4. TITLE AND SUBTITLE  Ultraviolet Plume Instrument Calibration and Sensor Assessment			5. FUNDING NUMBERS  PE-63217C PMA-N1305	
6. AUTHOR(S)  E. R. Malaret, J. G. Cardon, L. Perez, H. W. Smathers, and D. M. Horan				
7. PERFORMING ORGANIZATION NAME(S) AND ADDRESS(ES)  Naval Research Laboratory Washington, DC 20375-5320			8. PERFORMING ORGANIZATION REPORT NUMBER  NRL/FR/8105-93-9564	
9. SPONSORING/MONITORING AGENCY NAME(S) AND ADDRESS(ES)  Strategic Defense Initiative Organization SDIO/TND The Pentagon Washington, DC 20301-7100			10. SPONSORING/MONITORING AGENCY REPORT NUMBER	
11. SUPPLEMENTARY NOTES  Applied Coherent Technology Corp.				
12a. DISTRIBUTION/AVAILABILITY STATEMENT  Approved for public release; distribution unlimited.			12b. DISTRIBUTION CODE	
13. ABSTRACT (Maximum 200 words)  The Ultraviolet Plume Instrument (UVPI) is a calibrated, plume-tracking instrument flown on the Naval Research Laboratory's Low-power Atmospheric Compensation Experiment (LACE) satellite. The UVPI's primary mission was to collect images of rocket plumes in the ultraviolet wavelengths. The purpose of this report is to describe the procedures followed in calibrating the UVPI, to present final instrument response functions for use in subsequent data reduction and analysis, and to provide conversion constants useful for revising data values contained on delivered data tapes and in completed rocket plume reports.				
14. SUBJECT TERMS  LACE satellite      Ultraviolet plume instrument      UVPI Calibration plumes      Rocket plumes      Ultraviolet			15. NUMBER OF PAGES  126	
			16. PRICE CODE	
17. SECURITY CLASSIFICATION OF REPORT  UNCLASSIFIED	18. SECURITY CLASSIFICATION OF THIS PAGE  UNCLASSIFIED	19. SECURITY CLASSIFICATION OF ABSTRACT  UNCLASSIFIED	20. LIMITATION OF ABSTRACT  UL	

NSN 7540-01-280-5500

Standard Form 298 (Rev. 2-89)  
Prescribed by ANSI Std Z39-18  
283-102

## CONTENTS

EXECUTIVE SUMMARY .....	E-1
1. INTRODUCTION .....	1
1.1 Background .....	1
1.2 Sensor Head Description .....	3
1.3 UVPI Data Disposition .....	7
2. OVERVIEW OF UVPI DATA REDUCTION METHODOLOGY .....	7
2.1 Equivalent UVPI Imaging System Model .....	7
2.2 Simplified UVPI Data Reduction Model .....	9
3. NOISE CHARACTERIZATION .....	11
3.1 Signal-Independent Noise .....	11
3.2 Temporal Signal-Dependent Noise .....	53
4. UVPI SPATIAL RESOLUTION .....	54
4.1 Tracker Camera .....	54
4.2 Plume Camera .....	57
5. UVPI SENSOR RESPONSE .....	68
5.1 Laboratory and On-Orbit Measurements of the Gain Conversion Factor .....	69
5.2 Derivation of On-Orbit Net Quantum Efficiency Functions .....	77
5.3 UVPI Response Function Errors .....	88
5.4 Out-of-band Spectral Response .....	91
5.5 Noise Equivalent Radiance .....	94
5.6 Extraneous Signals .....	98
5.7 Response Transients .....	99
6. ON-ORBIT AND LABORATORY-MEASURED RESPONSE FUNCTIONS .....	102
6.1 History of Response Function Derivation .....	102
6.2 Comparison of Version 3 and Laboratory Calibration .....	107
6.3 Comparison of Version 3 and Version 2 Calibration .....	107
7. SUMMARY .....	114
REFERENCES .....	119
GLOSSARY .....	121



## EXECUTIVE SUMMARY

The Ultraviolet Plume Instrument (UVPI) is a calibrated, plume-tracking instrument flown on the Naval Research Laboratory's Low-power Atmospheric Compensation Experiment (LACE) satellite. The UVPI's primary mission was to collect images of rocket plumes in the ultraviolet wavelengths. Its secondary mission was to collect background image data of Earth, Earth's limb, and celestial objects in the near and middle ultraviolet wavebands. The UVPI successfully collected image data from four rocket launches, one ground burn of a rocket, and many background observations.

This report describes the procedures followed in calibrating the UVPI, presents final instrument response functions for use in subsequent data reduction and analysis, and provides conversion constants useful for revising data values contained on data tapes and in completed rocket plume reports.

Parameters and factors to convert UVPI data from digital numbers to photoevents are discussed. These include noise of various types, uniformity of response of the pixel array, and wavelength-independent terms such as gain conversion factors. This report also shows how little the calibration of the UVPI changed during more than two years of operation in space. Two multiplicative factors, one for each of the UVPI's cameras, are given for revising photoevent counts and rates contained on the delivered data tapes and in the rocket plume reports to base them on the final calibration values.

Wavelength-dependent factors such as the net quantum efficiency are also discussed, as well as their effect on radiometric values derived from photoevent counts based on earlier calibration values. Five multiplicative factors, one for the tracker camera and one for each of the four plume-camera filters, are given for revising radiometric values contained in the rocket-plume reports to base the reports on the final calibration values. These multiplicative factors range from 0.793 to 0.950. Application of these conversion factors does not change the trends and conclusions presented in the rocket-plume reports.

Major results are scattered throughout this report and may be difficult to separate from important, but secondary, results. Therefore, section 7 is a summary of primary results, including the final UVPI response functions, estimated errors in the final response functions, and the conversion constants to revise the existing data tapes and rocket-plume reports.

DTIC QUALITY INSPECTED 1

Accession For	
NTIS CRA&I	<input checked="" type="checkbox"/>
DTIC TAB	<input type="checkbox"/>
Unannounced	<input type="checkbox"/>
Justification _____	
By _____	
Distribution /	
Availability Codes	
Dist	Avail and/or Special
A-1	

# ULTRAVIOLET PLUME INSTRUMENT: CALIBRATION AND SENSOR ASSESSMENT

## 1. INTRODUCTION

### 1.1. Background

Since its launch on 14 February 1990, the Low-power Atmospheric Compensation Experiment (LACE) satellite has been used as a space-based platform from which numerous observations have been carried out using the onboard Ultraviolet Plume Instrument (UVPI).<sup>\*</sup> The satellite was designed and built by the Naval Research Laboratory (NRL) for the Strategic Defense Initiative Organization (SDIO). It was launched into a circular orbit of 292 nautical miles (nmi) altitude with an inclination of 43°. It is a gravity-gradient-stabilized satellite with attitude measurement accuracy of about 1°. Figure 1 is a schematic of the LACE satellite. The top boom extends to 150 ft and carries a 200-lb tip mass for gravity-gradient stabilization. The leading boom carries a retroreflector array. The bottom panels carry 210 electroptical sensors associated with the satellite's atmospheric compensation experiment. The UVPI is a pointable, telescopic instrument mounted internally and looking through an aperture on the Earth-facing side of the LACE spacecraft.

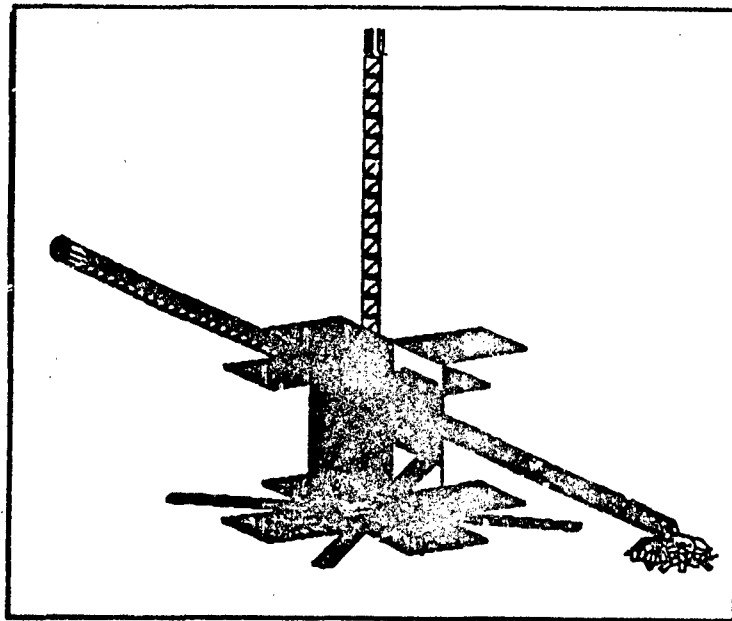


Fig. 1 - Schematic of LACE satellite

The UVPI's primary mission is to collect images of ultraviolet emission from rocket plumes. The UVPI telescope aperture is only 10 cm in diameter. However, it can detect and image missile plumes at 700 km range. The UVPI is typically used to observe missiles in flight above the atmosphere since stages of rockets fired at low altitude (below 40 km) are not expected to be visible in the ultraviolet from space. Rocket stages reaching 90 km altitude and greater have been successfully detected and tracked by

<sup>\*</sup> Manuscript approved April 21, 1993.

<sup>\*</sup> Glossary provided at end of text.

the UVPI at ranges from 450 to 700 km for about 30 s. Missile tracking in the ultraviolet is potentially advantageous because of extremely low Earth and solar backgrounds, extremely sensitive photodetectors that do not require cryogenic cooling, and very high optical resolution with optics of relatively modest size. Five rocket firings were successfully observed with UVPI.

The UVPI's secondary mission is to collect background image data of Earth, Earth's limb, and celestial objects in the near and middle ultraviolet wavebands. Background object imagery collected with the UVPI includes the day and night Earth limb air glow, aurora, sunlit and moonlit clouds, solid Earth scenes with varying solar illumination, cities, and stars.

The UVPI looks through a hole in the Earth-oriented panel. By use of an internal gimbaled mirror, the UVPI has a cone-shaped field of regard of  $\pm 50^\circ$  about the satellite's nadir. For nadir viewing, the door that covers the UVPI aperture is opened fully. Attached to the inside of this door is a flat mirror which, when the door is opened to about  $45^\circ$ , allows the UVPI cameras to view celestial objects or the Earth's limb. The hinge arrangement of the door constrains the limb viewing direction to within  $43^\circ$  of south.

The UVPI consists of two intensified charge-coupled device (CCD) cameras that are coaligned and share a Maksutov-Cassegrain telescope. The tracker camera has 17 times larger field of view than the plume camera and is used to locate, acquire, and track a target. The narrow field of view plume camera obtains high-resolution images of rocket plumes. The two cameras use narrowband filters and intensified charge-coupled devices (ICCDs) to observe sources in the near and middle ultraviolet. The primary function of the tracker camera, viewing over a relatively wide field of view ( $1.98^\circ$  by  $2.60^\circ$ ) and broad spectrum [225 to 450 nanometers (nm)], is to locate and track a target for higher resolution observation by the plume camera. The plume camera has a narrow field of view ( $0.184^\circ$  by  $0.137^\circ$ ) and observes sources through any of four filters with passbands of 195 to 295 nm, 220 to 320 nm, 235 to 350 nm, and 300 to 320 nm. Wavelengths shorter than 310 nm from high-altitude plumes are essentially invisible from the ground because of atmospheric absorption. Both the tracker camera and the plume camera can be operated in a mode where the transmitted field of view is restricted to the central 46%, vertically, and 36%, horizontally, of the full field of view, and the image rate is increased to 30 Hz instead of 5 Hz. The limiting resolution of the tracker camera is about 230  $\mu$ rad (rad) and that of the plume camera about 90  $\mu$ rad, which is equivalent at 500-km range to 115 m and 45 m, respectively.

The camera images are digitized and transmitted to the ground, or are recorded onboard for later transmission. The camera output is an analog signal that is read from the CCD chip as a sequence of interlaced image fields. The analog signal is immediately digitized and pairs of interlaced field readouts are summed to provide a digitized non-interlaced image frame once every 1/30 s. In normal mode, every sixth frame is sent to the ground in real time, or sent to a tape recorder and subsequently transmitted. The result is a sequence of images at a 5 Hz rate. Each image consists of an array of 251 by 240 8-bit numbers that measure the intensity distribution on the CCD sensor plane.

During each of the rocket plume observations, approximately 500 1/30th-second images of plume data were acquired using the four plume-camera filters. The tracking of the plumes was of sufficient quality to permit the superposition of images for plume radiance determination. Image superposition to enhance the signal level is needed for accurate radiometry because of the small telescope aperture. Typical UVPI background observations range from 3 to 10 minutes and usually included between 2,000 and 5,000 images. Data were channeled to the UVPI Mission Planning and Assessment Center in Alexandria, Virginia, for processing and evaluation. More than 200 observations were made in two years of operation. Data tapes are archived in the SDIO Background Data Center at NRL for further distribution.

The spectral radiance and spectral radiant intensities of the missile plumes were extracted from the plume images. The data reduction methodology for rocket plumes has been described [1] and is discussed further in this calibration report.

## 1.2. Sensor Head Description

The sensor head assembly (Fig. 2) houses the UVPI optical components and the two intensified video cameras. The two major sections are the optical bench and the gimbal frame. The optical bench contains the telescope, calibration lamp, tracker and plume cameras, power regulator, filter wheel for the plume camera, filter drive motor, plume-camera folding mirror, relay optics, beam splitter, and the filter for the tracker camera. The optical bench is attached to the gimbal frame that also accommodates the gimbals and resolvers, gimbaled mirror, gimbal caging mechanism, calibration mirror, the door, and the door drive motor.

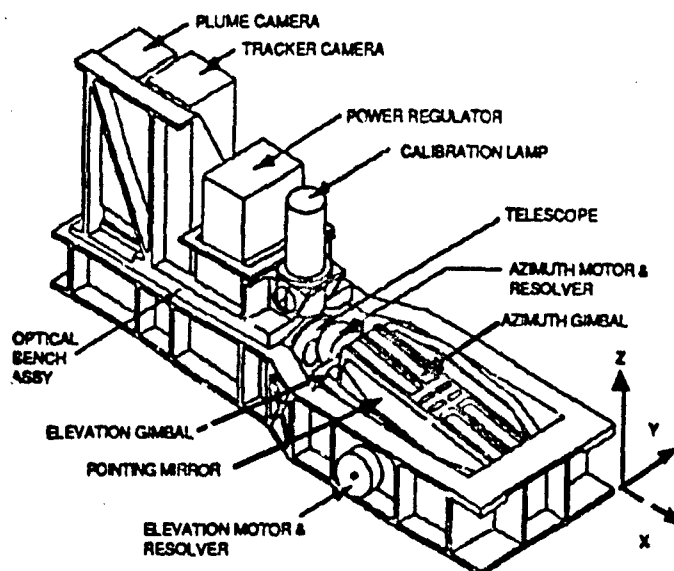


Fig. 2 - UVPI sensor head assembly diagram

The UVPI telescope (Fig. 3) is a Maksutov-Cassegrain configuration with a meniscal refracting corrector plate. The circular aperture is 10 cm in diameter, which provides a 78 cm<sup>2</sup> gross collecting area. A beam splitter allows the two cameras to share the beam and the forward telescope optics. The effective collecting area, which accounts for beam reduction caused by central blocking and the beam splitter, is used in calculating the net quantum efficiency. The focal length for the tracker camera is 60 cm, which gives an  $f$  number of 6 and a field of view of 2.60° by 1.98°. The plume camera uses a relay lens of magnification 10.3, which provides a focal length of 600 cm, an  $f$  number of 60, and a field of view of 0.184° by 0.137°. Table 1 shows the bandpass limits  $\lambda_1$  and  $\lambda_2$  for the camera filters.

The intensified cameras shown in Fig. 4 consist of an image intensifier followed by a fiber-optic reducer and a CCD television camera. The intensifiers, which were made by ITT, convert incoming ultraviolet-wavelength photons into outgoing green-wavelength photons, giving a large increase in intensity while preserving the spatial characteristics of the image.

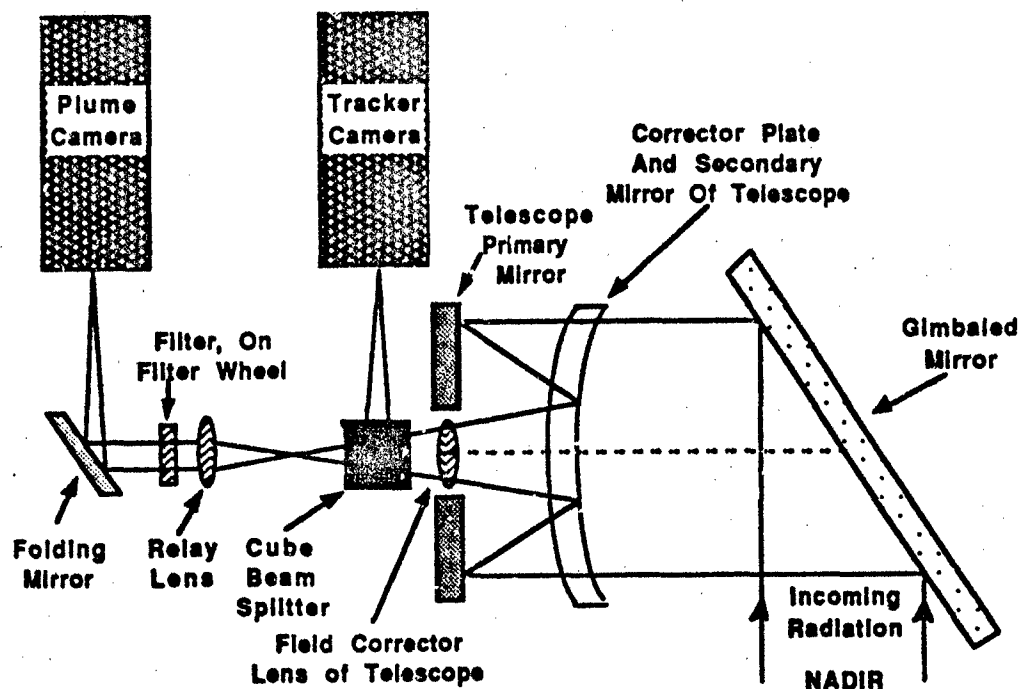


Fig. 3 - UVPI sensor head assembly optics

Table 1 - Camera Filter Bandpasses

Camera/Filter	$\lambda_1$ (nm)	$\lambda_2$ (nm)	$\lambda_2 - \lambda_1$ (nm)	FWHM (nm)
Plume PC-1	220	320	100	25
Plume PC-2	300	320	20	10
Plume PC-3	195	295	100	50
Plume PC-4	235	350	115	56
Tracker	255	450	195	150

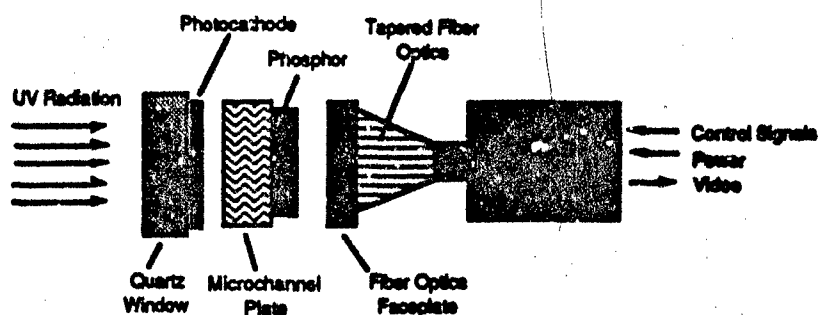


Fig. 4 - Schematic of intensified CCD camera

The intensifier is a vacuum-sealed cylinder containing circular quartz windows in front and back. The photocathode material, which converts incoming ultraviolet-wavelength photons to electrons, is a semi-transparent coating on the inside of the front window. The plume-camera intensifier uses a circular cesium-telluride photocathode with a 25-mm effective diameter. The tracker-camera intensifier uses a circular bialkali photocathode with a 40-mm effective diameter. The P20 phosphor, which converts electrons to green-wavelength photons, is a coating on the inside of the back window. A photoelectron is multiplied as it passes from front to back through a dual-chevron microchannel plate (MCP) that has electron gains of approximately  $10^5$  at high gain settings. The electron energy is increased by another factor of 100 by the phosphor's anode potential. The overall net gain provides about  $10^7$  green-wavelength photons per photoevent at high gain.

The tapered fiber optic reduces the size of the image to match the intensifier output to the CCD chip input. There are some light losses in the fiber-optic coupling. The CCD chip is a Texas Instrument 241C with a well-transfer function of  $1.2 \mu\text{V}/\text{electron}$  and an approximate photoelectric efficiency for green-wavelength photons of 50%. The result is a signal of about 1.5 V in the central pixel and lesser voltage in the surrounding 8 pixels associated with a single photoevent.

For purposes of providing a simplified model of operation for calibration, the optical path of each camera system can be divided into two parts. The first part consists of the telescope, a bandpass filter to select the observation wavelength, and the photocathode of the image intensifier. For the plume camera, one of four bandpass filters can be selected and the photocathode material is CsTe. For the tracker camera, only one bandpass filter is available and the photocathode material is bialkali. The second part of each camera system consists of the remaining elements of the image intensifier: the fiber-optic reducer, the CCD, and the electronics, which convert the pixel response to a digital number. The gain of each image intensifier is selectable, and the exposure time of the tracker camera is selectable by strobing the intensifier high voltage. The overall response of the UVPI cameras can be divided into the gains of the two parts described above.

The first component of the response for each camera is the photoefficiency, or net quantum efficiency, which is the probability that a photon incident on the UVPI telescope will produce a photoevent (PE). A photoevent is defined as a photoelectron produced at the photocathode that is collected and amplified by the MCP yielding a photoevent in the CCD. This component of the response is wavelength-dependent. It includes primarily the filter bandpasses but also includes the wavelength dependence of the optics and photocathodes. The collection efficiency of the MCP, approximately 60%, is incorporated into this component.

The second component of the response for each camera is the amplification of each photoelectron into volts per pixel of the CCD, i.e. the conversion ratio between photoevents and the digital number reported by the CCD control electronics. It is this digital number that is reported for each pixel in the telemetry stream. This component is not wavelength-dependent and takes into account MCP gain, phosphor, and CCD efficiencies.

Camera control is provided by a physically separate module called the Camera Frame Controller (CFC). The CFC provides automatic gain control of the exposure of each camera, normal/zoom image rate selection, plume-to-tracker ratio selection, camera telemetry data generation for post-mission reconstruction of the acquired images, filter wheel control, door position control, calibration lamp on/off control, gimbal cage/uncage control, and status data to telemetry. Horizontal and vertical control signals are supplied to both cameras by the CFC for synchronization, and the CFC receives their RS-170 output signal.

The received analog video signals are restored, multiplexed, digitized, and summed by internal CFC circuits. Each field consists of 754 by 240 pixels. The fields from the tracker camera are sent to the tracker electronics at a 60 Hz rate. To form plume- or tracker-camera images for telemetering or onboard storage, three pixels are averaged to form a superpixel, and two fields are then averaged. The result is the 251 vertical by 240 horizontal array of pixels at 30 Hz. The tracker camera's video signal is also buffered and made available to the tracker electronics for target centroid calculations and for determination of the gimbaled mirror pointing commands. Camera telemetry data from the CFC and engineering telemetry data from the electronics interface assembly are added to the digitized video frames and telemetered by the LACE spacecraft for later analysis.

The characteristics of the UVPI have been previously reported [2-3]. Table 2 provides a brief summary of the sensor characteristics.

Table 2 - Instrument Characteristics Summary

Parameter	Tracker Camera	Plume Camera
Shared telescope type	Maksutov-Cassegrain	Maksutov-Cassegrain
Telescope diameter	10 cm	10 cm
Focal length	60 cm	600 cm
Field of view	2.60° x 1.98°	.184° x .137°
Field of regard	100° x 97°	100° x 97°
Field of view per pixel	180.5 x 143.9 $\mu$ rad	12.8 x 10.0 $\mu$ rad
Pixel footprint @ 500 km	90 x 72 m	6.4 x 5.0 m
System resolution (FWHM)	220 to 250 $\mu$ rad	80 to 100 $\mu$ rad
Spectral region	225 - 450 nm	195 - 350 nm
Number of filters	1	4
Photocathode material	Bialkali	CsTe
Time for filter change	n/a	1.5 s
Digitization	8 bits/pixel	8 bits/pixel
Digital data rate	2.5 Mbps	2.5 Mbps
Image rate: Normal	5 per s	5 per s
Zoom*	30 per s	30 per s
Pixels: Normal	251 x 240	251 x 240
Zoom*	91 x 112	91 x 112
Pixel exposure time	.16 to 33.3 ms	33 ms
Frames integrated	n/a	1-6
Exposure range	>10 <sup>6</sup>	>10 <sup>6</sup>
Noise-equivalent radiance	See Section 5.5 for detailed discussion. NER depends on gain setting and filter selected.	

\*Reduced field of view.

### 1.3. UVPI Data Disposition

Data from all UVPI observations have been processed by the NRL LACE Program and deposited in the SDIO Backgrounds Data Center at NRL. Copies of the UVPI data can be obtained by contacting:

Backgrounds Data Center  
Code 7604  
Naval Research Laboratory  
Washington, D.C. 20375-5352

Phone: (202) 767-1760

Data from the four rocket plume observations has also been processed by the NRL LACE Program and deposited in the SDIO Plumes Data Center at Arnold Air Force Base in Tullahoma, Tennessee.

## 2. OVERVIEW OF UVPI DATA REDUCTION METHODOLOGY

The UVPI is an intensified CCD camera system designed to image tracked targets in the 195 to 450 nm wavelength range. UVPI collects rocket-plume data in the form of digitized images. The method used in the reduction of UVPI images implies a stochastic system model that describes how the continuous spatial, temporal, and spectral signal is sampled to discrete values or digital numbers (DN). This section provides a system-level model of UVPI as an imaging system. This is followed by an overview of the data reduction process used.

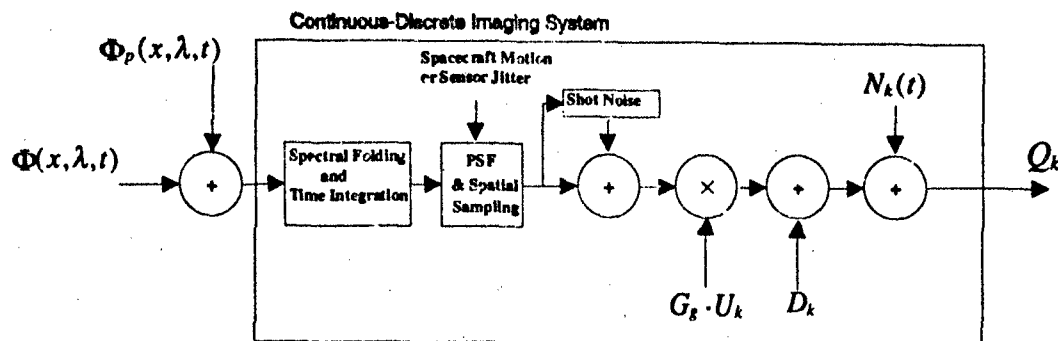
### 2.1. Equivalent UVPI Imaging System Model

Figure 5 is a simplified block diagram of the signal path in the UVPI imaging system. This type of diagram illustrates how the inherent signal from the object or scene of interest and background signal information are modified by different sources of noise present in the imaging system. These noise sources show up in the measured image as point degradations and spatial degradations. In this diagram the signal flows from left to right. This model is an equivalent imaging model since similar sources of image degradation, such as spatial blurring of the signal, are lumped together at one point in the model. A brief description of this diagram is in order.

#### *Spectral Folding*

Consider two additive sources of average spectral irradiance at the entrance of the UVPI sensor pupil. The first source is the spectral irradiance coming from the object under observation, for example, a rocket plume. The second source is the spectral irradiance not related to the object or scene under observation, e.g., background clutter. The goal is to determine the radiometric and spatial characteristics of the object of interest, independent of the background clutter. Immediately after passing through the sensor pupil, the combined spectral signal flows into the spectral filter block. At this point the signal is folded with the active UVPI spectral filter and integrated in time. The spectral folding equates to performing a weighted spectral integral of the signal with the net quantum efficiency of the active filter. The spectral response functions for the plume and tracker cameras are discussed in Section 5.





#### Legend:

- $\Phi(x, \lambda, t)$  spectral irradiance at sensor pupil coming from object under observation,
- $\Phi_p(x, \lambda, t)$  spectral irradiance at sensor pupil not related to object under observation,
- $G_s$  conversion constant, digital numbers per photoevent,
- $U_k$  detector nonuniformity at the  $k$ th pixel location,
- $D_k$  fixed pattern dark field at the  $k$ th pixel location,
- $N_k(t)$  temporal noise sources (zero mean), e.g., thermal and quantization (A/D),
- $Q_k$  discrete output in digital numbers (DN) at pixel location  $k$ .

Fig. 5 - Simplified block diagram of signal path in the UVPI

#### Spatial Degradations

Following the signal flow in Fig. 5, the signal is convolved with the equivalent system-level point spread function (PSF) and spatially sampled over a rectangular lattice. The UVPI point spread function is defined as the response of the UVPI cameras to a point source, e.g. a star or a ground beacon. It effectively changes the spatial frequency content of the image from that of the original signal, e.g. blurring of the observed data occurs, resulting in a loss of image fidelity. The PSF is closely related to the system modulation transfer function (MTF). For UVPI the spatial degradations are primarily introduced by diffraction-limited properties of optical elements, bandwidth limitations and transients in the electronic components, sensor jitter, and gimbal angle changes within the focal plane array (FPA) integration time. Section 5 presents quantitative information related to the UVPI PSF. Based on in-flight analysis, it is reasonable to model the UVPI PSF as a space invariant function.

#### Point Degradations

Point degradations affect only individual image points (pixels). Typical sources of this type of noise are shot noise, quantization noise, and thermal noise.

Shot noise is an additive noise that is signal-level dependent. In this equivalent model, the output of this stage, after the shot noise is added, results in a signal with a Poisson distribution with a mean equal to the mean number of photoevents observed and a standard deviation proportional to the square root of the mean of photoevents observed. Section 3 discusses the noise contributions to the UVPI sensor output.

The next two stages in the equivalent model in Fig. 5 characterize the focal plane array (FPA) response under the assumption of no detector noise. The output of each pixel in the FPA can be modeled, within the dynamic range of the detector, as a linear response with a nonzero intercept as a function of signal level. Since not all the pixels in the FPA have exactly the same linear response, two matrices are used to characterize the FPA. The first matrix is the detector nonuniformity matrix  $U_k$ , which characterizes the response or slope associated with each pixel. The second matrix is the FPA dark field matrix  $D_k$ . This is equivalent to the response of each pixel when no input signal is present, i.e., the zero intercept. For any given observation, both of these matrices are considered to be fixed or deterministic in nature. Section 3 provides quantitative information on the dark field and nonuniformity matrices. The constant  $G_g$ , discussed in section 5, accounts for the conversion from photoevents to digital numbers.

Finally, a more realistic detector model is achieved by adding the thermal and quantization noise terms to the resulting signal on a pixel by pixel basis. These two noise sources are signal-level independent. Quantization noise is an equivalent noise introduced in the analog-to-digital (A/D) conversion process. It is normally modeled by a uniform distribution with zero mean and standard deviation of  $1/12$ . Thermal noise is modeled by a Gaussian distribution with zero mean and a standard deviation that is temperature dependent. In actual practice, thermal and quantization noise are observed simultaneously. Therefore, empirical estimates of the combined noise sources can be obtained during dark field estimates.

In summary, the output of the image formation process corresponds to measurements of the image intensity over a lattice grid. Unfortunately, because of the inherent spatial and point degradations in the system, the output of this process is more accurately modeled as the sampled output of a linear system plus additive noise. The next section discusses the steps taken to remove all the deterministic transformations to which the original irradiance signal is subjected.

## 2.2. Simplified UVPI Data Reduction Model

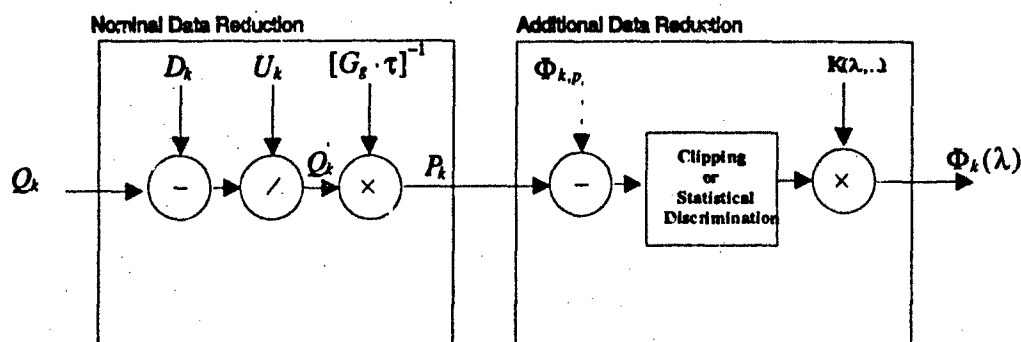
Figure 6 is a block diagram showing the basic sequence of data reduction steps used to recover the original source irradiance for each UVPI image. There are two major blocks in this diagram: nominal data reduction and additional data reduction. A brief description of this diagram is in order.

### Nominal Data Reduction

For nominal data reduction, digital numbers received from the satellite in the form of 8 bits/pixel are converted to counts of photoevents/s-pixel. In this process, all the nonrandom transformations introduced into the original signal are removed except the blurring introduced by the PSF. The signal transformations in this block have the following simple mathematical expression

$$\frac{P_k}{\tau} = \frac{1}{\tau \cdot G_g} \cdot Q_k = \frac{1}{\tau \cdot G_g} \cdot \left[ \frac{Q_k - D_k}{U_k} \right] \quad (\text{photoevents/second}). \quad (1)$$

The first stage in the data reduction process is to subtract an estimate of the deterministic dark field matrix. If the signal level is low at any given pixel, it is possible that a negative number results after the dark field subtraction is performed for that pixel. This is primarily caused, as discussed in the previous section, by the presence of additive noise in the signal. Section 3 discusses the method used to estimate dark field matrices.



**Legend:**

- $Q_k$  discrete output in digital numbers (DN) at pixel location  $k$ ,  
 $D_k$  estimated fixed pattern dark field at the  $k$ th pixel location,  
 $U_k$  estimated detector nonuniformity at the  $k$ th pixel location,  
 $\bar{Q}_k$  normalized digital number, with background subtracted and nonuniformity correction,  
 $[G_s \cdot \tau]^{-1}$  converts from digital numbers to photoevents/second,  
 $P_k$  estimated number of photoevents/second at the  $k$ th pixel location,  
 $\Phi_{k,p}$  estimated spectral irradiance contribution on  $k$ th pixel, not related to object under observation  
 $\Phi_k(\lambda)$  estimated spectral irradiance contribution on  $k$ th pixel, coming from object under observation  
 $K(\lambda, \dots)$  reference spectrum, known or assumed.

Fig. 6 - Simplified UVPI data reduction block diagram

The second stage is to normalize every pixel by the estimate of the nonuniformity matrix. Section 3 discusses the procedure used to estimate the nonuniformity matrices.

The estimation of both the dark field matrix and the nonuniformity matrix are critical for obtaining accurate, unbiased estimates of the signal. If the estimate of the dark field matrix is in error by a constant value, a bias will be obtained on every pixel.

The normalization of the data by  $G_s \tau$  converts the resulting image to units of photoevents/s-pixel. Section 5 discusses how the gain conversion factor  $G_s$  has been estimated and validated by using inflight calibration star observations.

**Additional Reduction for the Extraction of Radiance Values**

Additional data reduction can be performed to obtain accurate radiometric numbers.

The first stage in the additional data reduction process is to remove any remaining bias that is detected in regions where it is known that no signal should be present. If detected, the bias level is estimated and removed from every pixel in the image. If no superposition of frames is to be performed, the next stage is to perform an optional clipping of the data to suppress any readout of negative number of photoevents/s-pixel. Finally, given a reference spectrum, an estimate of the spectral irradiance can be obtained.

By registering, if necessary, and then summing consecutive images resulting from this processing stage, an increase in signal-to-noise ratio (SNR)/pixel can be achieved. No attempt is being made at the present time to remove from the measured images any of the spatial blurring introduced by the UVPI PSF.

### 3. NOISE CHARACTERIZATION

Analysis of UVPI data and accurate prediction of instrument sensitivity limits requires a thorough characterization of each of the noise components present in the digitized output of the instrument. Here, noise is defined as all components or statistical variation of the readout pixel values or spatial pattern arising from the detection process or detector electronics alone, and not directly from the mean value or variations in the irradiance of the scene of interest. These noise contributions lead to fluctuations in the pixel values, even in the case of temporally constant, flat-field irradiance at the input aperture. For discussion, the noise components are grouped into three major categories: signal-independent fixed pattern, signal-independent temporal, and signal-dependent temporal. Representative measurements are presented below for each.

#### 3.1. Signal-Independent Noise

Signal-independent noise is present in the digitized output of the instrument at all times, independent of any radiation incident on the telescope aperture. There are several sources of signal-independent noise, all of which must be taken into account in the calibration process. In practice, fixed-pattern signal-independent "dark frames" are subtracted from each frame of raw data on a pixel-by-pixel basis, and fixed-pattern signal-independent "nonuniformity" matrices are applied to account for pixel-to-pixel variations in responsivity. The temporal signal-independent noise is measured by determining the frame-to-frame variation of dark frames. The dark frame mean value can be accurately determined by averaging over a large number of frames. Spatial variation in the responsivity of the pixels is measured while viewing a spatially uniform, or flat-field scene. Results are presented demonstrating that the flat-field response of the instrument has not changed significantly during the first two years of the mission.

##### *Fixed-Pattern Dark Field Matrices*

Dark field pixel values used for calibration include dark current and electronic bias contributions. Accurate determination of these mean values for each pixel is essential to the calibration process. The mean values have been found to vary slightly from pass to pass and, to a lesser extent, during a single pass. The mean values also depend on gain step. Good estimates of the mean values and their variations for the fixed-pattern dark field matrices are of great importance for observations that do not include a dark field measurement.

Dark current, i.e., electrons collected in the CCD when no signal is incident on the sensor system, are generated in the photocathode, MCP, phosphor, and CCD. The largest contribution is expected from

thermal emission of electrons from the photocathode, especially from the tracker camera's bialkali photocathode. At high MCP gains, a single dark current electron released from the photocathode results in a bright image at the CCD, and the sum of values from all the pixels in the image is the same as that for a single photoevent.

The largest contribution to the dark frame pixel values is an intentionally applied bias in the readout electronics. This bias is not affected by MCP gain step but does have a slight dependence on pass-specific parameters such as temperature. The combination of this bias and the dark current provides the total signal-independent fixed-pattern dark frame pixel values subtracted from images during calibration.

Figures 7 and 8 show individual tracker- and plume-camera dark frame images, respectively, at low MCP gain; Figs. 9 and 10 show individual tracker- and plume-camera dark frames, respectively, at high MCP gain. The tracker-camera image at high gain clearly shows thermally generated dark current "events". No obvious dark current events are visible in the high-gain plume-camera image. A bad pixel slightly to the right of center in the plume-camera image is visible at both low and high gain.

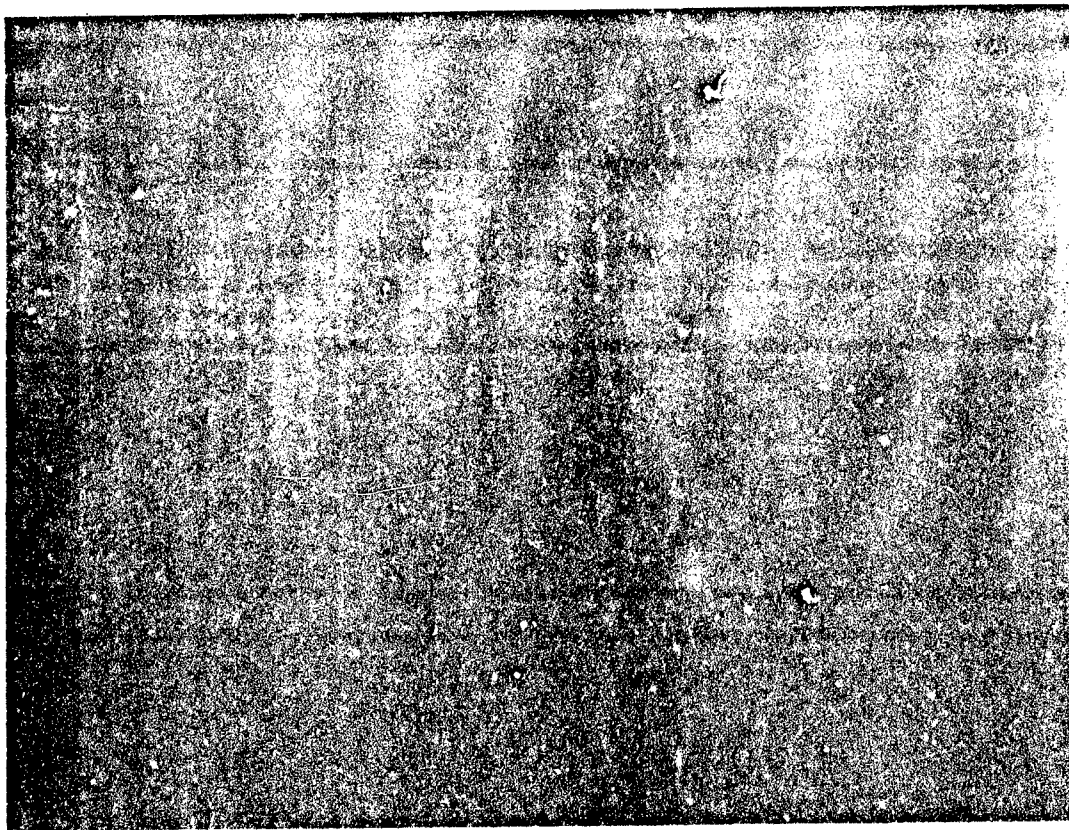


Fig. 7 - Tracker-camera dark frame at low MCP gain



Fig. 8 - Plume-camera dark frame at low MCP gain

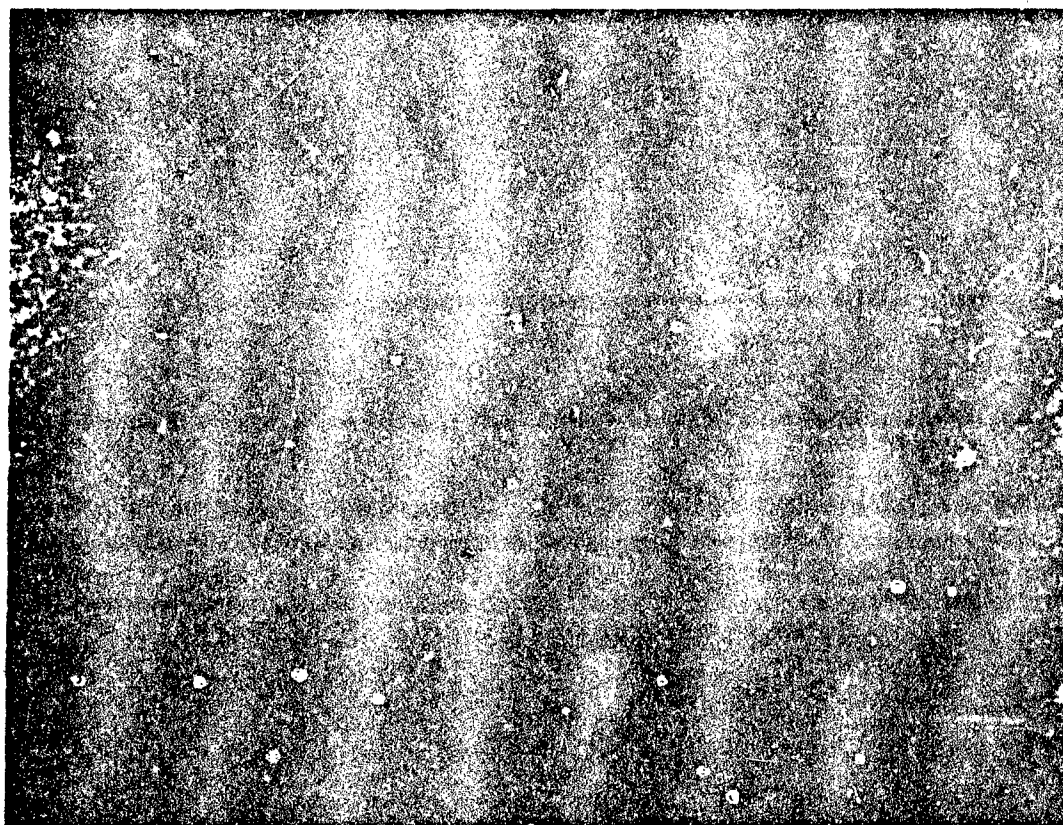


Fig. 9 - Tracker-camera dark frame at high MCP gain



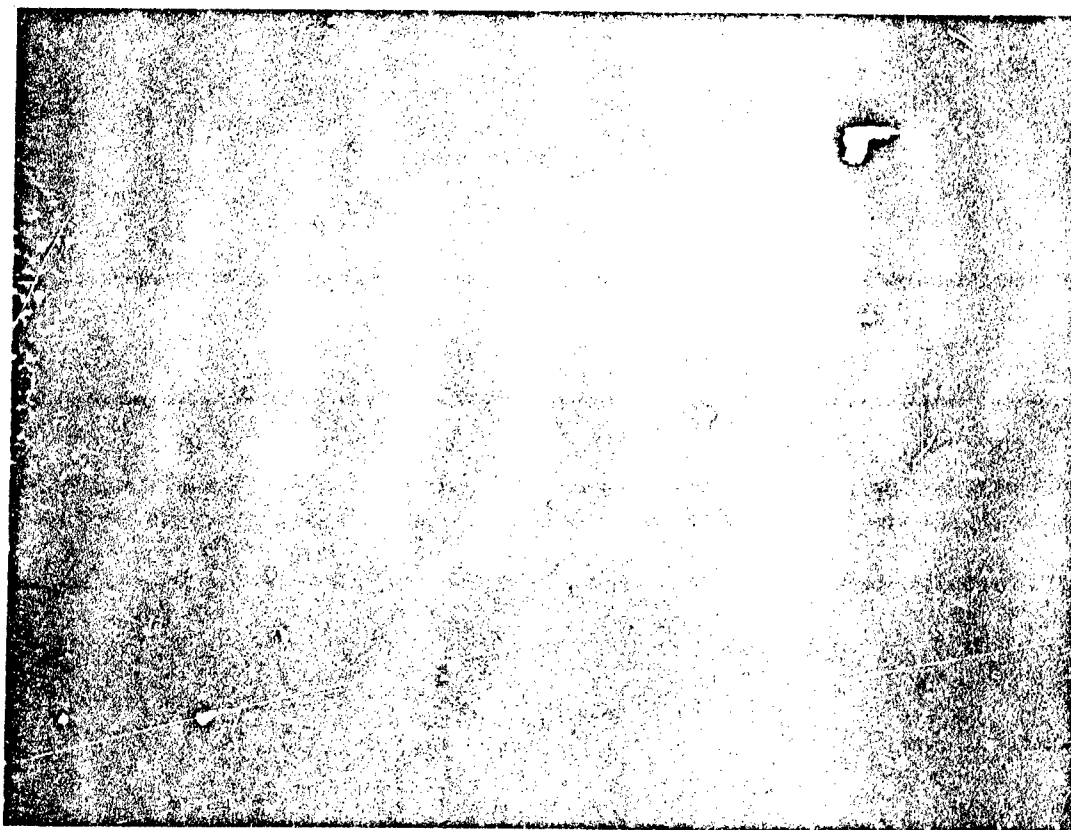


Fig. 10 - Plume-camera dark frame at high MCP gain



Several dark frames can be averaged temporally to obtain estimates of the dark frame temporal mean, Eq. (2), and temporal standard deviation, Eq. (3):

$$D_k = \frac{1}{N} \sum_{n=1}^N Q(\bar{x}_k, t_n) \quad (\text{DN}) \quad (2)$$

and

$$\sigma_{D_k} = \sqrt{\left[ \frac{1}{N} \sum_{n=1}^N Q^2(\bar{x}_k, t_n) \right] - \left[ \frac{1}{N} \sum_{n=1}^N Q(\bar{x}_k, t_n) \right]^2} \quad (\text{DN}). \quad (3)$$

Here,  $\bar{x}_k$  is the coordinate of pixel  $k$  in the image plane,  $N$  is the number of frames used for frame averaging, and  $Q(\bar{x}_k, t_n)$  is the measured UVPI scene pixel values (8 bits/pix) at time  $t_n$  from pixel  $k$ .

It is possible to determine the necessary number of images  $N$  to get an adequate estimate of the mean dark field value for each pixel. It is known from the law of large numbers and the Tchebycheff inequality [4] that given a random variable with mean  $\mu$  and variance  $\sigma^2$ , the probability that the absolute error in the mean estimate be greater than  $\epsilon$  obeys the inequality

$$\text{Probability } (|\hat{\mu}_N - \mu| \geq \epsilon) \leq \frac{\sigma^2}{N\epsilon^2} \quad (4)$$

In our case,  $\hat{\mu}_N$  is the tracker- or plume-camera dark frame sample mean value estimate  $\mu$  is the true mean value,  $\epsilon$  is some value greater than zero,  $\sigma$  is the camera dark frame standard deviation, and  $N$  is the number of frames used for the estimation.

Tables 3 and 4 show how large the number of frames  $N$  should be in order that  $\text{Prob}(|\hat{\mu}_N - \mu| \geq \epsilon)$  is less than or equal to 0.01, 0.05 and 0.1 as a function of  $\epsilon$ . The value of  $\epsilon$  is set to some multiple of the quantization noise, 0.29 DN. The value of  $\sigma$  is set to the spatial mean of the temporal standard deviation. Note that  $N$  is directly proportional to  $\sigma^2$ , and inversely proportional to  $\epsilon^2$ . Typically, 100 frames of plume and tracker data are used to generate dark field matrices, leading to a standard error  $\sigma/\sqrt{N}$  which is approximately 1% of the mean value.

The spatial mean of the temporal mean values is

$$\bar{D} = \frac{1}{M} \sum_{k=1}^M D_k \quad (\text{DN}) \quad (5)$$

where  $k$  indexes each of the  $M$  pixels on the focal plane. Tables 5 and 6 list the spatial mean of the temporal mean values for groups of frames from a single observation at several MCP gain steps. The tracker camera mean values for this particular pass were unusually high, but the gain dependence is typical. Figures 11 and 12 show the results graphically. The larger means at higher gain steps are caused by dark current.

A study of the dark frame mean values for several observations has shown that there is a variation from pass to pass. The variation is small, on the order of 0.12 DN (1.4% of the mean) for the plume camera and 0.49 DN (2.5% of the mean) for the tracker camera.

Table 3 - Number of Frames Required for Tracker-Camera  
Dark Field Estimation

$P( \hat{\mu}_N - \mu  \geq \epsilon)$	$\epsilon(\text{DN})$	$N$
0.01	0.29	3111
	0.58	778
	0.87	346
	1.15	194
0.05	0.29	622
	0.58	156
	0.87	69
	1.15	39
0.10	0.29	311
	0.58	78
	0.87	35
	1.15	19

Table 4 - Number of Frames Required for Plume-Camera  
Dark Field Estimation

$P( \hat{\mu}_N - \mu  \geq \epsilon)$	$\epsilon(\text{DN})$	$N$
0.01	0.29	1587
	0.58	397
	0.87	176
	1.15	99
0.05	0.29	317
	0.58	79
	0.87	35
	1.15	20
0.10	0.29	159
	0.58	40
	0.87	18
	1.15	10

Table 5 - Example of Tracker-Camera Dark Frame Gain Dependence

Tracker Camera MCP Gain Step	Frames Used in Calculation	Spatial Mean of Temporal Mean (DN)	Spatial Mean of Temporal Std. Dev. (DN)
0	9	20.159	2.256
5	11	20.167	2.272
6	11	20.184	2.212
7	11	20.203	2.264
8	11	20.216	2.280
9	11	20.207	2.285
10	11	20.227	2.269
12	17	20.245	2.376
13	18	20.313	2.520
14	19	20.366	3.047
15	21	20.495	5.058

Table 6 - Example of Plume-Camera Dark Frame Gain Dependence

Plume Camera MCP Gain Step	Frames Used in Calculation	Spatial Mean of Temporal Mean (DN)	Spatial Mean of Temporal Std. Dev. (DN)
0	19	10.160	1.247
5	21	10.164	1.284
6	22	10.162	1.249
7	22	10.168	1.263
8	22	10.165	1.265
9	22	10.160	1.263
10	22	10.166	1.263
11	34	10.176	1.363
13	34	10.179	1.380
14	37	10.200	1.817
15	39	10.224	2.404

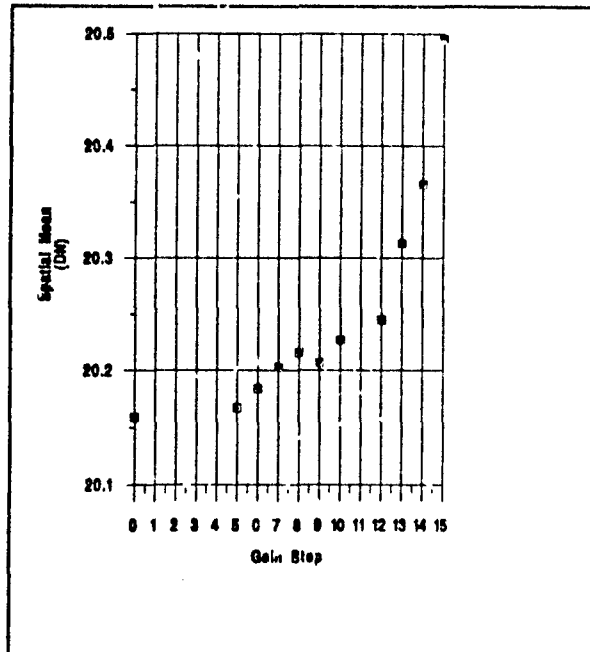


Fig. 11 - Example of tracker-camera dark field gain dependence

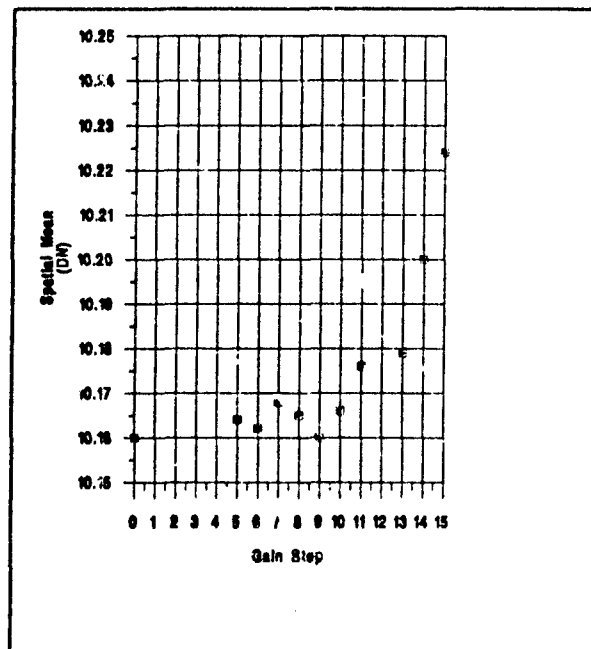


Fig. 12 - Example of plume-camera dark field gain dependence

Some of the earlier UVPI observations did not gather adequate dark field data and, therefore, must be calibrated using dark field estimates obtained from another observation. No repeatable method for theoretically predicting the dark frame mean value during a given pass has been developed. If an average dark field, based on data from many observations, is used as an estimate, the pass-to-pass dark field variations must be considered a source of error in the calibrated data. In most cases, the error is insignificant, since 0.12 DN (plume camera) and 0.49 DN (tracker camera) are very small compared with typical signals measuring 100 DN or more. Occasionally, the scene observed is of sufficiently low radiance that the error is significant.

Table 7 provides the mean and standard deviation of the spatial mean of the temporal mean for the plume and tracker cameras for dark field measurements during several observation passes. Also shown are the values for a single arbitrary pixel. The standard deviation, which is an estimate of the variation from pass to pass, is seen to be a small percentage of the mean value.

Table 7 - Dark Field Variations from Pass to Pass

Pass	Tracker-Camera Frames	Tracker-Camera Spatial Mean of Temporal Mean (DN)	Tracker-Camera Pixel (100,100) (DN)	Plume-Camera Frames	Plume-Camera Spatial Mean of Temporal Mean (DN)	Plume-Camera Pixel (100,100) (DN)
2076	32	20.25	20.97	32	9.22	9.28
5582	94	19.64	20.71	22	9.27	9.91
6786	105	19.67	20.26	104	9.33	9.63
6801	69	19.47	20.38	68	9.35	9.42
6816	115	19.62	20.07	115	9.26	9.55
7009	n/a	18.73	21.19	n/a	9.31	9.84
7024	96	19.28	22.05	91	9.36	9.92
7200	104	19.94	20.43	103	9.45	9.46
7215	88	19.57	20.18	49	9.32	9.55
7324	103	19.96	20.37	104	9.40	9.66
7338	123	19.70	19.87	122	9.42	9.71
7487	99	18.28	19.85	90	9.13	9.92
7502	103	18.28	19.08	102	9.24	9.98
7828	138	19.67	21.53	137	9.36	10.43
8172	100	19.47	20.51	100	9.15	9.34
8739	96	19.50	19.85	97	9.27	9.68
8754	122	19.46	20.07	121	9.27	9.46
9037	97	19.77	20.13	94	9.18	9.41
9329	44	19.50	20.61	45	8.97	9.71
9344	44	19.49	20.64	45	8.97	9.87
9547	116	19.97	20.78	243	9.27	9.50
9740	30	19.49	20.80	30	9.31	10.23
Mean:		19.49	20.47		9.26	9.70
Stdv:		0.49	0.63		0.12	0.29
Stdv/Mean:		2.51%	3.08%		1.35%	2.98%

In addition to changes in the dark field mean value from pass to pass, the spatial pattern has also been found to vary. To discount the possibility that changes in the spatial pattern are caused by different gain settings, an observation was made in which the door remained closed throughout the pass, and each of the tracker camera gain steps were used while collecting dark field data. The results are shown in Figs. 13 and 14. Clearly, the pattern changes very little, if any, with gain.

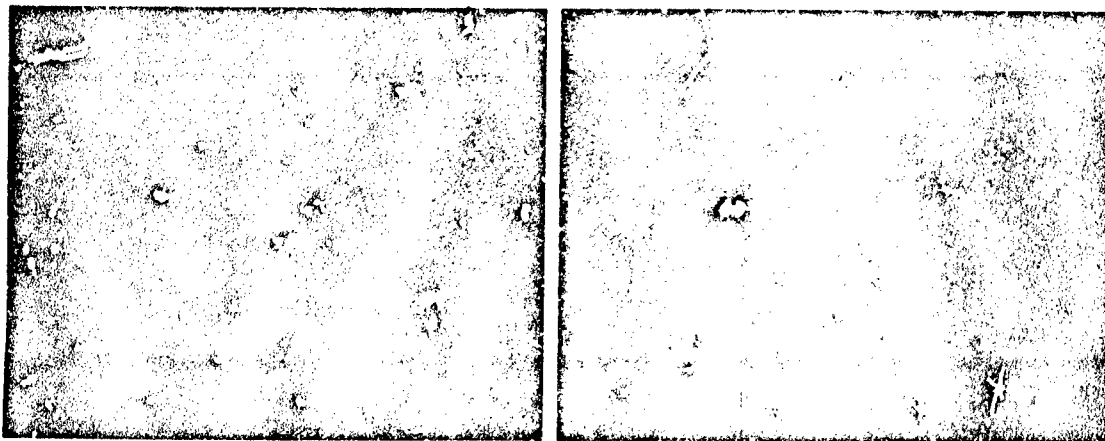


Fig. 13 - Tracker-camera dark field pattern for gain steps 0 and 15

Figures 15 and 16 show dark field spatial pattern variations from pass to pass for plume and tracker cameras, respectively. Relatively minor variations have been greatly overemphasized by scaling to the full intensity range of the video printer. No method for theoretically predicting the spatial pattern during a given pass has been developed.

Variations in the dark field mean value and spatial pattern have also been observed during single passes; Fig. 17 shows an example. The mean value measured in the tracker camera at the beginning of this pass (9695) differs from that measured at the end of the pass by only 0.13 DN. This change is small compared to tracker-camera pass-to-pass variations, 0.49 DN. To study the possible orbit-position dependence of the dark field measurements, an observation was made (10699) in which the instrument gathered dark field data periodically during two complete orbits. The cameras were left on for nearly three hours, and the tape recorder was turned on and off periodically. Figures 18 and 19 show that, as anticipated, the gain step 14 measurements have a higher mean value than do the gain step 1 measurements. The overall standard deviation during this observation was found to be 0.13 DN for the tracker camera and 0.03 DN for the plume camera.

Mean values in each camera were also plotted vs solar zenith angle at the spacecraft (Figs. 20 and 21). It appears that there is a correlation, especially at high gain, probably indicating that the UVPI door has a small light leak that is significant at high gain settings.

Since variations within a single pass are not large enough to account for all of the pass-to-pass variation, an observation was made to test for variations caused by the process of turning the instrument on and off. An observation (11026) of approximately 10 minutes was broken into 12 segments of approximately 30-s duration separated by short periods during which the instrument was turned off. The results are shown in Figs. 22 and 23 for the plume and tracker camera, respectively. Except for the low-DN transients measured as the gain stabilized immediately following instrument turn-on, the dark field mean values fall on a smoothly varying curve, with no erratic jumps. The jump in the tracker-camera mean values between frames 3000 and 4000 was caused by a change in gain from 0 to 13.



Fig. 14 - Tracker-camera dark field pattern for gain steps 1-14

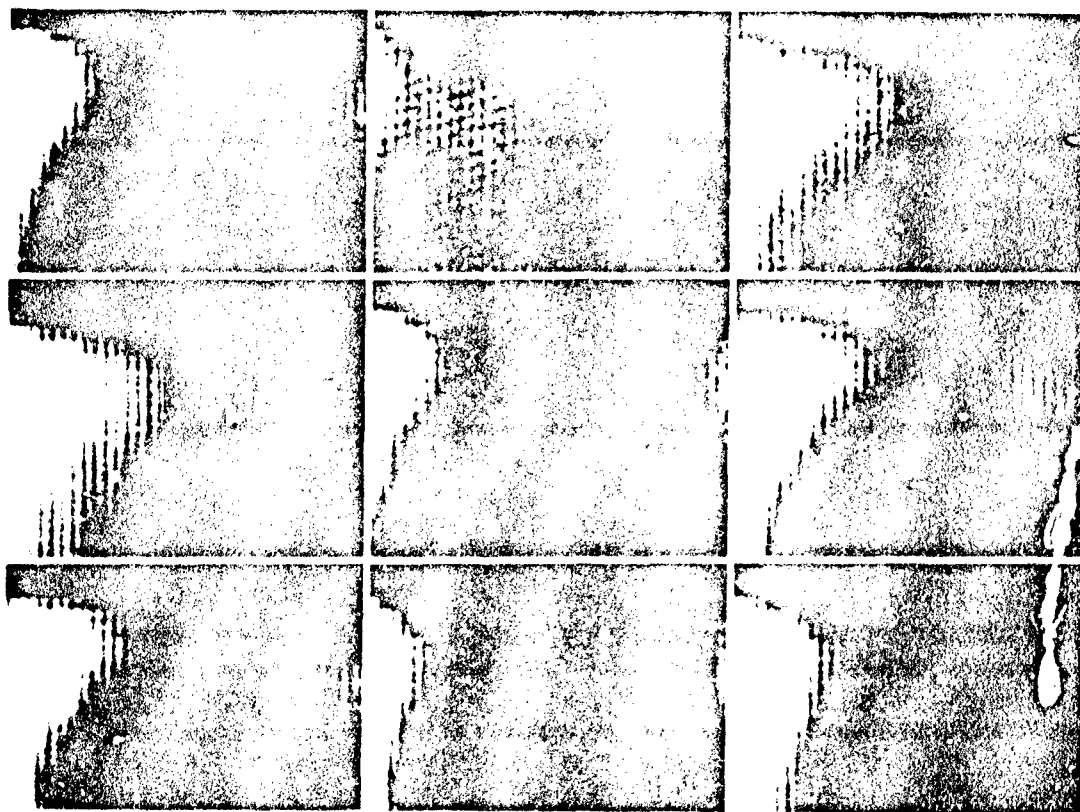


Fig. 15 - Plume-camera dark field spatial pattern variations from pass to pass



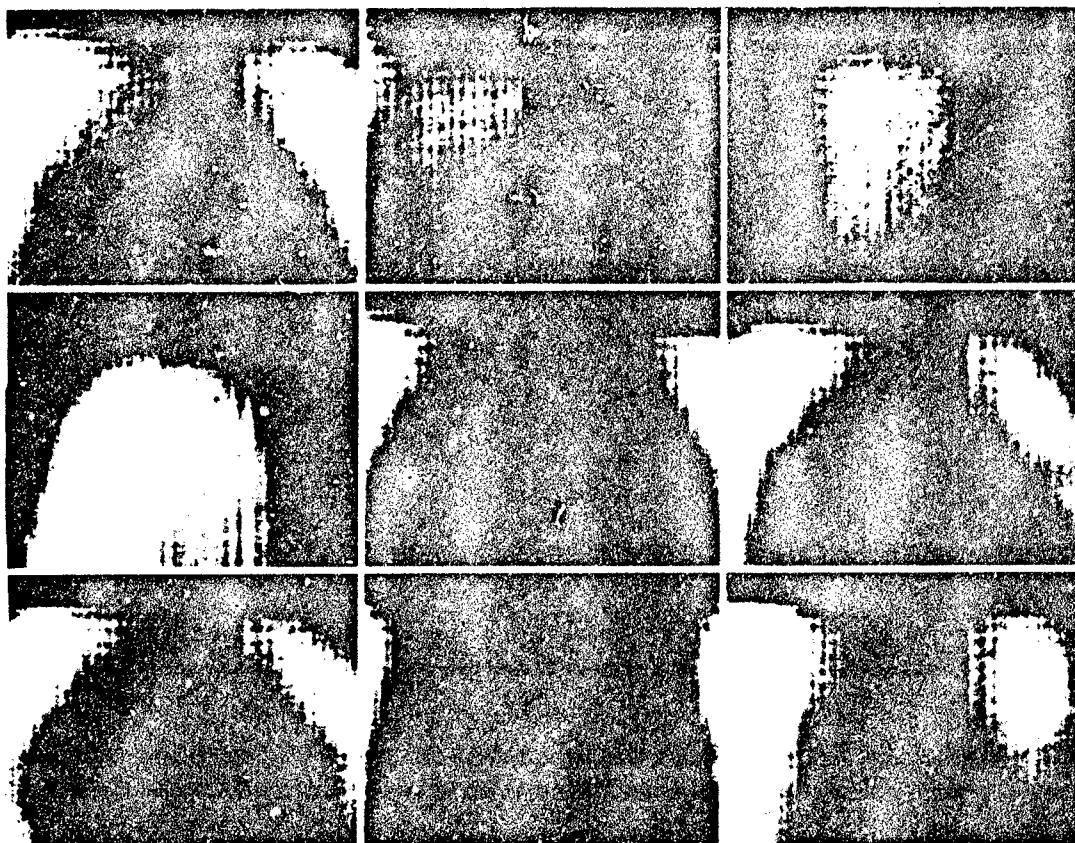


Fig. 16 - Tracker-camera dark field spatial pattern variations from pass to pass

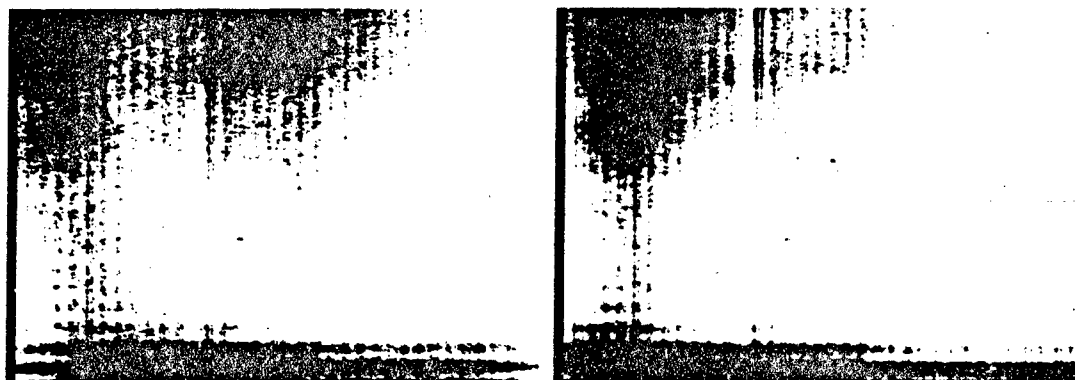


Fig. 17 - Tracker-camera dark field spatial variation during a single pass

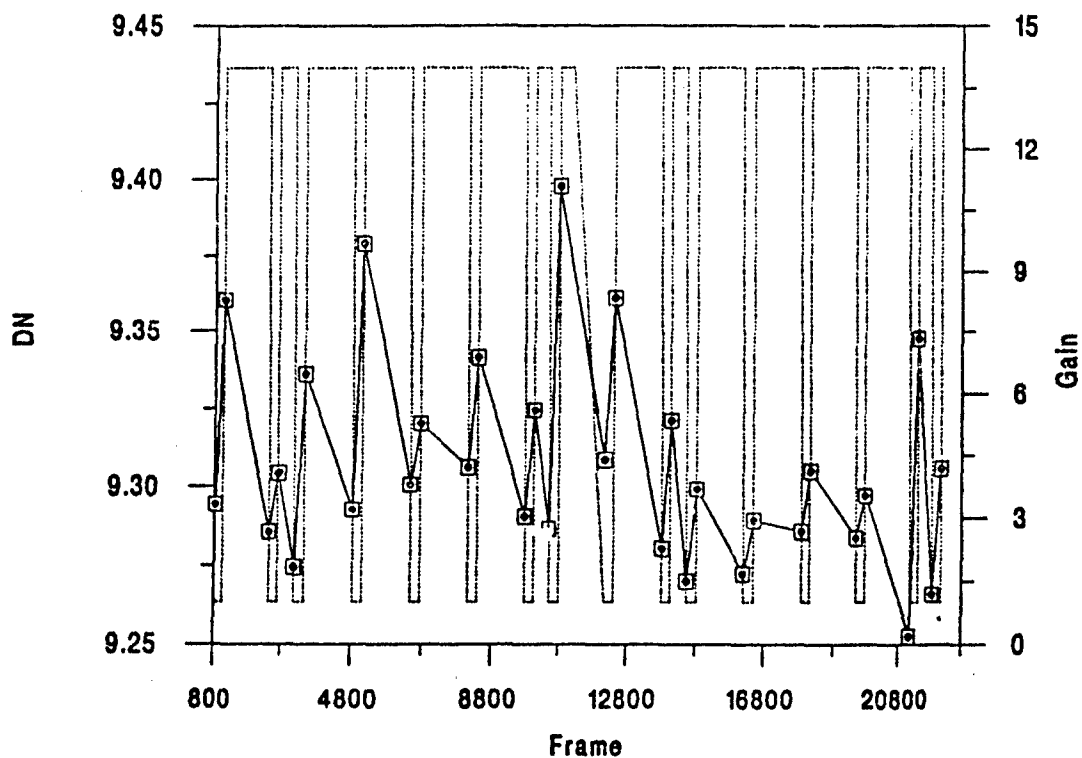


Fig. 18 - Plume-camera dark field mean values during pass 10699

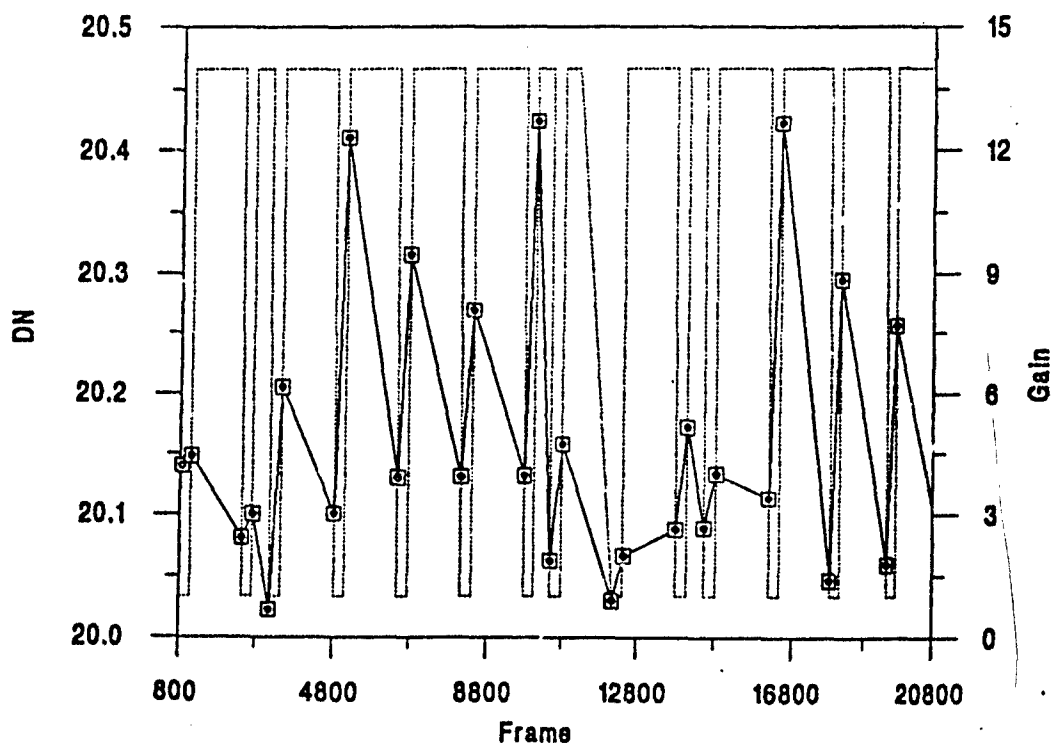


Fig. 19 - Tracker-camera dark field mean values during pass 10699

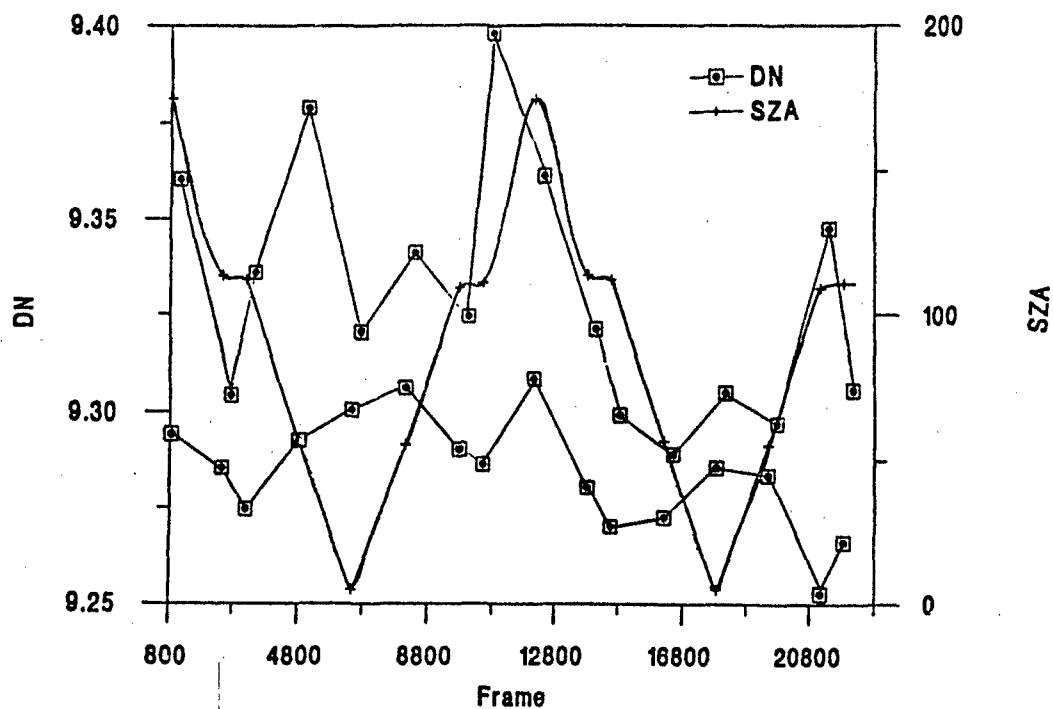


Fig. 20 - Plume-camera dark field dependence on solar zenith angle

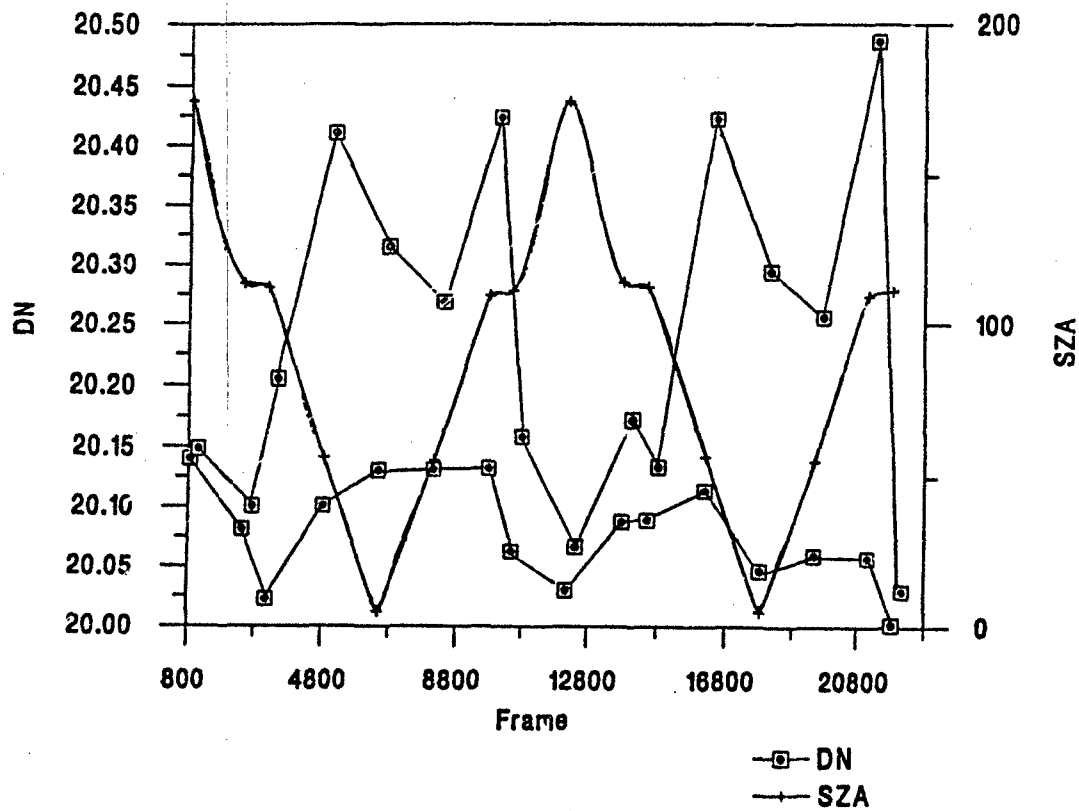


Fig. 21 - Tracker-camera dark field dependence on solar zenith angle

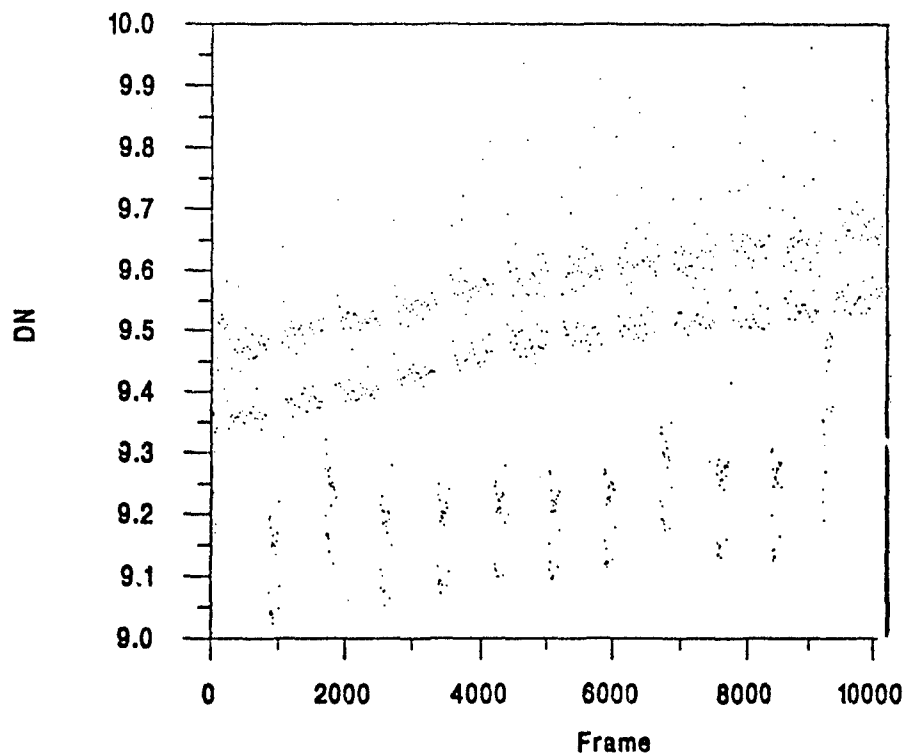


Fig. 22 - Plume-camera dark field during pass 11026

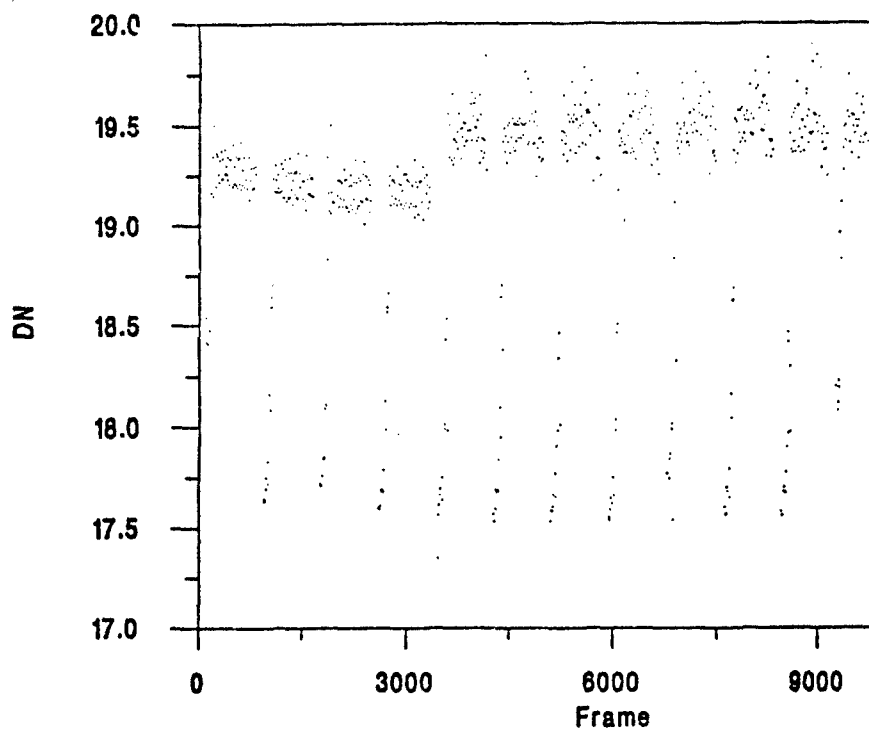


Fig. 23 - Tracker-camera dark field during pass 11026

Based on these and other observations, it appears that variations in the spacecraft lighting conditions and variations in the extent of light leakage, although significant, do not fully account for the pass-to-pass standard deviations of 0.12 DN for the plume camera and 0.49 DN for the tracker camera. In particular, the dark frame mean value for daytime passes is not consistently higher than that for nighttime passes, indicating that light leakage is not the primary contributor to pass-to-pass variations. Since the primary source of the variations is not understood, these variations must be treated as a systematic error in the calibration of a pass for which inadequate dark field data were gathered, and for which an estimated dark field is used. Table 8 summarizes the error, in units of photoevents/second based on the variation estimate of 0.12 DN for the plume camera and 0.49 DN for the tracker camera, for each of the plume- and tracker-camera gain steps. The tracker-camera values assume an integration time of 33.3 ms. Note that these errors apply only for those passes in which inadequate dark field data were gathered.

Table 8 - Estimated Error in Calibrated Data From Dark Field Uncertainty

Errors Applicable to Passes With Inadequate Dark Field Measurements		
Gain Step	Estimated Plume Camera 1s Error (PE/s)	Estimated Tracker Camera 1s Error (PE/s)*
0	$8.61 \times 10^1$	$6.68 \times 10^3$
1	$6.28 \times 10^1$	$3.48 \times 10^3$
2	$3.46 \times 10^1$	$1.61 \times 10^3$
3	$2.23 \times 10^1$	$7.63 \times 10^2$
4	$1.37 \times 10^1$	$3.65 \times 10^2$
5	6.17	$1.60 \times 10^2$
6	2.45	$8.52 \times 10^1$
7	1.02	$4.55 \times 10^1$
8	$4.54 \times 10^{-1}$	$2.08 \times 10^1$
9	$2.15 \times 10^{-1}$	$1.06 \times 10^1$
10	$1.00 \times 10^{-1}$	5.54
11	$5.86 \times 10^{-2}$	2.61
12	$3.00 \times 10^{-2}$	1.26
13	$1.62 \times 10^{-2}$	$5.00 \times 10^{-1}$
14	$1.05 \times 10^{-2}$	$2.80 \times 10^{-1}$
15	$7.96 \times 10^{-3}$	$1.06 \times 10^{-1}$

\*Assuming 33.3-ms integration time.

#### Fixed-Pattern Nonuniformity Matrices

The nonuniformity matrices used for calibration are a measure of the pixel-to-pixel variations in responsivity. The photocathode, spectral filters, MCP, phosphor, and CCD all contribute. Spatial variations in pixel responsivity are measured by irradiating the entire focal plane with a uniform intensity, or flat field. The resulting set of pixel values gives a measure of the relative response of each of the pixels in the focal plane array. Manufacturer's data indicate that each CCD pixel and each MCP channel has linear response over its operating range, i.e., the ratio of outputs (DN or electrons, respectively) for two measurements is equal to the ratio of inputs (irradiance or photoevents, respectively) for the two measurements. The automatic gain control (AGC) adjusts the MCP gain to keep the CCD in its operating range for a wide range of irradiances at the face of the UVPI telescope. Based on laboratory measurements and manufacturer's data, it is anticipated that the cameras will exhibit a fixed-pattern flat-field response over the range of irradiances anticipated during the mission. It has not been possible to verify the linearity of the response of each of the pixels [5] on-orbit for the full range of

observed scene irradiances because fixed-pattern flat-field response can only be measured accurately for very bright (sunlit) scenes. A variety of flat-field scenes observed on-orbit have produced nearly identical fixed-pattern images.

Flat-field irradiation was achieved both in the laboratory and in flight by locking straight down over the ocean during the daytime. Based on many observations using all four plume-camera filters, it is clear that spatial nonuniformities in the phosphor, MCP, photocathode, and CCD stay essentially constant throughout a given observation pass, and for all passes, but nonuniformities associated with the filters vary. These filter nonuniformities move with the filter wheel as it rotates between positions. Furthermore, once the filter wheel has moved either during a single pass or between passes, a return to a previously used filter position shows slight changes in the appearance of the nonuniformities.

The filter nonuniformities appear in flat-field images as dark spots that shift and spread or contract each time the filter wheel is rotated. The shifting and spreading indicates that the filter wheel is probably slightly loose in the plane normal to the optical axis. The result is that correction for these relatively minor blemishes is difficult or impossible, depending on the scene under observation. Near flat-field observations such as daytime nadir viewing over the ocean, land, or uniform clouds can often be corrected on a frame-by-frame basis. Less uniform sources, which do not show the filter nonuniformities clearly, may not be correctable. Figures 24 through 27 show flat-field data for all four plume-camera filters. Small variations in responsivity have been accentuated by using pseudo-color mapping. Filter-specific blemishes are numbered, and their approximate location and size are tabulated in Table 9.

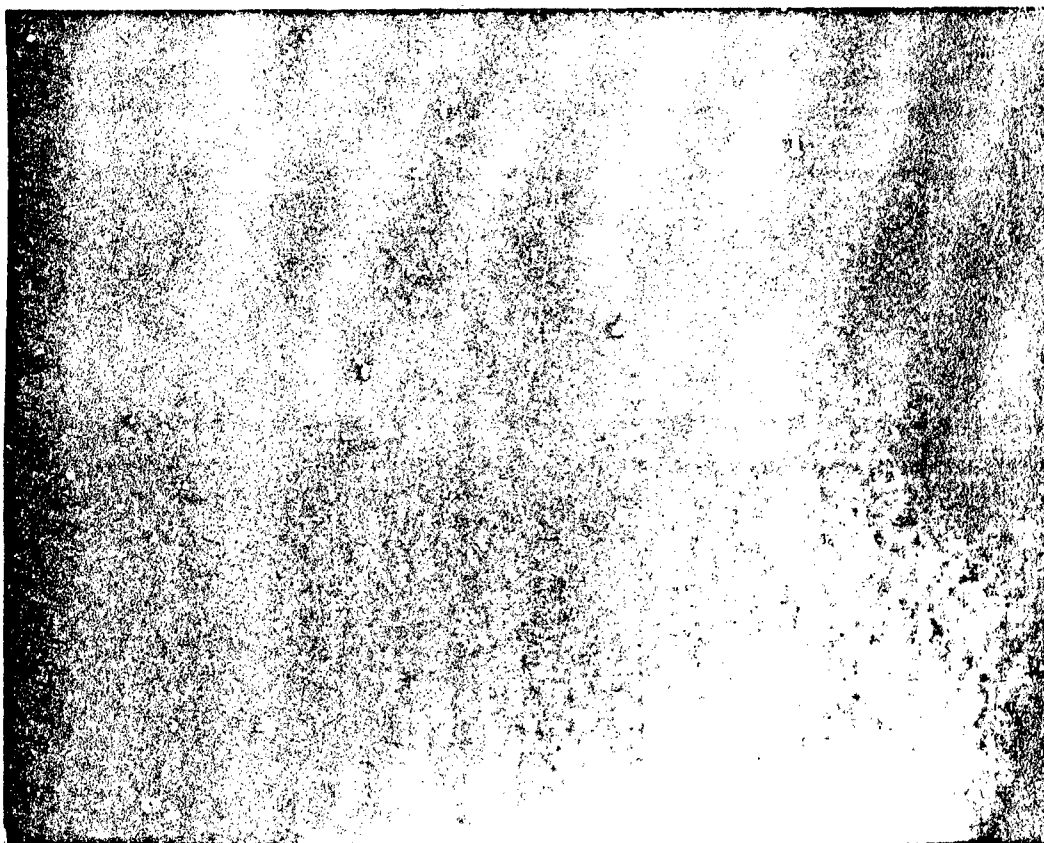


Fig. 24 - Plume-camera PC-1 flat-field response

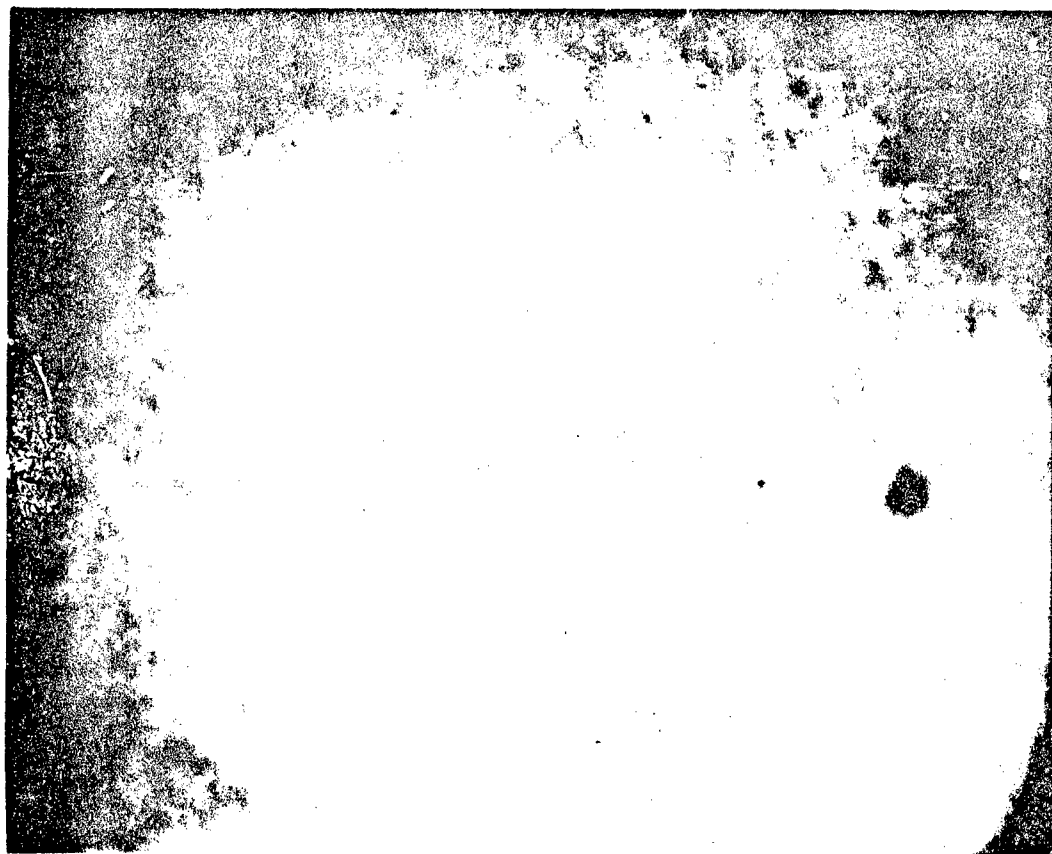


Fig. 25- Plume-camera PC-2 flat-field response

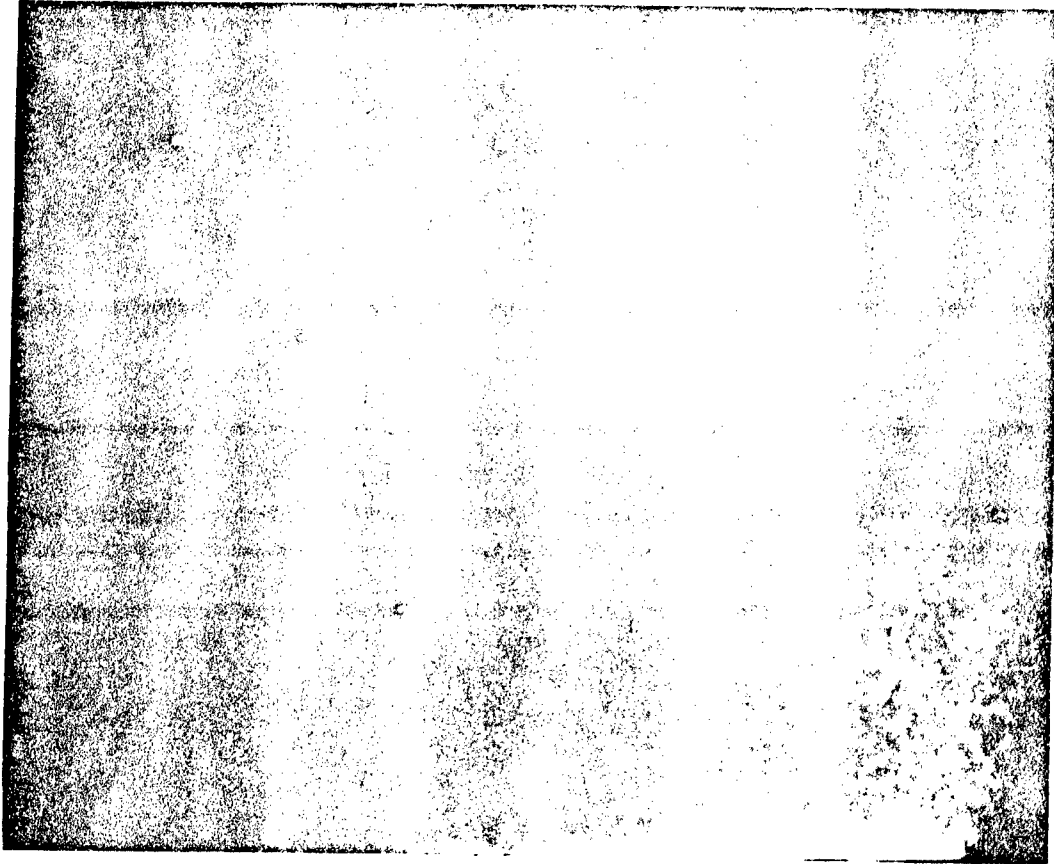


Fig. 26 - Plume-camera PC-3 flat-field response





Fig. 27- Plume-camera PC-4 flat-field response

Table 9 - Position and Size of Filter-Specific Blemishes

Spectral Filter	Blemish Number	Location of Center Pixel (Row, Col.)	Size
1	1	(38,204)	6 pixel radius
2	1	(134,214)	4 pixel radius
3	none		
4	1	(87,13)	4 x 5
	2	(101,29)	5 x 3
	3	(67,37)	5 x 4
	4	(79,49)	3 x 3
	5	(157,103)	3 x 3
	6	(125,113)	8 x 4
	7	(103,113)	4 x 2
	8	(147,175)	4 x 3
	9	(153,213)	5 x 3
	10	(157,237)	4 x 3

Excluding filter-specific blemishes, the plume-camera fixed-pattern response to flat-field irradiance has remained nearly constant throughout the mission. Figure 28 shows two flat-field images normalized to spatial mean value 1.0, recorded during passes 1606 (May 31, 1990) and 6994 (May 22, 1991). For comparison, Fig. 29 shows pass 1606 and pass 6994 images along the middle row of pixels. The two profiles are very similar except at the edge of the focal plane. Figure 30 shows the difference between the two normalized images; the color bar in the bottom left-hand corner shows the value associated with each color in the image. The only significant change between pass 1606 and pass 6994 is a shift in the PC-4 filter blemishes. Excluding the filter blemishes and edge effects, the differences are very small compared with the mean value (approximately 1.0) for each pixel. Similarly, Fig. 31 shows the difference between the pass 10175 and the pass 1606 normalized images. By chance, the filter blemishes are in nearly the same position in these matrices, resulting in differences that are very small compared to the mean pixel value. The bright band in the upper left-hand corner is positioned along the filter window edge.

Based on these results, a single nonuniformity matrix is used to calibrate all plume camera images. Filter-dependent blemishes, which change position unpredictably, are not included in the matrix. Figure 32 shows the plume-camera nonuniformity matrix with filter-specific blemishes removed. The spatial standard deviation over the central 112 by 91 pixels (zoom image rate region) is approximately 4%, and the standard deviation over the full pixel array is 12%.

The nonuniformity matrices have been normalized such that previously analyzed calibration star results (discussed in Section 5) are not altered by the application of the matrix. The ratio of measured  $DN$  to estimated  $PE$  resulting from application of this normalized matrix must be identical to that previously determined for the particular star. Since calibration constants were originally determined without using a nonuniformity matrix, the matrices are normalized such that  $P_w^{(s)} = P_{w/o}^{(s)}$ , where  $P_w^{(s)}$  is the number of photoevents resulting from a calibration star using the nonuniformity matrix, and  $P_{w/o}^{(s)}$  is the number of photoevents resulting from the same calibration star using no nonuniformity matrix. In all cases, the spatial mean value of the resulting nonuniformity matrix is very near to 1.0.

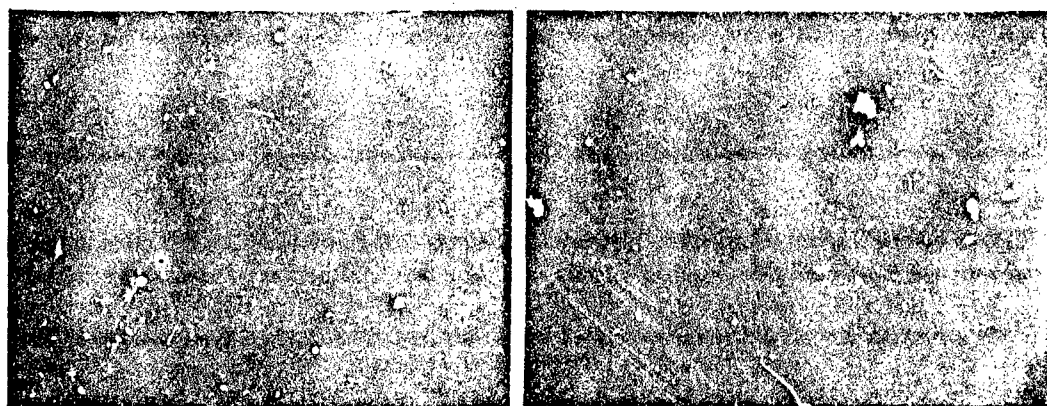
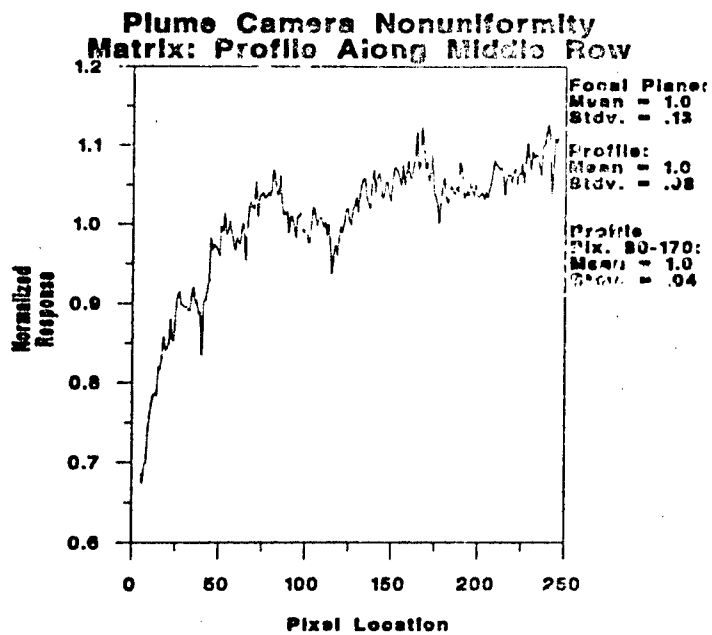
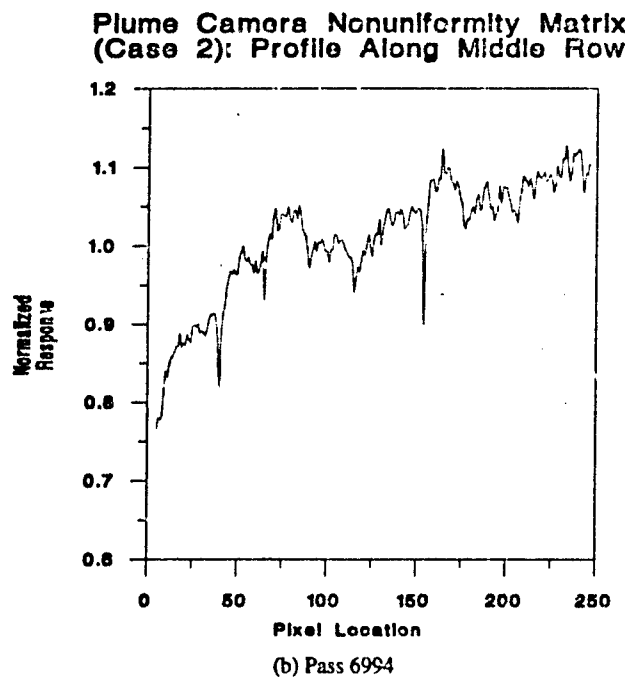


Fig. 28 - Plume-camera nonuniformities (passes 1606 and 6994)



(a) Pass 1606



(b) Pass 6994

Fig. 29 - Comparison of nonuniformity matrix central row profiles

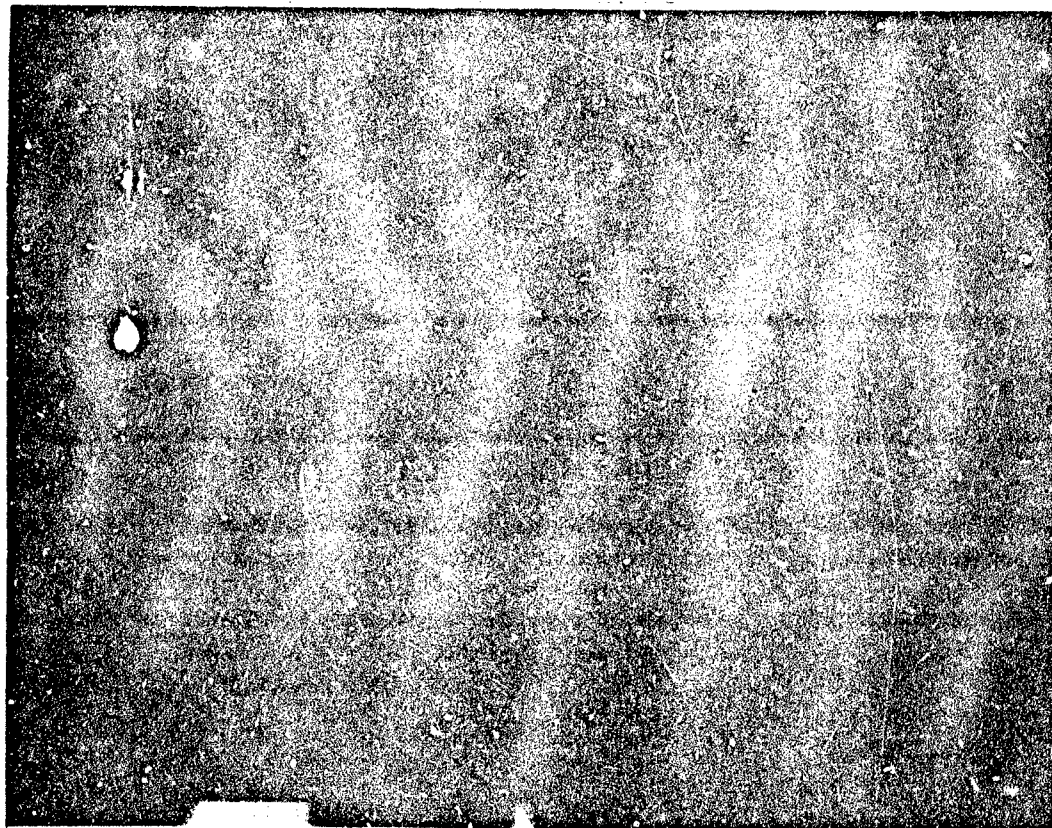


Fig. 30 - Difference between pass 6994 and 1606 nonuniformity matrices

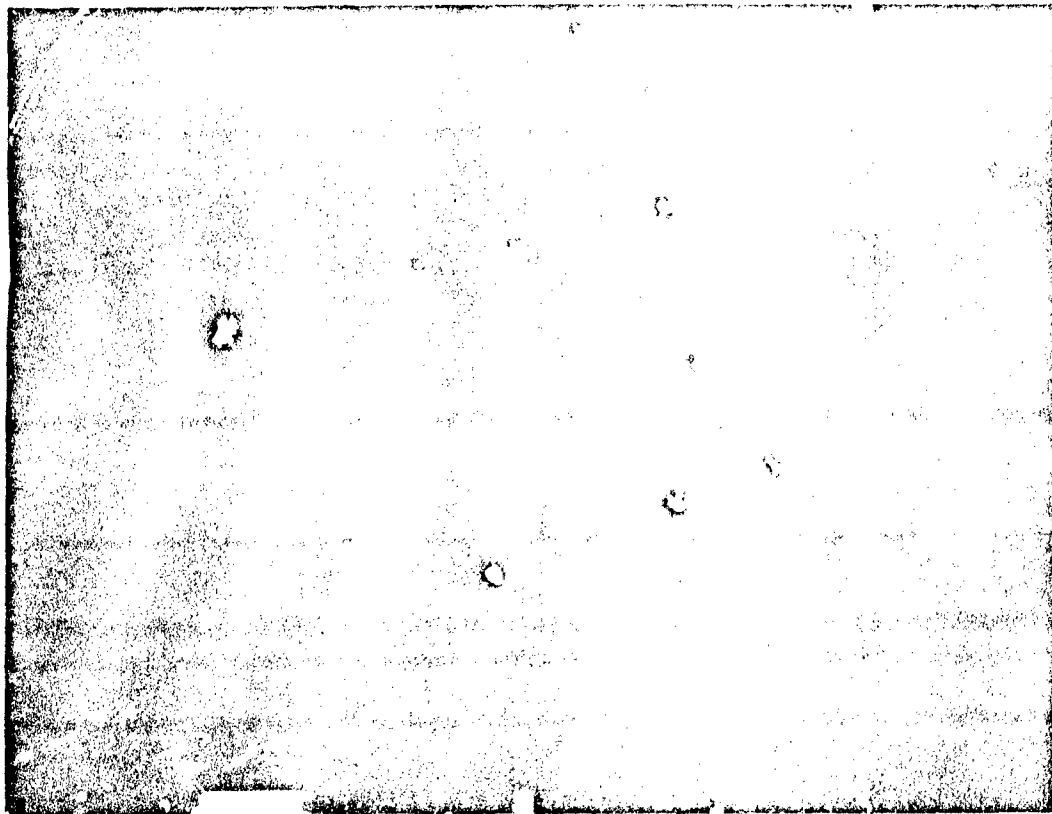


Fig. 31- Difference between pass 10175 and 1606 nonuniformity matrices

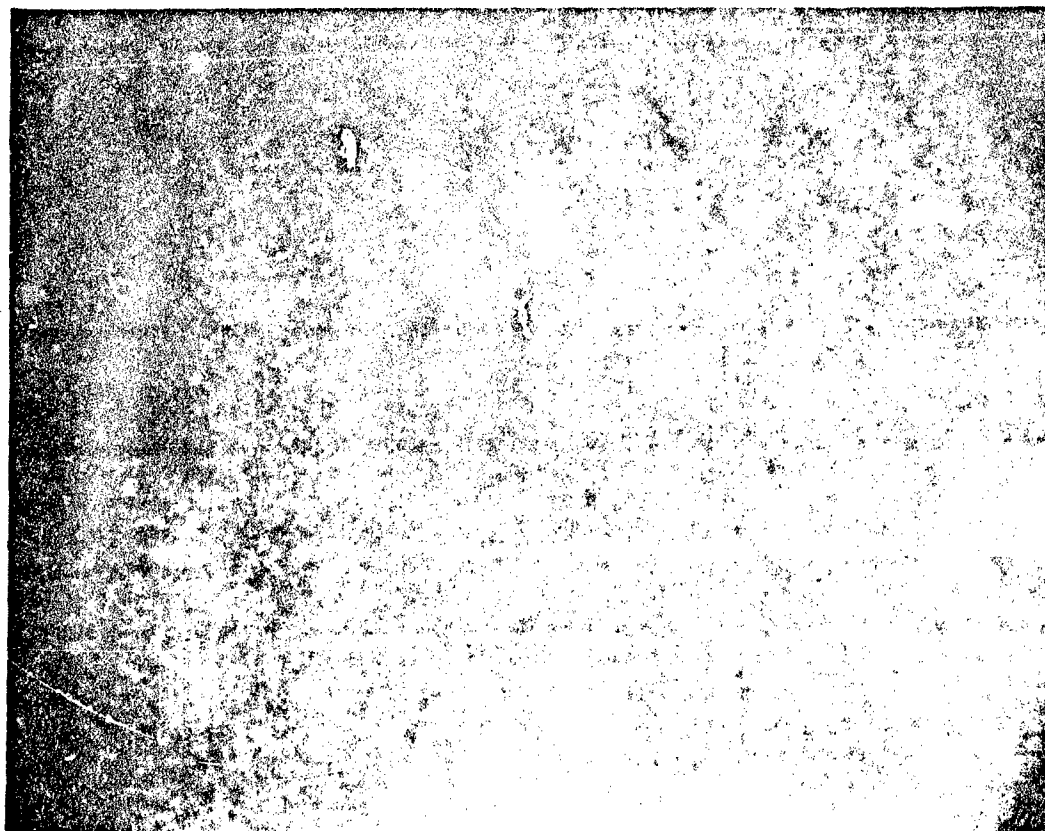


Fig. 32 - Plume-camera nonuniformity matrix used for calibration

Figure 33 shows the tracker-camera nonuniformity matrix. The tracker-camera exhibits only minor nonuniformities (Figs. 34 and 35). The spatial standard deviation is approximately 2% of the mean value, both over the entire focal plane and along a central row of pixels. In the tracker camera measurements, the effect of small clouds in the field of view were removed by selecting the minimum value, on a pixel-by-pixel basis, of a large sequence of frames. The scene is sufficiently bright that the photon shot noise is an insignificant fraction of the mean for each pixel. In the plume camera, no small clouds were observed, and each of the frames in a large sequence were indistinguishable from each other.

The tracker-camera nonuniformity matrix should also be normalized such that analyzed calibration star results (discussed in Section 5) are not altered by the application of the matrix. However, the tracker-camera normal-mode nonuniformity matrix used for data reduction was erroneously normalized such that the mean value over the entire field of view was 1.0. This normalization leads to a systematic 4% error in the tracker-camera normal image rate images delivered on UVPI data tapes. Therefore, all tracker-camera normal image rate calibrated values for each pixel delivered on UVPI data tapes should be reduced by 4%.

### *Bad Pixels*

A single small clump of bad pixels has been identified in the plume camera. Bad pixels are defined as those whose output is erratic and not correlated with the input signal. The group of 9 pixels centered around location (row 111, column 154) flashes on and off randomly from frame to frame. The source of the erratic behavior is likely in the MCP, because a group of pixels (rather than a single pixel) are affected. As an example, Fig. 36 shows two successive dark frames from pass 2076. The group of bad pixels is clearly visible slightly to right and above center in the second image. This same group of pixels behaves erratically in all types of UVPI plume-camera images.

No bad pixels are evident in the tracker camera.

### *Temporal Signal-Independent Noise*

Temporal signal-independent noise generated in the detectors and readout electronics includes electron shot noise, Johnson noise, 1/f noise, generation-recombination noise, and quantization noise. These noise components are measured as a temporal variation in the digitized dark field pixel values and are important for observations that do and do not include a dark field measurement. To determine the best possible dark frame pixel values for calibration purposes, it is necessary to average over a large number of dark frames. Data will be presented that show the temporal standard deviation for single dark frame pixels and groups of pixels.

### *Measurements*

All temporal signal-independent noise components are measured by calculating the temporal standard deviation, Eq. (3), for a large number of dark frames. The spatial mean of this temporal standard deviation is useful for discussion purposes:

$$\overline{\sigma}_D = \frac{1}{M} \sum_{k=1}^M \left\{ \sqrt{\left[ \frac{1}{N} \sum_{n=1}^N Q^2(\bar{x}_k, t_n) \right] - \left[ \frac{1}{N} \sum_{n=1}^N Q(\bar{x}_k, t_n) \right]^2} \right\} \quad (\text{DN}). \quad (6)$$



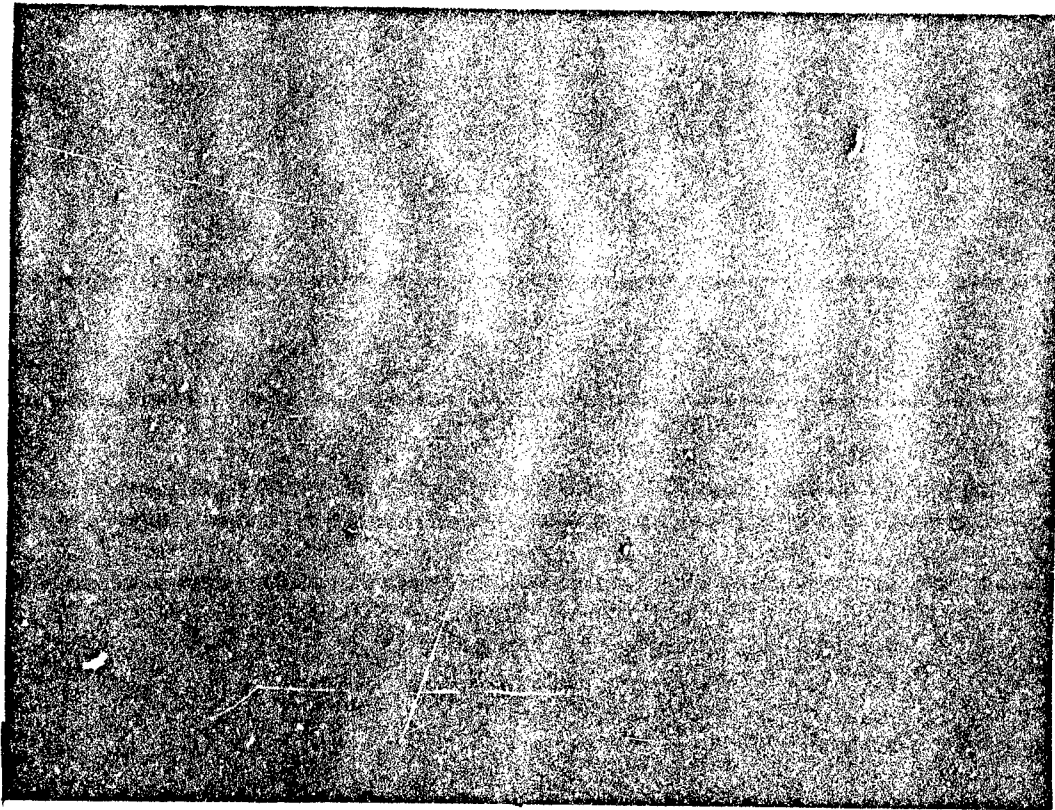


Fig. 33 - Tracker-camera nonuniformity matrix used for calibration

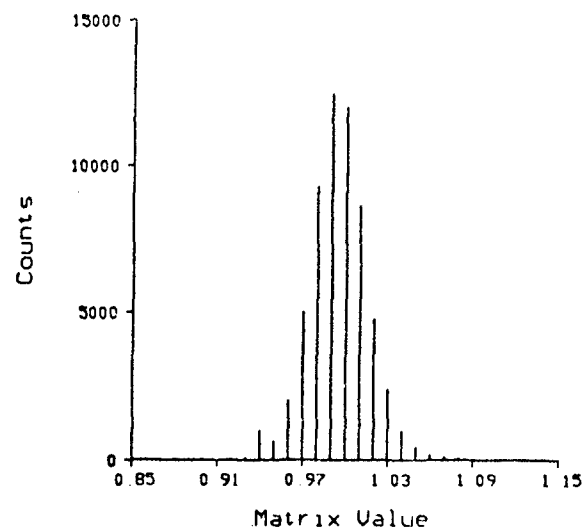


Fig. 34 - Tracker-camera inverse nonuniformity matrix histogram

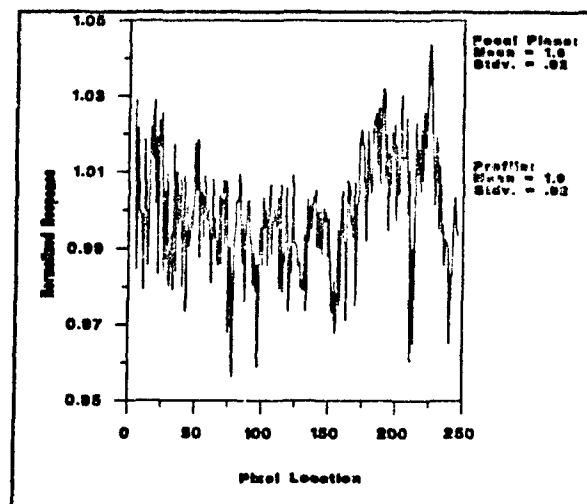


Fig. 35 - Tracker-camera nonuniformity profile along a central row

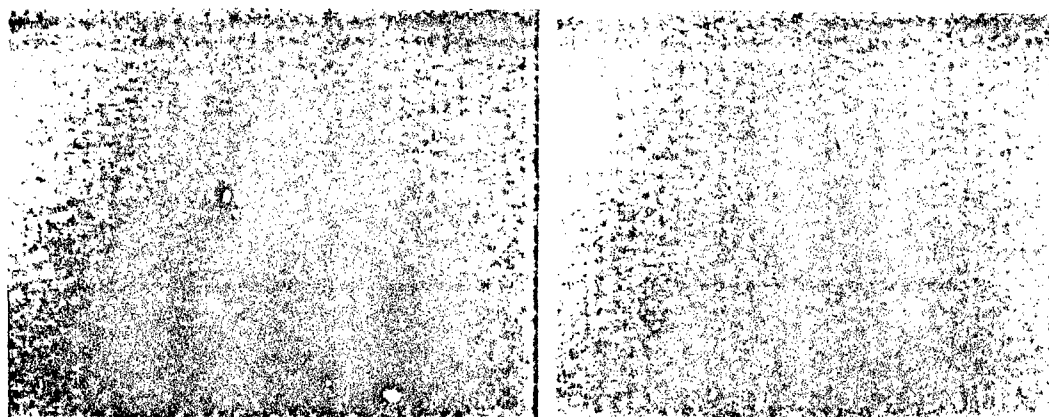


Fig 36 Bad pixels in the plume camera

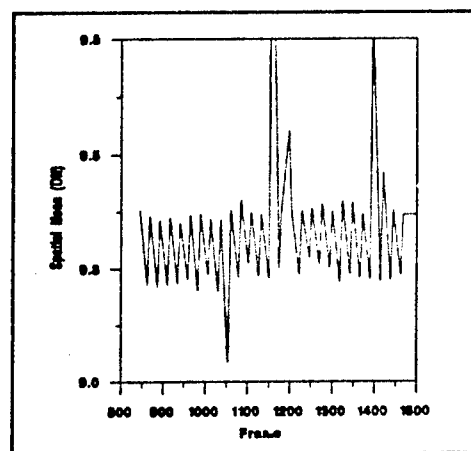
In this report, no attempt is made to model the individual noise components contributing to the total. Empirical results are shown in Table 10.

Table 10 - Dark Field Variations From Frame to Frame

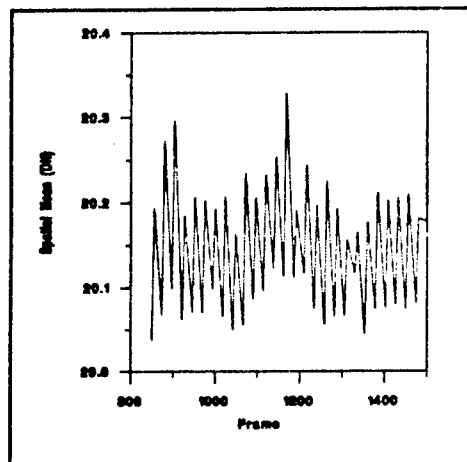
Orbit	Tracker Camera Frames	Tracker-Camera Spatial Mean of Temporal Standard Deviation (DN)	Plume-Camera Frames	Plume-Camera Spatial Mean of Temporal Standard Deviation (DN)
2076	32	1.57	32	1.13
5582	94	1.59	22	1.04
6786	105	1.61	104	1.16
6801	69	1.60	68	1.15
6816	115	1.61	115	1.15
7024	96	1.53	91	1.26
7200	104	1.91	103	1.16
7215	88	1.62	49	1.09
7324	103	1.60	104	1.17
7338	123	1.52	122	1.18
7487	99	1.77	90	1.19
7502	103	1.60	102	1.24
7828	138	1.54	137	1.18
8172	100	1.73	100	1.21
8739	96	---	97	1.08
8754	122	1.54	121	1.11
9037	97	1.57	94	1.15
9329	44	1.63	45	1.10
9344	44	1.62	45	1.11
9547	116	1.51	243	1.14
Mean:		1.61		1.15
Stdv:		0.10		0.05
Stdv/Mean:		5.9%		4.6%

Comparison shows that the mean of the spatial means of the temporal standard deviation shown in Table 10 (1.61 DN for the tracker camera and 1.15 DN for the plume camera) is approximately 8 to 12% of the mean of the spatial means of the temporal mean shown in Table 7 (19.49 DN for the tracker camera and 9.26 DN for the plume camera). Note that the frame-to-frame variation (1.61 DN for the tracker camera and 1.15 DN for the plume camera) is significantly larger than the pass-to-pass variation (0.49 DN for the tracker camera and 0.12 DN for the plume camera).

A small part of this variation is contributed by a slight oscillation of the spatial mean value from frame to frame (Fig. 37). The figure shows a series of dark field measurements at a single gain over a very short time period for the two cameras. The spatial mean values are clearly oscillating at the frame readout rate of  $5 \text{ s}^{-1}$ . The temporal standard deviation of the spatial mean is approximately 0.095 DN for the plume camera and 0.074 in the tracker camera.



(a) Plume camera



(b) Tracker camera

Fig. 37 - Oscillating values in plume- and tracker-camera dark frames

## Quantization Noise

The FPA readout undergoes an A/D conversion before the data are transmitted to the ground. A/D conversion involves the quantization of the charge stored to  $2^n$  different levels, where  $n$  is the number of bits available. UVPI used 8 bits, hence there are 256 different levels of quantization. Since quantization is a mapping of the continuous data sample space into a finite number of selected values, after the signal is quantized it cannot be recovered exactly as it was before quantization. Hence, the quantization process introduces some fluctuation about the true signal value. This fluctuation can be regarded as an additive noise. Assuming that for a given quantization interval the conditional density function of the input signal is uniform over that interval, the quantization error has a uniform distribution over a quantization interval; its mean square error is given [6] by  $1/12$ .

## 3.2. Temporal Signal-Dependent Noise

Signal-dependent noise is observed as a statistical variation in the readout pixel values that depends on the irradiance at the telescope aperture as a function of time. Also, fixed-pattern flat-field response variations may, in some instruments, be signal dependent. UVPI flat field response spatial variations (nonuniformity matrices) are expected to be signal independent.

It is assumed that there are two signal-dependent temporal-noise contributions in the UVPI output—photon shot noise caused by the random arrival rate of photons, and noise caused by temporal variations in the gain of the microchannel plate intensifier. Both of these noise contributions can be reduced, relative to the mean signal, by averaging over a large number of data frames.

### Photon Shot Noise

According to Wyatt [7], photon shot noise fluctuations "...set a fundamental limit to the accuracy by which the average photon rate can be measured. This limit arises from the quantum nature of the radiant source, and applies to the case of an ideal detector that is capable of counting every incident photon and that generates no noise."

The average power of incident radiation on the telescope aperture at a given wavelength can be written as

$$W(\lambda) = \bar{N}(\lambda) \cdot \frac{hc}{\lambda}, \quad (7)$$

where  $\bar{N}(\lambda)$  is the average number of photons of wavelength  $\lambda$  incident per second,  $c$  is the speed of light, and  $h$  is Planck's constant. Assume exactly one photoevent is produced for each  $[\eta(\lambda)]^{-1}$  incident photons, where  $\eta(\lambda)$  is the spectral net quantum efficiency discussed in Section 5.2. The average power can then be measured by counting the average number of photoevents accumulated during an integration period  $\tau$ :

$$P(\lambda) = \bar{N}(\lambda) \cdot \tau \cdot \eta(\lambda), \quad (8)$$

where  $P(\lambda)$  is the number of photoevents caused by photons of wavelength  $\lambda$ .

The randomly arriving photons obey Poisson statistics and, since the photoevents mimic the arriving photons, their generation also obeys Poisson statistics. The variance of a Poisson process equals its mean value [4]. Hence, the variance on the number of photoevents from photons of wavelength  $\lambda$ ,  $\sigma_p^2(\lambda)$ , equals

$$\sigma_p^2(\lambda) = P(\lambda) = W(\lambda) \cdot \tau \cdot \left( \frac{\lambda}{hc} \right) \cdot \eta(\lambda) \quad (9)$$

A necessary and sufficient condition for valid integration over wavelength for the above expressions for the mean and variance of the number of photoevents observed is that there is no statistical correlation between two spectrally adjacent measurements of photoevents,  $P(\lambda)$  and  $P(\lambda + \Delta\lambda)$ . Note that this condition does not imply that the two measurements are statistically independent random variables. For this report it is assumed that such a condition holds.

#### *Temporal MCP Response Variations*

It is assumed that all signal-dependent temporal variations are either photon shot noise or temporal MCP response variations. Since the photon shot noise is well characterized, MCP responsivity variations can be measured directly by using star and flat field data. Table 11 summarizes the mean photoevent count and its standard deviation for several star measurements. In general, the detector noise is approximately a factor of 1.6 above the estimated photon shot noise at all intensity levels. Figure 38 shows the photoevent count standard deviation plotted as a function of the mean photoevent count.

## 4. UVPI SPATIAL RESOLUTION

### 4.1. Tracker Camera

#### *Pixel Field of View*

Star patterns in the field of view (FOV) of the tracker camera were used to estimate the angular pixel resolutions in the horizontal and vertical directions. A typical star pattern contains at least 7 to 10 stars after frame averaging of three consecutive frames to reduce the noise level. After a particular star pattern in the tracker camera FOV has been matched against catalogued stars (in this case, the Smithsonian Astrophysical Observatory catalog), angular pixel resolution is determined. This determination is based on the stipulation that the angular separation between any two detected stars in the FOV must equal the angular separation between the two corresponding stars (of the catalog) whose positions are given in right ascensions and declinations.

For  $N$  stars detected in the FOV,  $N(N-1)/2$  independent equations can be formed in two unknowns,  $x$  and  $y$ . The technique of nonlinear least squares can then be applied to solve for  $x$  and  $y$ . The least-squares technique was applied to a set of three consecutive frames in an orbit. See Table 12 for tracker-camera pixel resolution. The overall results were obtained by averaging over 5 orbits with the maximum and minimum excluded from the average and standard deviation computation.

Table 11 - Mean Photoevent Count and Standard Deviation for Star Measurements

Star	Filter	Gain Step	Number of Frames	Mean PE (PE)	PE Std. Dev. (PE)	Photon Shot Noise (PE)
HD74753	2	13	41	9.272	2.614	3.045
$\alpha$ Col	2	11	93	40.324	8.554	6.350
$\alpha$ Vel	2	11	71	58.655	11.815	7.659
HD74753	3	11	49	72.353	10.715	8.506
HD74753	1	11	27	79.419	9.764	8.912
$\kappa$ Vel	2	11	45	79.684	13.776	8.927
$\kappa$ Vel	2	11	62	87.151	18.823	9.335
$\alpha$ Col	3	10	77	233.648	23.986	15.266
HD74753	4	10	29	269.911	27.014	16.429
$\kappa$ Eri	4	9	100	277.611	27.027	16.662
$\kappa$ Vel	3	9	64	476.100	29.641	21.820
$\kappa$ Vel	1	9	63	594.833	34.235	24.389
$\kappa$ Vel	3	9	83	631.114	38.506	25.122
$\kappa$ Vel	3	9	45	643.194	43.119	25.361
$\beta$ Cen	2	9	65	650.726	41.625	25.509
$\kappa$ Vel	1	8	10	732.474	41.864	27.064
$\kappa$ Vel	1	8	60	752.015	45.041	27.423
$\kappa$ Vel	1	9	30	781.184	95.421	27.950
$\chi$ Car	4	9	41	1153.962	53.938	33.970
$\alpha$ Col	4	8	104	1250.347	52.301	35.360
$\kappa$ Vel	4	7	47	2210.046	63.359	47.011
$\kappa$ Vel	4	6	9	2331.400	70.917	48.285
$\kappa$ Vel	4	7	80	3199.398	90.315	56.563
$\kappa$ Vel	4	7	100	3382.811	93.544	58.162
$\beta$ Cen	3	7	65	5327.780	116.340	72.992
$\beta$ Cen	1	6	65	5997.923	120.144	77.446
$\beta$ Cen	4	5	52	21458.690	293.153	146.488

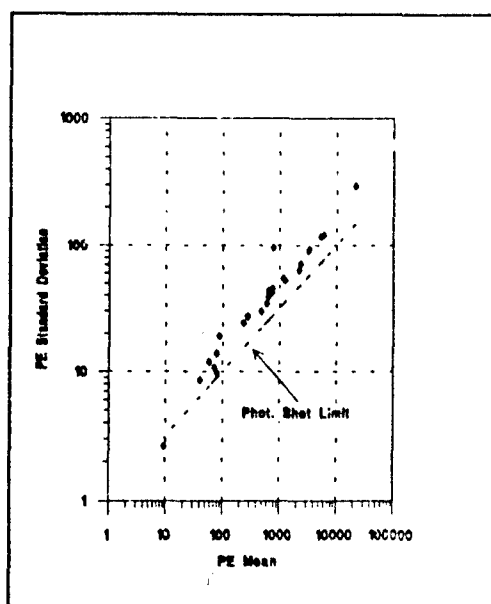


Fig. 38 - Photoevent count standard deviation as a function of mean photoevent count

Table 12 - Tracker-Camera Pixel Resolution

Orbit Number	Horizontal ( $\mu$ rad)	Vertical ( $\mu$ rad)
6533	182.90	146.17
6533	-	143.60
6548	179.16	143.73
6548	180.03	143.15
6563	179.93	
6563	180.64	143.97
6578	181.00	145.22
7321	180.08	141.74
Average	180.53	143.94
Std dev	1.19	1.43
Std dev (% of avg)	0.66	0.99

### Point Spread Function

The effective UVPI point spread function (PSF) is defined as the response of the instrument to a point source, e.g., a star or a ground-based beacon. The PSF is the result of many contributing factors, such as pixel size, spacecraft jitter, telescope optics, electronic blurring, and MCP blurring.

Estimates of the tracker camera PSF have been obtained at different times during the UVPI mission. For all of the PSF estimates presented in this section, the dark field background has been subtracted from the data, pixel values less than zero have been set to zero, and the data have been normalized such that the maximum value is one.



Table 13 summarizes PSF estimate results for one ground-based beacon observation and one star observation. The approximate full width of the PSF along its major axis is reported, in pixels, at 10% and 50% of the maximum amplitude. The star used in this observation is  $\kappa$ -vel. The values in this table were derived from 3-dimensional (3-D) and contour plots of the PSF over subimages of 16 by 16 pixels (Figs. 39 and 40). Figure 39 depicts the tracker camera PSF response to  $\kappa$ -vel during orbit 4621. On the top, a 3-D plot of the normalized PSF is shown; on the bottom, contour plots of the PSF are shown for three different amplitude levels of 0.9, 0.5, and 0.1 of the maximum value of 1. Figure 40 corresponds to the tracker-camera PSF while looking at a ground-based beacon during orbit 1173.

Table 13 - Typical Tracker Camera PSF Widths (With and Without Door Mirror)

UVPI Orbit No.	Point Source	Image Frame No.	UVPI Door Mirror	10% Full Width (pixel)	50% Full Width (pixel)	Comment
4621	$\kappa$ vel	8089	used	3	1.5	good quality
1173	Ground beacon	12772	not used	3	2.5	good quality

## 4.2. Plume Camera

### Pixel Field of View

Given the knowledge of plume-camera inter pixel distance (27.0  $\mu\text{m}$  along a column, 34.5  $\mu\text{m}$  across columns), and the inflight observation of two known close stars, the angular field of view for a pixel of the plume camera has been verified. The two stars are  $\mu^1$  scorpii and  $\mu^2$  scorpii, which have a small enough angular separation that they can both be imaged in the plume camera at the same time, as shown in Fig. 41. The  $\mu^1$  scorpii right ascension and declination are, respectively, 252.8134 and -38.0326. The  $\mu^2$  scorpii right ascension and declination are, respectively, 252.9796 and -38.0027. The angular separation  $\theta_r$  is calculated to be  $1.681 \times 10^{-3}$  radians.

The distance between star images on the focal plane was determined by calculating the centroid location for each of the two stars and determining the offset in pixel rows and columns. The centroid location for a single star image is calculated by selecting an  $n$  by  $n$  pixel region around the image and using

$$(\Delta r)_{\text{cm}} = \frac{1}{\sum_j f(i, j)} \cdot \sum_{i=1}^n \left[ i \cdot \sum_{j=1}^n f(i, j) \right] \quad (10)$$

and

$$(\Delta c)_{\text{cm}} = \frac{1}{\sum_i f(i, j)} \cdot \sum_{j=1}^n \left[ j \cdot \sum_{i=1}^n f(i, j) \right] \quad (11)$$

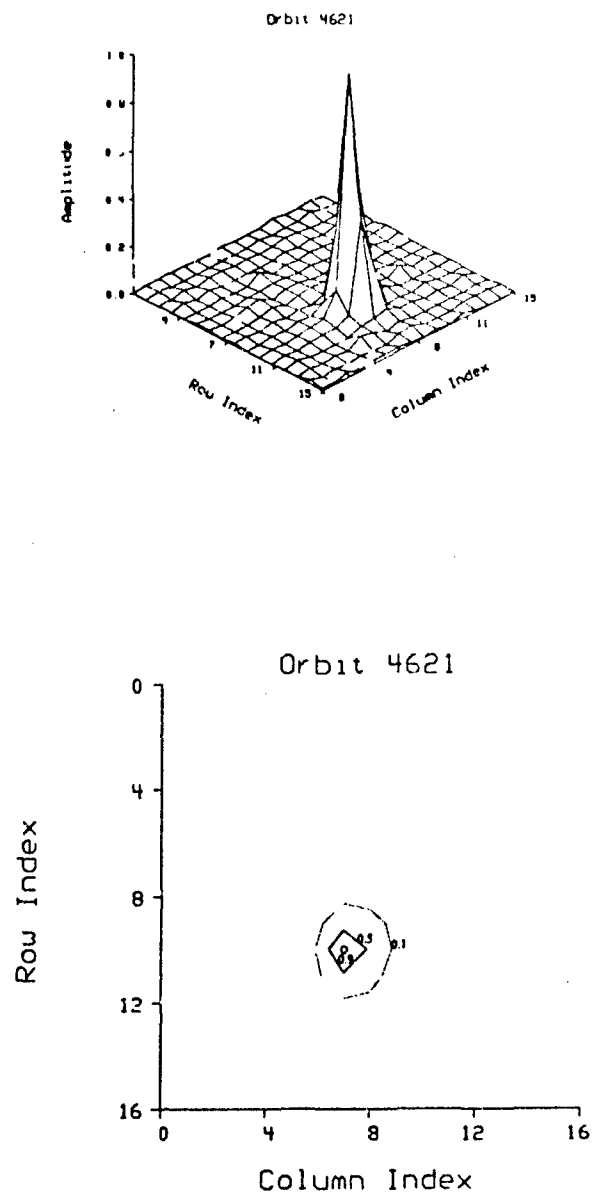


Fig. 39 - Tracker camera PSF derived from star observation during orbit 4621

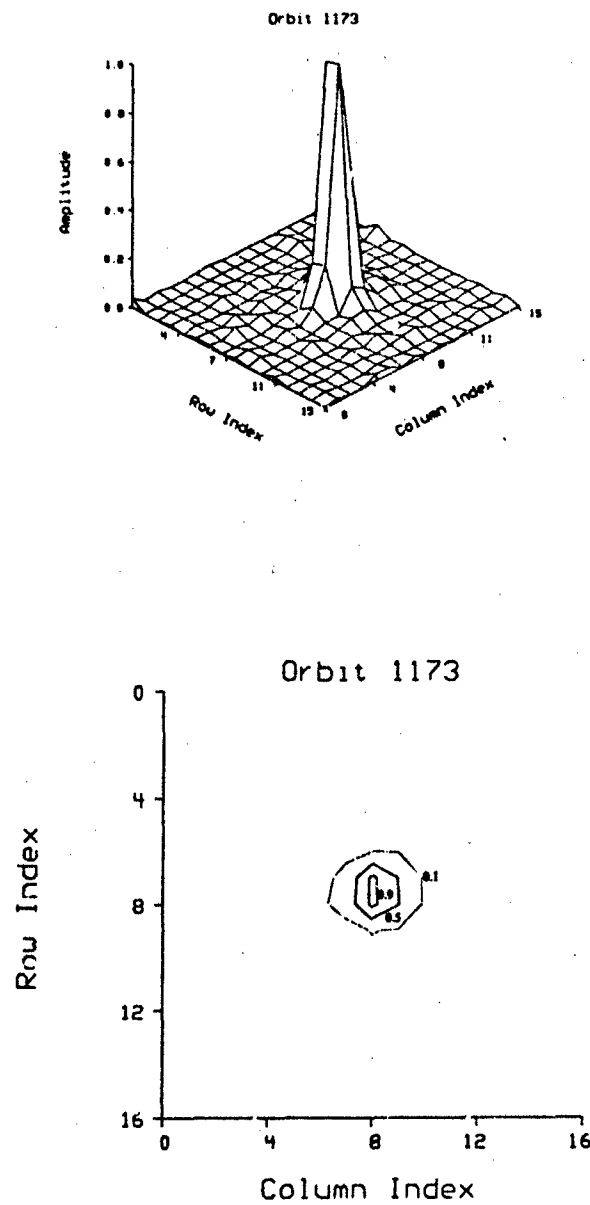


Fig. 40 - Tracker-camera PSF derived from beacon observation during orbit 1173

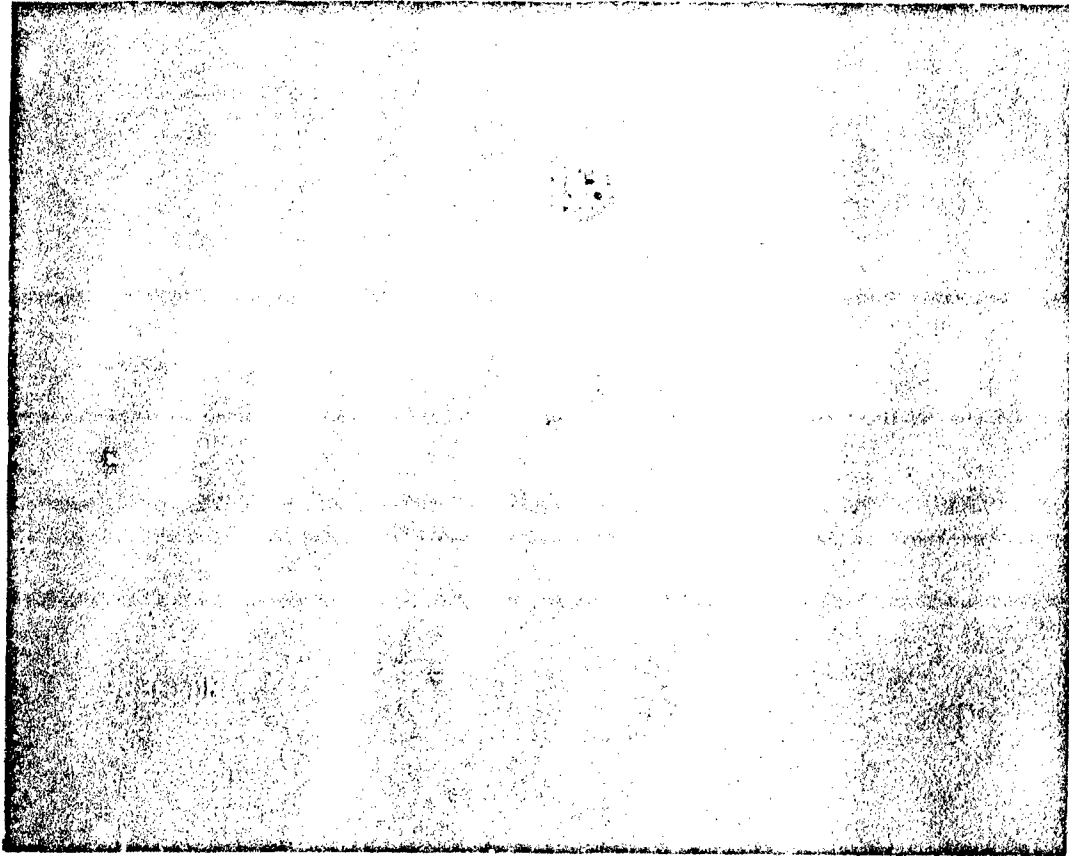


Fig. 41 - Two stars simultaneously imaged in the plume camera

Here  $(\Delta r)_{n \times n}$  and  $(\Delta c)_{n \times n}$  specify the offset in rows and columns between the centroid and the upper left-hand corner of the  $n$  by  $n$  region,  $i$  and  $j$  are the pixel indices within the  $n$  by  $n$  region, and  $f(i,j)$  is the image intensity (with units DN) at pixel position (row= $i$ , column= $j$ ).  $(\Delta r)_{n \times n}$  and  $(\Delta c)_{n \times n}$  were used to determine the absolute row and column position of the image intensity centroid on the focal plane. Measurements of the centroid locations  $(R_1, C_1)$  and  $(R_2, C_2)$  for  $\mu^1$  scorpii and  $\mu^2$  scorpii were made, and the offsets,  $\Delta x = |C_2 - C_1|$  and  $\Delta y = |R_2 - R_1|$  between the two centroids were calculated. The distance  $r$  between the two centroids on the focal plane is then given by

$$r = \sqrt{(\Delta x \cdot 34.5)^2 + (\Delta y \cdot 27.0)^2} \quad (\mu\text{m}), \quad (12)$$

and the angular field of view per pixel in the  $x$  and  $y$  directions is given by

$$\Omega_x = \frac{\Theta_r}{r} \left( \frac{\text{rad}}{\mu\text{m}} \right) \times 34.5 \left( \frac{\mu\text{m}}{\text{pix}} \right) \quad (13)$$

$$\Omega_y = \frac{\Theta_r}{r} \left( \frac{\text{rad}}{\mu\text{m}} \right) \times 27.0 \left( \frac{\mu\text{m}}{\text{pix}} \right). \quad (14)$$

Table 14 shows results of several measurements.  $\Omega_x$  is found to be  $12.78 \mu\text{rad}$ , and  $\Omega_y$  is  $10.00 \mu\text{rad}$ , giving a total pixel field of view of  $\Omega_x \Omega_y = 1.278 \times 10^{-10}$  steradians.

#### Point Spread Function

The effective UVPI point spread function (PSF) is defined as the response of the instrument to a point source, e.g., a star or a ground-based beacon. The PSF is the result of many contributing factors, such as pixel size, spacecraft jitter, telescope optics, electronic blurring, and MCP blurring. Based on review of UVPI data from many observations, one may conclude that the plume camera's PSF depends on the observation modality, i.e., downward-looking vs sideward-looking. Sideward-looking observations use the door-mounted mirror, but downward-looking observations do not. Existing data for point sources indicate that the PSF is less circularly symmetric when using the door-mounted mirror.

Estimates of the plume-camera PSF have been obtained at different times during the UVPI mission. For all of the PSF estimates presented in this subsection, the dark field background has been subtracted from the data, pixel values less than zero have been set to zero, and the data have been normalized such that the maximum value is one.

Table 15 summarizes PSF estimate results for one ground-based beacon and four star observations, where the approximate full width of the PSF along its major axis is reported, in pixels, at 10% and 50% of the maximum amplitude. The star used in these observations is  $\kappa$ -vel. The values in this table were derived from 3-D and contour plots of the PSF over subimages of 32 by 32 pixels, see Figs. 42-46. Figure 42 depicts the plume-camera PSF response to  $\kappa$ -vel during orbit 1584. On the top a 3-D plot of the normalized PSF is shown and, on the bottom, contour plots of the PSF are shown for three different amplitude levels of 0.9, 0.5, and 0.1 of the maximum value of 1. The irregular shape of the plume camera PSF is believed to have its origin in jitter introduced by the UVPI door mirror. Figures 43-45 show, respectively, the plume camera PSF while looking at  $\kappa$ -vel during orbits 4621, 4636, and 597.

Table 14 - Plume-Camera Pixel Field of View Measurements

$C_1$	$R_1$	$C_2$	$R_2$	$\Delta x$ (pixel)	$\Delta y$ (pixel)	$r$ ( $\mu m$ )	$\Omega_x$ ( $\mu rad$ )	$\Omega_y$ ( $\mu rad$ )
109.16	182.61	144.85	20.81	35.69	161.80	4538.90	12.78	10.00
107.49	185.59	143.09	23.80	35.61	161.78	4537.57	12.78	10.00
108.36	183.84	144.04	22.19	35.68	161.65	4534.88	12.79	10.01
109.52	181.16	144.91	19.29	35.40	161.87	4537.78	12.78	10.00
108.38	184.11	143.67	22.41	35.29	161.70	4532.46	12.80	10.02
108.32	184.87	143.50	23.02	35.18	161.85	4535.49	12.79	10.01
107.93	187.02	143.08	25.10	35.15	161.93	4537.11	12.78	10.01
107.52	185.83	142.77	23.63	35.25	162.21	4545.36	12.76	9.99
108.25	184.75	143.41	22.74	35.16	162.01	4539.21	12.78	10.00
108.15	183.95	143.41	21.77	35.26	162.17	4544.43	12.76	9.99
108.37	182.25	143.50	20.18	35.13	162.07	4540.52	12.77	10.00
108.27	184.70	143.30	22.14	35.03	162.55	4552.24	12.74	9.97
109.22	182.16	144.11	20.05	34.88	162.11	4539.47	12.78	10.00
108.69	182.50	143.40	20.56	34.71	161.94	4533.49	12.79	10.01
108.39	187.48	143.32	25.20	34.93	162.29	4544.46	12.76	9.99
109.15	182.27	144.01	20.22	34.86	162.06	4537.77	12.78	10.00
108.64	182.50	143.49	20.43	34.85	162.07	4538.06	12.78	10.00
108.82	179.23	143.62	16.63	34.80	162.61	4551.51	12.74	9.97
Mean value:				35.16	162.04	4540.04	12.78	10.00
% error:				0.85	0.16	0.12	0.12	0.12

Table 15 - Typical Plume Camera PSF Widths (With and Without Door Mirror)

UVPI Orbit No.	Point Source	Image Frame No.	UVPI Door Mirror	10% Full Width (pixel)	50% Full Width (pixel)	Comment
1584	$\kappa$ -vel	3803p	used	17	14	irregular shape
4621	$\kappa$ -vel	8089p	used	18	6	irregular shape
4636	$\kappa$ -vel	7879p	used	15	6	irregular shape
0597	$\kappa$ -vel	6916p	used	10	6	1 main lobe
1173	Ground beacon	12778	not used	17	8	1 main lobe

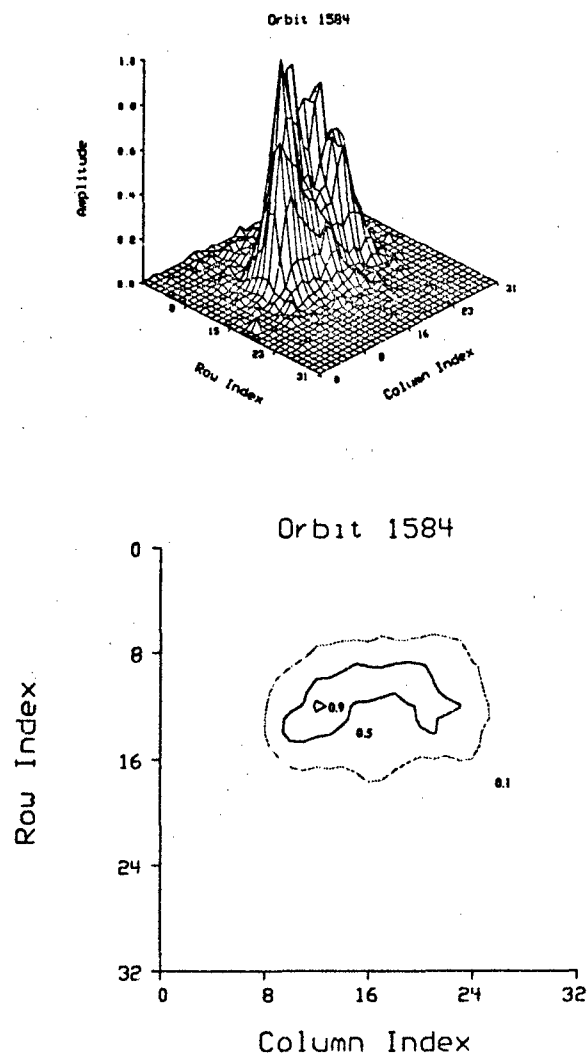


Fig. 42 - Plume-camera PSF derived from star observations during orbit 1584

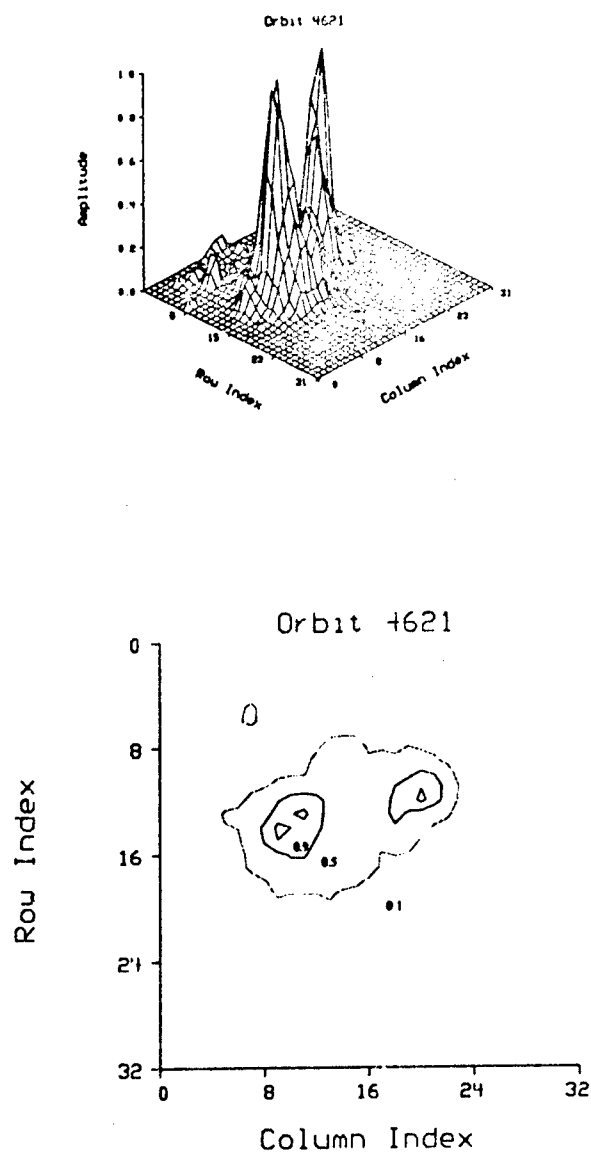


Fig. 43 - Plume-camera PSF derived from star observation during orbit 4621



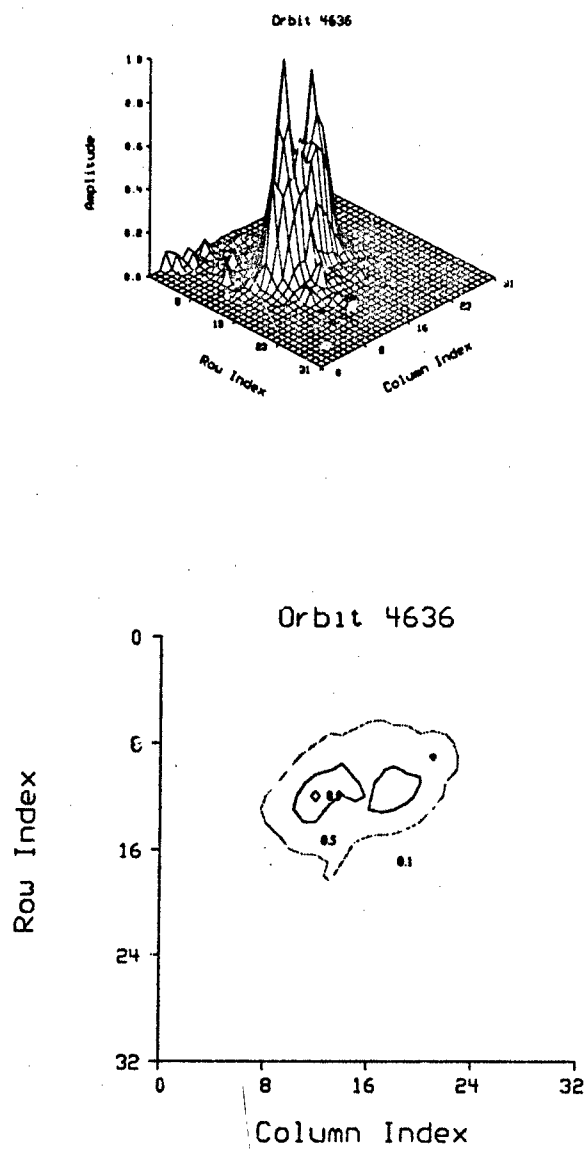


Fig. 44 - Plume-camera PSF derived from star observations during orbit 4636

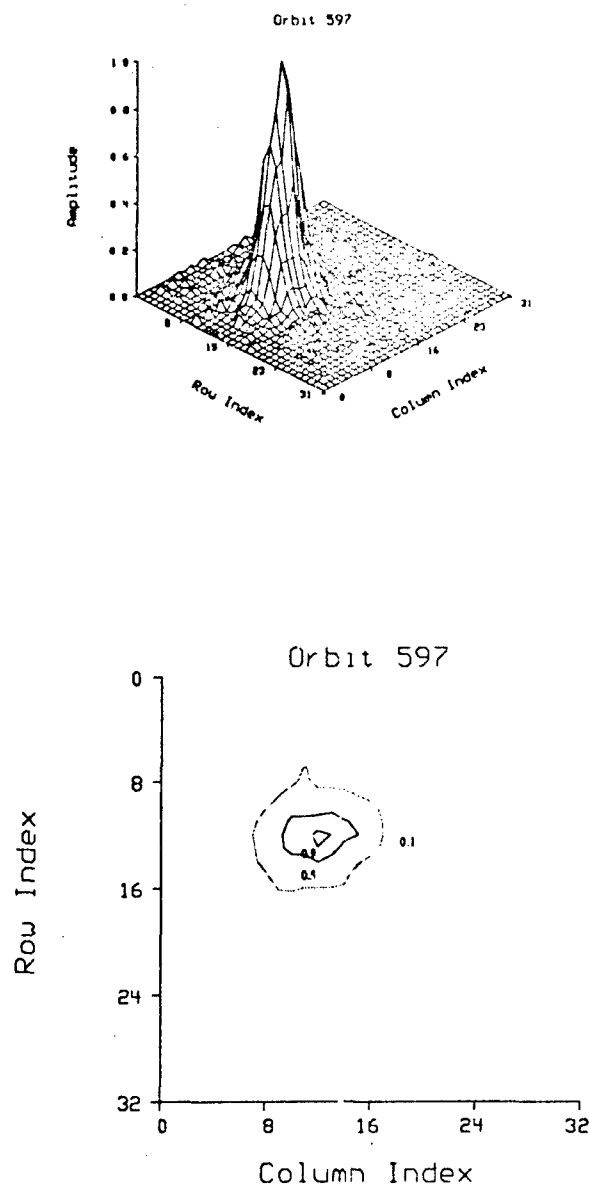


Fig. 45 - Flume-camera PSF derived from star observation during orbit 597

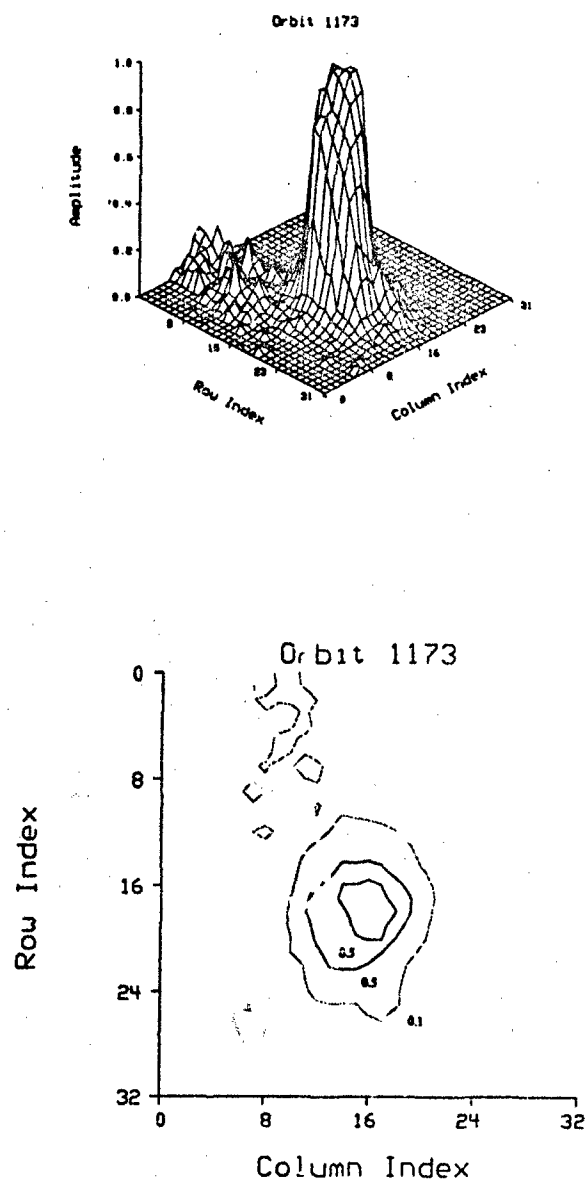


Fig. 46 - Plume-camera PSF derived from beacon observation during orbit 1173

Figure 46 depicts the UVPI plume-camera PSF response to a ground-based beacon during orbit 1173. The nominal plume-camera PSF shape used in the rocket plume reports [8-11] corresponds to a block of 16 by 16 pixels around the brightest pixel in the ground-based beacon response.

## 5. UVPI SENSOR RESPONSE

The goal of the UVPI sensor calibration effort is to ensure that the instrument response is well understood under all measurement conditions and that the accuracy and precision of calibration constants, at any time in the mission, are well known. Derived response functions are used to convert 8-bit pixel readout values to useful radiometric units (such as watts  $\text{sr}^{-1} \mu\text{m}^{-1}$  or rayleighs/angstrom) with error bars, and to specify the spatial characteristics of the scene or target of interest in length or area units.

Determination of target or scene radiometric characteristics requires a thorough understanding of sensor spectral responsivity. This depends on MCP gain step, tracker-camera integration time, and pass-specific parameters. To convert from photoevents to radiometric units, an assumption must be made concerning the spectral energy distribution of the target or scene.

Determination of target or scene spatial characteristics from UVPI images requires a full characterization of the system point spread function, as well as knowledge of observation range. System point spread function was discussed in Section 4.

To determine the wavelength-dependent total responsivity (8-bit digital numbers per photon) on-orbit, calibration measurements were regularly made throughout the UVPI mission by using well characterized stars. These measurements, in conjunction with measurements performed at Loral Electro-Optic Systems and ITT prior to launch, were used to derive the revised intensity calibration curves presented in this section. These revised curves are compared with laboratory measurements in the next section. It should be noted that the results presented here (UVPI calibration version 3) are revisions of those presented in the UVPI rocket reports (UVPI calibration version 2) [8-11]. Simple conversion factors to convert between the two versions are presented in the next section and in the final section.

Based on star and laboratory measurements, the total responsivity of the UVPI is described as the product of two terms, one wavelength-dependent and one MCP gain dependent. The wavelength-dependent term accounts for transmission in the optics and spectral filters, for inefficiencies in the photocathode response, and for collection inefficiency in the MCP. These losses are combined to obtain net quantum efficiency functions  $\eta_i(\lambda)$ , which take into account the total wavelength-dependent responsivity (photoevents per photon) of the sensor with spectral filter  $i$  in place, independent of MCP gain, phosphor efficiency, and CCD quantum efficiency. The effect of MCP gain, phosphor efficiency, and CCD quantum efficiency on responsivity is isolated in the gain conversion factors  $G_g$ , one for each MCP gain step,  $g = 0, \dots, 15$ .

It is assumed that the net quantum efficiency functions  $\eta_i(\lambda)$  do not depend on MCP gain, scene irradiance, or pass-specific parameters and, therefore, are constant under all measurement conditions. Two sets of net quantum efficiency functions are necessary—one set for observations using the UVPI door mirror  $\eta_{i,w}(\lambda)$ , and one set for observations without the door mirror,  $\eta_{i,w/o}(\lambda)$ .

Using these definitions, the total responsivity of the UVPI with spectral filter  $i$  in place and at MCP gain step  $g$  is

$$R_{i,g}(\lambda) = \eta_i(\lambda) \cdot G_g \quad (\text{DN / photon}). \quad (15)$$

To derive the total responsivity on-orbit, laboratory measurements of the shapes of the net quantum efficiency and gain conversion functions are used as a starting point. Since the responsivity of each individual detector element, or pixel, can change during the course of the UVPI mission, it is essential that ongoing in-flight measurements of well characterized stars are made frequently in order to adjust the laboratory calibration. This section discusses the procedure used to revise the laboratory calibration functions by using a known star's spectrum and UVPI measurements of that star. An empirical model of the UVPI radiometric response is used to predict the response to a known star. By comparing the prediction to the measured data, a set of calibration constants is obtained. The method requires that:

- UVPI must track the selected star, and
- reliable UV spectra for the observed star must be known.

### 5.1. Laboratory and On-Orbit Measurements of the Gain Conversion Factor

Prior to launch, ITT measured the relationship between MCP voltage and MCP photoelectron gain. Combined with knowledge of the MCP voltage associated with each UVPI gain setting, relative to gain setting zero, these measurements define the shape of the gain conversion factor. The on-orbit gain conversion factor was derived by fixing the amplitude of the ITT functional shape based on direct on-orbit measurements of the number of 8-bit digital numbers (DN) per photoevent (PE) at high gain settings.

In this section it is assumed that the net quantum efficiency curves stay constant under all measurement conditions and, therefore, that the number of photoevents per photon incident on the MCP are completely determined at each wavelength for a given spectral filter and door mirror configuration. The MCP gain dependence of the total responsivity (digital numbers per photoevent) is taken into account by using the gain conversion factors  $G_g$  for each MCP gain step  $g$ , which are independent of wavelength. These factors specify the number of digital numbers (DN) output from the A/D converter per photoevent (PE) incident on the MCP. Because of the consistency and repeatability of on-orbit calibration star measurements, discussed later, it is apparent that the  $G_g$  values do not have a strong dependence on pass-specific parameters, and small pass-to-pass variations are simply included in calibration error estimates.

#### *Gain Conversion Factor Estimation Procedure*

This section discusses the method used to estimate gain conversion factors at high gains by using sparse field images. A sparse field image is defined as an image in which a small number of photoevents are recorded in the focal plane of the camera and no significant spatial or temporal overlapping between the individual photoevents takes place. Figure 47 depicts a 3-D plot of a 33 by 33 pixel plume-camera subimage in which three photoevents are clearly visible as amplitude spikes. The image was obtained with the UVPI door closed and an MCP gain of 15. Notice that photoevents occupy multipixel regions and can have different peak amplitudes. The observed spatial extent of a single photoevent is caused by the combination of the MCP, the phosphor, and the fiber optic bundle interface. This blurring is one of the many factors affecting the overall camera point spread function. The observed background variations are primarily induced by fixed-pattern dark field variations and thermal noise. The final evaluation of sparse field image acceptability is done by visual inspection. Typically, sparse field images result when low irradiance levels are at the MCP aperture and high MCP gains are used. For a given MCP gain level, the primary goal of the sparse field analysis is to estimate the average integrated DN response of a single photoevent  $G_g$  with units of DN/PE; the secondary goal is to estimate its average spatial extent.

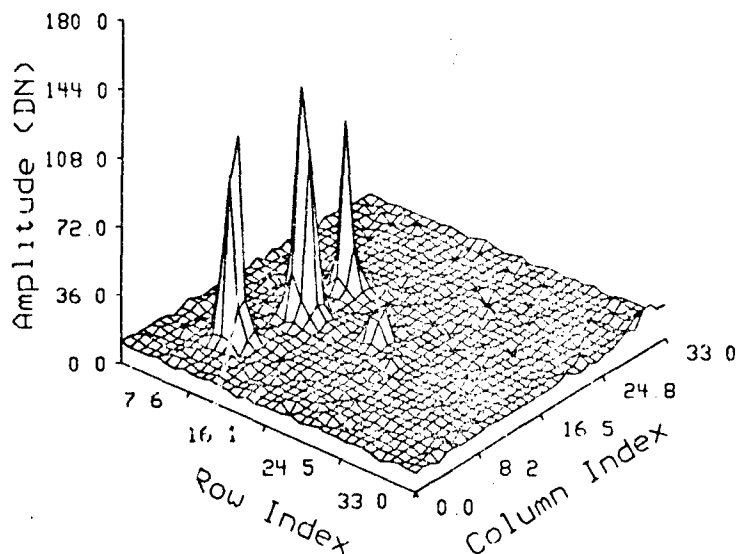


Fig. 47 - Single photoevents in a plume camera subimage at MCP gain of 15

Given a sequence of sparse field images gathered from the same camera-filter-gain combination and over a small time window,  $\{t_n | n = 1, \dots, N\}$ , a scheme was developed to measure  $G_g$ . The problem was posed as a detection and estimation problem where the signal is the photoevent and the noise is the dark field spatial and temporal fluctuations. A photoevent is discriminated from the background noise based on its amplitude and shape.

#### Amplitude Discrimination

For amplitude discrimination, the readout value of a pixel was considered to be the result of at least one photoevent if it exceeded a threshold value derived from the pixel background noise statistics and an accepted probability of false alarm (PFA). The PFA is the probability that the pixel DN value will exceed the derived threshold with no photoevent present, resulting in a false detection. In particular, given the  $k$ th pixel, an  $N$  dimensional vector of raw DN values in time can be constructed, i.e.,  $\{Q_{k,n} | n=1, \dots, N\}$  from which the threshold value was computed. To suppress biases or large deviations introduced by photoevents, a median filtered version of the raw data vector was constructed,

$$B_{k,n} = \text{median}(Q_{k,n-2}, \dots, Q_{k,n+2}). \quad (16)$$

From this estimates of the  $k$ th pixel background noise sample mean  $\mu_{B_k}$  and the background noise sample variance  $\sigma_{B_k}^2$  were derived as

$$\begin{aligned}\mu_{B_k} &= \frac{1}{N} \sum_n B_{k,n}, \\ \sigma_{B_k}^2 &= \frac{1}{N} \sum_n B_{k,n}^2 - \mu_{B_k}^2.\end{aligned}\tag{17}$$

Given an acceptable PFA and the assumption that the dark field fluctuations of a pixel have a Gaussian distribution, a threshold value was computed for each pixel by using the equation,

$$T_k = \mu_{B_k} + \text{erfc.}(PFA) \cdot \sigma_{B_k}\tag{18}$$

where  $\text{erfc.}(x)$  is the complementary error function [12]. In this analysis, a PFA of  $1 \times 10^{-8}$  was adopted for PE discrimination. This corresponds to a value of  $\text{erfc.}(PFA) = 5.61$ . For example, by using plume-camera sparse field data gathered at gain step 13 during orbit 2089, typical values for  $\mu_{B_k}$  are approximately  $9.41 \pm 0.957$  DN; typical values for  $\sigma_{B_k}$  are approximately  $0.53 \pm 0.24$  DN; and a typical decision threshold value  $T_k$  is 12.38. Pixels whose value exceeded the threshold value were then subjected to spatial discrimination.

### Spatial Discrimination

Spatial discrimination was applied to each pixel corresponding to a possible photoevent by the following steps:

- Rank by amplitude all the pixels identified during the amplitude discrimination process to be possible photoevents on a given image. Select the brightest pixel  $k_0$  and construct an  $S$  by  $S$  pixel window around that pixel. Such a region is denoted as  $\Gamma_{k_0}$ . Typical values of  $S$  used are  $S = 3, 5, 7$ .
- Accept this region as a real photoevent if at least 5 pixels within the  $S$  by  $S$  window exceed their threshold and if it does not overlap any previously identified region.
- Continue with the next brightest pixel left until no more pixels are left that exceed the threshold on the image. The process is started on the next image.

A program was developed using the MSHELL Image/Signal Processing language to autonomously apply the amplitude and spatial discrimination schemes to a group of images. Figure 48 depicts the output of the program in the middle of its processing. The upper left image is the raw data as gathered by the UVPI camera. The lower left image is the estimated dark field image that resulted from the dark background estimation process. The lower right image depicts the location of possible photoevents. The upper right image shows the already identified photoevents as black spots. The overlay photoevent regions shown in light blue are not used in sparse field analysis process.

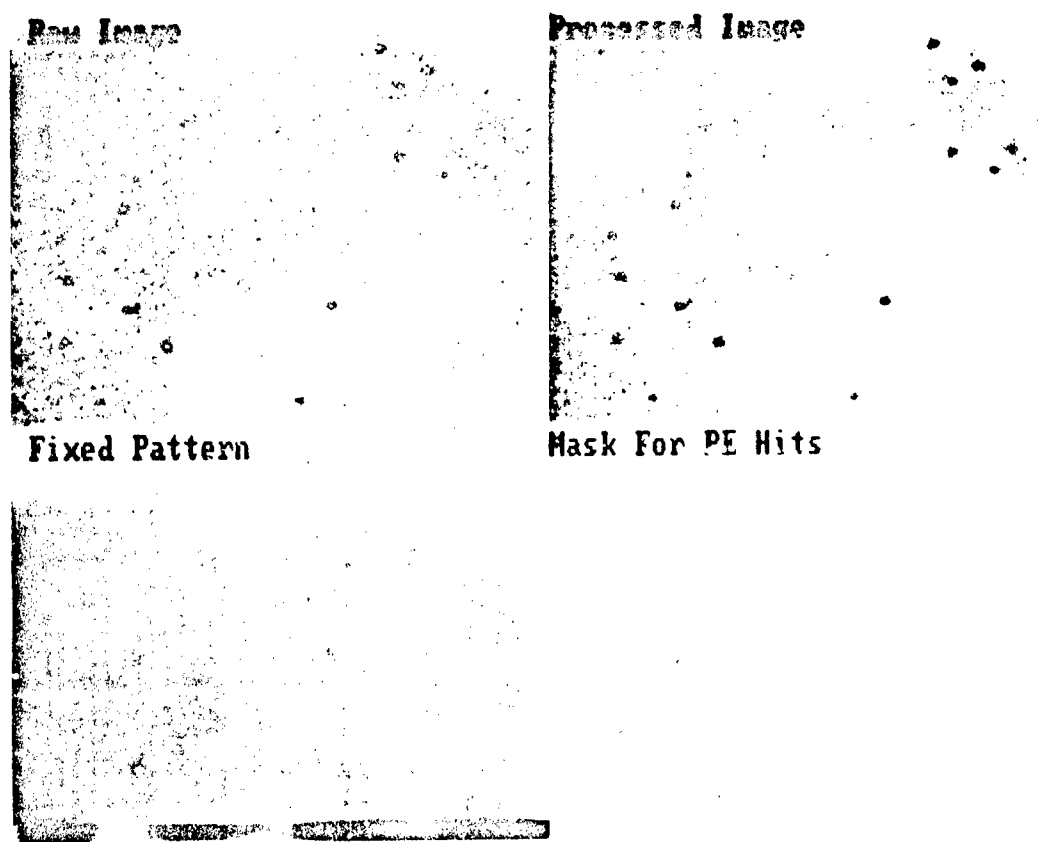


Fig. 48 - Mid-processing output of sparse field analysis program

For identified photoevents, indexed by  $i = 1, \dots, I_n$ , the net spatial mean  $\mu_{s,n,i}$  and variance  $\sigma_{s,n,i}^2$  was computed as follows:

$$\begin{aligned}\mu_{s,n,i} &= \frac{1}{S^2} \sum_{k \in \Gamma_{k,n,i}} F_{k,n,i} \\ \sigma_{s,n,i}^2 &= \frac{1}{S^2} \sum_{k \in \Gamma_{k,n,i}} F_{k,n,i}^2 - \mu_{s,n,i}^2\end{aligned}\quad (19)$$

where  $F_{k,n,i}$  is the DN value at pixel  $k$  and time  $t_n$  that results after subtracting its corresponding dark field estimate, i.e.,

$$F_{k,n,i} = (Q_{k,n} - \mu_{B_i}), \quad k \in \Gamma_{k,n,i} \quad (20)$$



Hence, for the given MCP gain level  $g$  and assuming a photoevent support region of  $S$  by  $S$  pixels, the estimated total DN response per photoevent  $G_{g,s}$  is defined by

$$G_{g,s} = S^2 \cdot \frac{1}{N} \sum_{n=1}^N \frac{1}{I_n} \sum_{l=1}^{I_n} \mu_{s,n,l} \quad (21)$$

Good physical intuition can be gained by looking at the density functions of the DN/pixel values for the noise alone and the signal plus noise, i.e., the dark field background noise and the photoevent on top of the dark field background. Figure 49 depicts the density functions that resulted for a single pixel on the analysis of preflight data, 385\_4B1010D7FL2Z\_W.LIS, using a window size of 5 by 5, and MCP

gain of 13. On the left is the noise density function estimate for a single pixel, with mean  $\mu_{B_k} = 10.05$ ,

standard deviation  $\sigma_{B_k} = 0.63$ , and a decision threshold at  $T_k = 13.57$ . On the right is the signal plus noise density function. This plot shows that the noise density function looks fairly symmetric around its peak value and the signal and noise are fairly separable at this gain and window size.

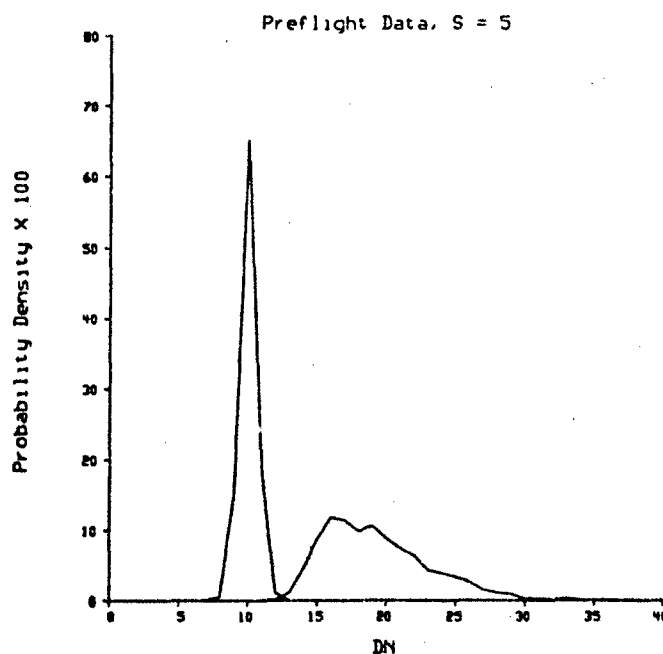


Fig. 49 - Density functions of noise and signal plus noise

## Results

Recall that for a given MCP gain level, the primary goal of the sparse field analysis is to estimate the average integrated DN response of a single photoevent  $G_g$  with units of DN/PE; the secondary goal is to estimate its average spatial extent. Sparse field analysis was performed on inflight and pre-flight observations for the piume and tracker camera.

The photocathode material used in the plume camera, cesium telluride, produces fewer dark current electrons than the bialkali used in the tracker camera. For this reason, it was necessary to open the UVPI door to gather data for sparse field analysis of the plume camera. Very low intensity nightglow observations were used to generate a few widely spaced photoevents per image frame at MCP gain step 13. Table 16 summarizes the results. A window size of  $S = 7$  was adopted because it is small enough to provide a tight fit of the individual photoevent, but large enough to suppress the tail contributions of photoevents from being counted as individual photoevents. For this window size, it can be seen that the preflight estimate is 1.18 times larger than the inflight estimate. The reason for this improved sensitivity is unknown.

Table 16 - Plume Camera  $G_{13}$  Gain Conversion Factor Estimates

Data Set	No. of PEs Used For Estimation	Gain Level	$G_{13.5}$ (DN/PE)		
			S=3	S=5	S=7
385_4B1010D7FL2Z_WILIS (preflight)	2000	13	194.96	233.65	261
UVPI pass 2089 (inflight)	389	13	165.85	203.21	222

Figure 50 shows the average spatial and amplitude response generated on the plume camera CCD by a photoevent in the MCP when a window size of 7 by 7 is used for estimation. This result was derived from the inflight data set, UVPI pass 2089. The area under this curve corresponds to the MCP gain conversion factor at gain step 13, i.e.,  $G_{13}$ .

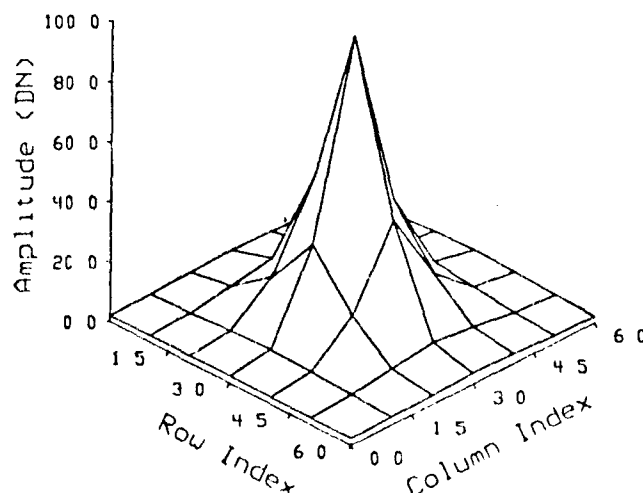


Fig. 50 - Plume camera response to a single photoevent at gain step 13, neglecting dark background

Sparse field analysis of the tracker camera was performed with the sensor door closed. Since most of the dark current images evident at high MCP gain are generated at the photocathode, it is possible to measure  $G_g$  at MCP gain step 15 by summing the pixel values in a dark current electron image and assuming that the sum was caused, most likely, by a single dark current electron released from the photocathode. Table 17 summarizes the results obtained on the tracker camera. For the same reasons given for the plume camera analysis, a window size of  $S = 7$  was adopted. For this window size, it can be seen that the preflight estimate is 1.07 times larger than the inflight estimate.

Table 17 - Tracker Camera  $G_{15}$  Gain Conversion Factor Estimates

Data Set	Gain Level	$G_{15,S}$ (DN/PE)	
		S=5	S=7
361_cdrk.t15 (preflight)	15	134.43	148.73
UVPI Pass 2076 (inflight)	15	128.13	139.51

In summary, the shape of the  $G_g$  curve was measured by ITT prior to launch, and the value of  $G_g$  at gain step 15 for the tracker camera was measured directly on-orbit by using the sparse field analysis method described. The resulting plume-camera gain conversion factors are shown in Table 18 and Fig. 51, and the gain conversion factors,  $G_g$ , for the tracker camera are shown in Table 19 and Fig. 52. The value of  $G_g$  at MCP gain step 13 for the plume camera was determined by using the sparse field analysis procedure discussed, and the shape of the curve was based on ITT's measurements. Note that the  $G_g$  values at a given gain setting are higher for the plume camera than those at the same setting for the tracker camera.

Table 18 - Plume Camera Gain Conversion Factors

Gain Step $g$	$G_g$ (DN/PE)
0	4.171E-02
1	5.735E-02
2	1.043E-01
3	1.616E-01
4	2.607E-01
5	5.840E-01
6	1.470E+00
7	3.533E+00
8	7.928E+00
9	1.670E+01
10	3.584E+01
11	6.144E+01
12	1.199E+02
13	2.220E+02
14	3.420E+02
15	4.527E+02

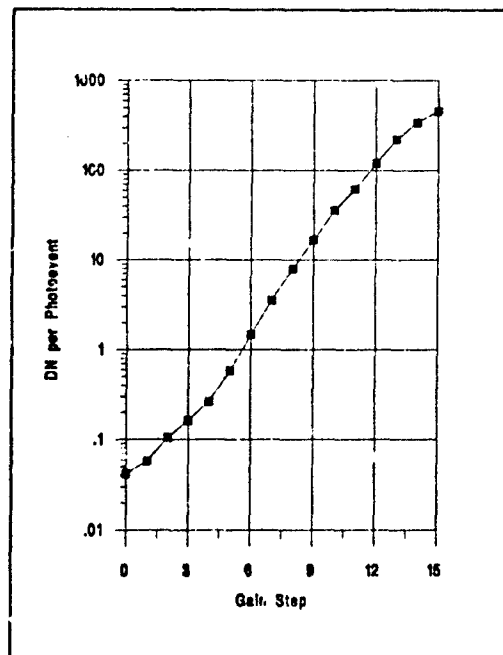


Fig. 51 - Plume-camera gain conversion factors

Table 19 - Tracker Camera Gain Conversion Factors

Gain Step G	$G_t$ (DN/PE)
0	2.199E-03
1	4.227E-03
2	9.131E-03
3	1.928E-02
4	4.025E-02
5	9.199E-02
6	1.725E-01
7	3.230E-01
8	7.068E-01
9	1.380E+00
10	2.655E+00
11	5.631E+00
12	1.172E+01
13	2.937E+01
14	5.265E+01
15	1.395E+02

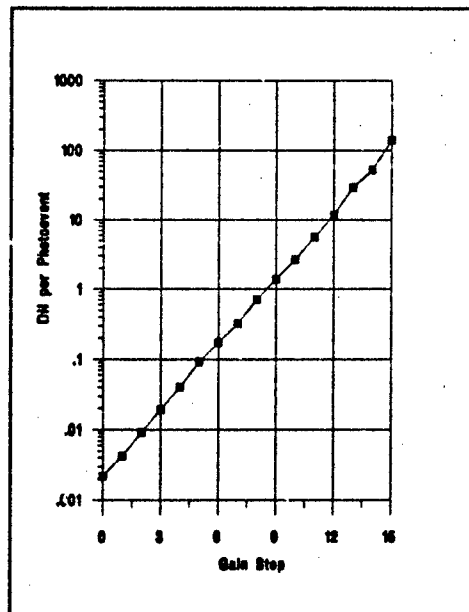


Fig. 52 - Tracker-camera gain conversion factors

## 5.2. Derivation of On-Orbit Net Quantum Efficiency Functions

### *Laboratory Measurement of Net Quantum Efficiency Wavelength Dependence*

Prior to launch, a series of measurements were made at Loral Electro-Optic Systems to determine the wavelength-dependent net quantum efficiency of the UVPI. The measurements were made without the UVPI door mirror in place. Five net quantum efficiency curves were provided by Loral ( $\beta_i(\lambda)$   $i = 0, 1, \dots, 4$ ); one for the tracker camera, and four for the plume camera. Since the UVPI functions as a relatively broadband photometer rather than as a spectrometer, no measurement of the wavelength-dependent shapes of the net quantum efficiency curves can be made on-orbit, and, therefore, the shapes measured at Loral must be used.

The following subsections discuss how the curves measured at Loral were adjusted to match on-orbit star measurements. Since star measurements were made with the UVPI door mirror in place, the wavelength-dependent reflectivity of the door mirror is incorporated into the net quantum efficiency shape before adjustment to match star measurements. The wavelength-dependent reflectivity of the door mirror,  $r(\lambda)$  as specified by Loral [13], is shown in Fig. 53 and in Table 20.

### *Stellar Emission Spectra*

UVPI measurements of known stars must be compared with similar measurements from other well calibrated sensor systems. Currently, spectral data are available from the International Ultraviolet Explorer (IUE) [14] and Orbiting Astronomical Observatory (OAO-2) [15] satellites. In addition, longer wavelength ground-based data spanning the Balmer discontinuity (at approximately 380 nm) is used in the tracker camera calibration [16].

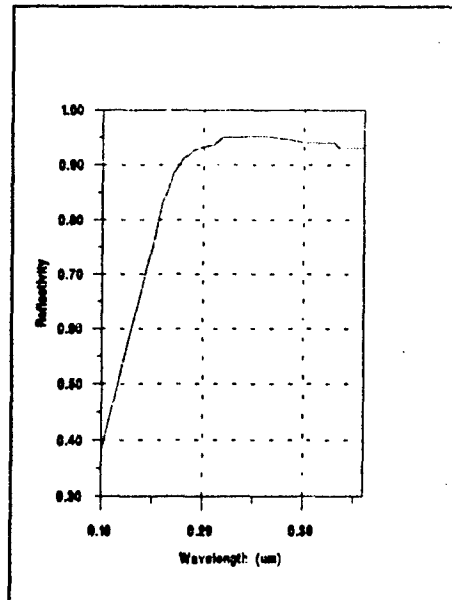


Fig. 53 - Wavelength-dependent reflectivity of UVPI door mirror

Table 20 - Wavelength Dependent Reflectivity of UVPI Door Mirror

$\lambda(\text{nm})$	$r(\lambda)$	$\lambda(\text{nm})$	$r(\lambda)$	$\lambda(\text{nm})$	$r(\lambda)$	$\lambda(\text{nm})$	$r(\lambda)$
190	0.383	270	0.91	330	0.95	390	0.94
200	0.457	275	0.918	335	0.951	395	0.94
210	0.531	280	0.926	340	0.952	400	0.94
220	0.604	285	0.929	345	0.952	405	0.94
230	0.678	290	0.932	350	0.952	410	0.94
235	0.715	295	0.934	355	0.951	415	0.94
240	0.749	300	0.936	360	0.95	420	0.94
245	0.79	305	0.943	365	0.948	425	0.93
250	0.832	310	0.95	370	0.947	430	0.93
255	0.853	315	0.95	375	0.946	435	0.93
260	0.884	320	0.95	380	0.944	440	0.93
265	0.897	325	0.95	385	0.942	445	0.93
						450	0.93

### Predicted UVPI Star Response

Well-calibrated spectral irradiance measurements for known stars are used to determine the expected number of photoevents (photoelectrons registered in the MCP) collected during a given integration time. The conversion from wavelength-dependent photon flux to photoevents per unit integration time is accomplished by using the Loral net quantum efficiency curves. Photoevents are the basic quantity counted by the instrument and, as such, can be used to estimate the photon shot noise.

Given Loral's laboratory-measured net quantum efficiency of the UVPI sensor,  $\beta_i(\lambda)$ , and a known star spectral irradiance,  $\Phi_s(\lambda)$ , with units  $\text{ergs cm}^{-2} \text{s}^{-1} \mu\text{m}^{-1}$ , the UVPI response in photoevents per frame can be predicted from

$$P_{s,i}^* = A_{opt} \cdot \tau \cdot \int_{\Delta\lambda_i} \Phi_s(\lambda) \cdot \frac{\lambda}{hc} \cdot [r(\lambda) \cdot \beta_i(\lambda)] d\lambda \quad (\text{PE}). \quad (22)$$

Here,  $\Delta\lambda_i$  is the spectral bandwidth (microns) for filter number  $i$ ,  $i = 0, 1, 2, 3, 4$  with  $i = 0$  representing the tracker camera,  $A_{opt}$  is the effective optical aperture ( $\text{cm}^2$ ), and  $\tau$  is the integration or exposure time (seconds) for a single frame. The door mirror reflectivity  $r(\lambda)$  was incorporated into the above expression because the door mirror is used for star observations and Loral's net quantum efficiency (NQE) functions  $\beta_i(\lambda)$  were measured without the UVPI door mirror in place.

### Measured UVPI Star Response

Using the same star for which  $P_{s,i}^*$  was predicted, the UVPI measurement in units of digital numbers is estimated by correcting for dark field and nonuniformities, integrating over the star spatial region of support, and computing the average over  $N$  frames as:

$$Q_{s,i}^*(\bar{x}_{k_0}) = \frac{1}{N} \sum_{n=1}^N \left\{ \sum_{\bar{x}_k \in \Gamma(\bar{x}_{k_0})} \left[ \frac{Q_i(\bar{x}_k, t_n) - D_k}{U_k} \right] \right\} \quad (\text{DN}). \quad (23)$$

Here,

- $\bar{x}_k$  is coordinate of a point in the image plane,
- $N$  is number of frames used for frame averaging,
- $\Gamma(\bar{x}_{k_0})$  is point-spread function spatial extent around center point  $\bar{x}_{k_0}$ . In practice the region of support of the point spread function is limited to a block of 19 by 19 pixels.
- $D_k$  is pixel-based temporal average of dark fields measured during the same pass in which  $Q_{s,i}^*$  was obtained,
- $U_k$  is spatial nonuniformities (unitless) at point  $\bar{x}_k$  in the image plane. Only two nonuniformity matrices were used, one for the tracker camera and one for the plume-camera.
- $Q_i(\bar{x}_k, t_n)$  is raw scene value at pixel location  $k$  over spectral band  $\Delta\lambda_i$  and at time  $t_n$ .

### Derived Net Quantum Efficiency Functions (With Door Mirror)

Radiometric calibration constants are calculated by measuring the sensor response (DN) for a star of known spectrum and comparing with the predicted number of photoevents. As each new star is measured, the calculated gain conversion factors (DN/PE) at different MCP gain steps are compared with current  $G_g$  values to determine if adjustments are necessary, and to revise error estimates. Since the  $G_g$  values were derived in-flight by using the ground-based ITT-measured shape and the on-orbit sparse field analysis method discussed, corrections are accomplished by scaling Loral's net quantum efficiency curves  $\beta_i(\lambda)$  to predict photoevents for the DN measured at a given gain step. Hence, the in-flight derived net quantum efficiency (including door mirror) can be written as

$$\eta_{i,w}(\lambda) = k_{\beta_i} \cdot r(\lambda) \cdot \beta_i(\lambda), \quad (24)$$

where  $k_{\beta_i}$  is a scaling constant determined from the calibration star observations. The door mirror reflectivity  $r(\lambda)$  was incorporated into Eq. (24) because the door mirror is used for star observations and Loral's NQE functions  $\beta_i(\lambda)$  were measured without the UVPI door mirror in place.

For a given combination of UVPI filter, star observation, and gain level, the ratio of the UVPI star measurement to the predicted value,  $Q_{s,i}^* / (k_{\beta_i} \cdot P_{s,i}^*)$ , can be computed and compared to the gain conversion factor previously derived by using the following error function definition,

$$\begin{aligned} \epsilon_{s,i} &= \left[ \frac{Q_{s,i}^*}{A_{opt} \cdot \tau \cdot \int_{\Delta\lambda_i} \Phi_s(\lambda) \cdot \frac{\lambda}{hc} \left[ \underbrace{k_{\beta_i} \cdot r(\lambda) \cdot \beta_i(\lambda)}_{\eta_{i,w}(\lambda)} d\lambda} \right] - G_{s,i}} \right] \cdot \frac{1}{G_{s,i}} \\ &= \left[ \frac{Q_{s,i}^*}{k_{\beta_i} P_{s,i}^*} - G_{s,i} \right] \cdot \frac{1}{G_{s,i}} \end{aligned} \quad (25)$$

In Eq. (25) the constant  $k_{\beta_i}$  is used to provide a multiplicative adjustment to the shape of the laboratory-measured net quantum efficiency. Given  $s = 1, \dots, S$  calibration star observations, this constant can be estimated from a weighted sum of individual error functions, i.e.,

$$\epsilon_i = \sum_{s=1}^S a_{s,i} \cdot \epsilon_{s,i} \quad (26)$$

The weighting function  $a_{s,i}$  was defined to give more weight, in the estimation of  $k_{\beta_i}$ , to those stars for which the expected SNR is higher, i.e. stars for which the photon shot noise standard deviation is



small compared to the mean. Based on Poisson statistics, the values of the weighting functions are given by [4]:

$$a_{s,i} = \mu_{P_{s,i}} / \sigma_{P_{s,i}} = \sqrt{P_{s,i}^*} \quad (27)$$

The value of  $k_{p_i}$  can be simply found by setting  $\epsilon_i$  to zero, which gives

$$k_{p_i} = \sum_{s=1}^S \left[ \left( \frac{a_s}{\sum_j a_j} \right) \cdot \frac{1}{G_{s,i}} \cdot \frac{Q_{s,i}^*}{P_{s,i}^*} \right] \quad (28)$$

Table 21 and Figure 54 show the revised tracker-camera net quantum efficiency function (version 3) so derived for observations using the door mirror. The in-band spectral region is defined to be 255 to 450 nm; the response at the defined band limits is well below 1% of the peak response. The response longward of 450 nm is significant in some cases, as discussed in Section 5.4. The shape of the in-band function is primarily determined by the shape of the spectral filter curve, and the peak efficiency (at 355 nm wavelength) is approximately 0.02 photoevents per photon. Reference 13 provides a thorough discussion of the spectral response measurements performed at Loral. The tracker-camera net quantum efficiency function given by Ref. 13 differs from the NQE below because NQE presented here implicitly incorporates an MCP collection efficiency of approximately 50%, whereas the Loral function assumed 100% MCP collection efficiency. Also, the wavelength-dependent reflectivity of the door mirror has been included, whereas the Loral function did not include the door mirror.

Table 21 - Tracker-Camera Net Quantum Efficiency (With Door Mirror)

Wavelength (nm)	NQE (PE / photon)	Wavelength (nm)	NQE (PE / photon)
255	7.838E-06	355	1.748E-02
260	4.777E-04	360	1.633E-02
265	1.492E-03	365	1.628E-02
270	3.331E-03	370	1.586E-02
275	4.959E-03	375	1.562E-02
280	6.211E-03	380	1.615E-02
285	7.562E-03	385	1.649E-02
290	7.618E-03	390	1.579E-02
295	9.351E-03	395	1.625E-02
300	1.040E-02	400	1.627E-02
305	1.216E-02	405	1.543E-02
310	1.307E-02	410	1.562E-02
315	1.070E-02	415	1.418E-02
320	1.247E-02	420	1.418E-02
325	1.559E-02	425	1.405E-02
330	1.515E-02	430	1.380E-02
335	1.333E-02	435	1.186E-02
340	9.827E-03	440	9.394E-03
345	1.290E-02	445	1.530E-03
350	1.500E-02	450	7.478E-05

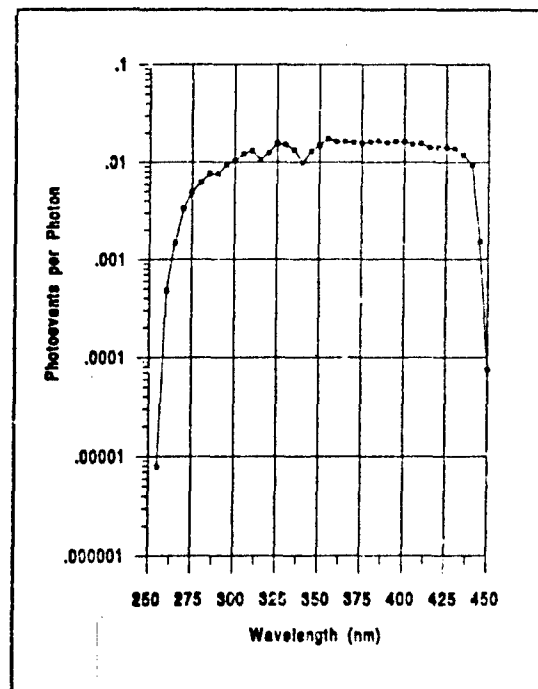


Fig. 54 - Tracker-camera net quantum efficiency curve (with door mirror)

There are four plume-camera net quantum efficiency curves, one for each filter. The curves originally determined in the laboratory have been adjusted slightly in shape by including door mirror spectral reflectivity, and in magnitude based on in-flight calibration star measurements following the procedure discussed. Results are shown in Table 22 and Fig. 55. The curves originally determined at Loral are discussed in a document prepared by Loral [13]. The results given in the Loral document differ from those shown here for three reasons:

- the Loral curves assumed 100% MCP collection efficiency, whereas for this report a collection efficiency of approximately 60% is implicitly incorporated;
- based on calibration star measurements, each of the plume camera filters were independently adjusted; and
- the Loral measurements were made without the UVPI door mirror in place, whereas values for this report were derived by using star observations with the door mirror in place.

Tables 23 and 24 summarize the stars used for calibration together with pertinent parameters such as number of frames averaged, gain step, and filter position. By using these stars and the revised net quantum efficiency curves, the predicted gain conversion factors based on calibration star measurements are shown in Figs. 56 and 57, respectively, for the tracker and plume cameras. The star-based predictions for  $G_e$  are plotted along with the directly measured tracker and plume camera  $G_e$  values presented in Figs. 51 and 52. Figure 58 demonstrates that the responsivity of the instrument has remained quite constant throughout the mission. The figure shows the ratio of predicted DN (using calibration curve) to measured DN vs pass number. There is some indication of a decrease in ratio with time but, since the decrease is quite small, its effect has been included in calibration constant error bars, rather than in time-dependent calibration constants. A single set of calibration constants is used to calibrate all UVPI data.

Table 22 - Plume-Camera Net Quantum Efficiency (With Door Mirror)

Wavelength (nm)	PC-1 (PE / photon)	PC-2 (PE / photon)	PC-3 (PE / photon)	PC-4 (PE / photon)
195			2.111E-05	
200			4.810E-05	
205			8.748E-05	
210			1.421E-04	
215	3.394E-20		2.149E-04	
220	6.509E-06		3.499E-04	
225	1.726E-05		5.644E-04	
230	3.652E-05		8.560E-04	3.154E-19
235	4.750E-05		1.220E-03	5.992E-05
240	1.076E-04		1.510E-03	3.566E-04
245	2.184E-04		1.763E-03	1.101E-03
250	5.259E-04		1.930E-03	2.062E-03
255	1.147E-03		1.876E-03	2.963E-03
260	2.412E-03		1.742E-03	4.310E-03
265	3.517E-03		1.229E-03	4.760E-03
270	3.963E-03		8.347E-04	5.974E-03
275	3.497E-03		4.779E-04	7.978E-03
280	2.533E-03		2.607E-04	8.554E-03
285	1.408E-03		1.387E-04	8.560E-03
290	6.878E-04		9.356E-05	7.823E-03
295	3.220E-04	7.558E-19	3.909E-05	7.027E-03
300	1.398E-04	3.410E-05		5.966E-03
305	6.434E-05	1.171E-03		5.074E-03
310	3.582E-05	1.037E-03		4.102E-03
315	1.024E-05	5.884E-04		3.315E-03
320	3.411E-06	1.351E-05		2.520E-03
325				1.781E-03
330				1.167E-03
335				6.600E-04
340				2.762E-04
345				7.978E-05
350				2.159E-06
355				
360				

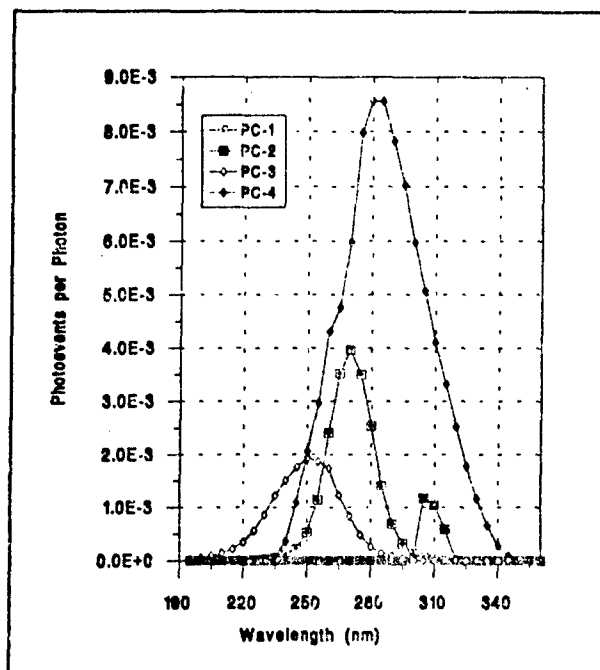


Fig. 55 - Plume-camera net quantum efficiency curves (with door mirror)

Table 23 - Plume-Camera Calibration Star Summary

Filter	Gain	Pass Number	Star	Images	Gain Conversion Factors, $G_g$ (DN/PE)	Observed DN	Predicted DN / Observed DN	Observed DN / Predicted PE
1	8	4636	$\kappa$ vel	60	7.93	6147.82	0.93	8.52
1	9	1584	$\kappa$ vel	63	16.71	10309.7	1.17	14.28
1	9	4621	$\kappa$ vel	30	16.71	13043.64	0.93	18.05
1	11	1584	HD74753	27	61.45	4672.32	1.10	55.98
1	6	5396	$\beta$ cen	65	1.47	8908.05	0.96	1.53
1	6	7324	$\beta$ cen	119	1.47	10343.98	0.83	1.78
1	10	8873	$\kappa$ eri	119	35.84	2915.34	0.88	40.58
1	8	10502	$\kappa$ vel	153	7.93	6371.74	0.90	8.82
2	11	2728	$\alpha$ col	93	61.43	2300.62	0.85	72.24
2	11	4636	$\kappa$ vel	45	61.43	5212.43	0.98	62.56
2	11	1584	$\kappa$ vel	71	61.43	3526.37	1.21	50.83
2	11	4621	$\kappa$ vel	61	61.43	4981.81	1.03	59.79
2	13	1584	HD74753	41	221.99	1514.81	1.33	166.48
2	9	5396	$\beta$ cen	65	16.71	10969.97	0.87	19.23
2	8	7324	$\beta$ cen	119	7.93	5654.19	0.80	9.91
2	12	8873	$\kappa$ eri	119	119.88	971.54	1.15	104.58
2	10	10502	$\kappa$ vel	153	35.84	3174.28	0.78	45.76
3	10	2728	$\alpha$ col	77	35.84	8253.95	0.96	37.23
3	9	4636	$\kappa$ vel	45	16.71	10940	0.92	18.11
3	9	1584	$\kappa$ vel	64	16.71	8063.32	1.25	13.34
3	9	4621	$\kappa$ vel	82	16.71	10376.9	0.97	17.17
3	11	1584	HD74753	49	61.45	4147.93	1.13	54.29
3	7	5396	$\beta$ cen	65	3.54	18949.97	0.90	3.93
3	6	7324	$\beta$ cen	150	1.47	7651.78	0.93	1.59
3	11	8873	$\kappa$ eri	119	61.45	3168.25	1.14	53.84
3	8	10502	$\kappa$ vel	149	7.93	4571.12	1.05	7.56
4	8	2728	$\alpha$ col	104	7.93	9855.23	0.88	8.96
4	7	4636	$\kappa$ vel	100	3.54	11660.53	0.85	4.17
4	7	1584	$\kappa$ vel	47	3.54	7768.49	1.25	2.83
4	9	3716	$\xi$ car	41	16.71	19461.14	1.01	16.57
4	7	4621	$\kappa$ vel	76	3.54	11066.84	0.89	3.96
4	10	1584	HD74753	29	35.84	9578.63	1.21	29.70
4	5	5396	$\beta$ cen	52	0.59	12479.97	1.01	0.57
4	9	3866	$\kappa$ eri	100	16.71	4631.44	1.03	16.29
4	4	7324	$\beta$ cen	99	0.26	6643.69	0.85	0.31
4	8	8873	$\kappa$ eri	119	7.93	2949.3	0.76	10.37
4	6	10517	$\kappa$ vel	81	1.47	4981.14	0.81	1.82
4	6	10502	$\kappa$ vel	150	1.47	4816.34	0.84	1.76

Table 24 - Tracker-Camera Calibration Star Summary

Gain	Integ. Time (s)	Pass Number	Star	Images.	Gain Conversion Factors $G_p$ (DN/PE)	Observed DN	Predicted DN / Observed DN	Observed DN / Predicted PE
7	0.019	3716	$\chi$ car	26	0.32	1061.90	1.02	0.31
6	0.012	4636	$\kappa$ vel	100	0.17	742.83	0.80	0.22
5	0.019	4621	$\kappa$ vel	115	0.09	459.37	1.11	0.08
7	0.012	597	$\kappa$ vel	24	0.32	1238.90	0.90	0.36
6	0.019	4229	$\mu$ 1 sco	66	0.17	640.88	1.07	0.18
6	0.019	4229	$\mu$ 2 sco	66	0.17	342.59	1.08	0.16
9	0.014	2728	$\mu$ col	8	1.37	686.02	1.26	1.10
3	0.019	5396	$\beta$ cen	17	0.02	904.17	0.82	0.02
3	0.015	7324	$\beta$ cen	119	0.02	778.94	0.75	0.02
6	0.012	10517	$\kappa$ vel	120	0.17	763.65	0.77	0.22
6	0.012	10502	$\kappa$ vel	151	0.17	792.84	0.74	0.23

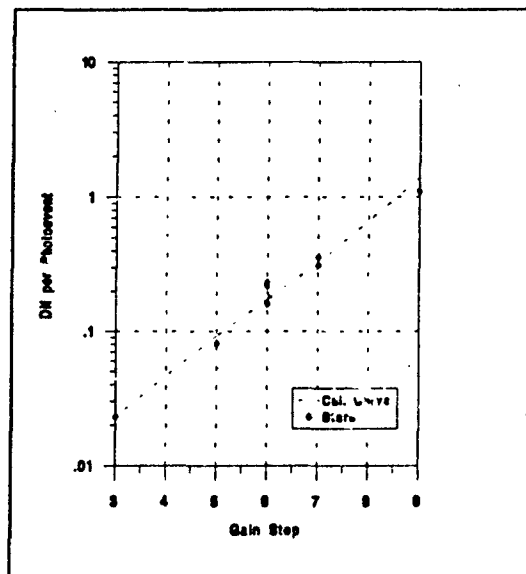


Fig. 56 - Gain conversion factors calculated by using tracker-camera star measurements

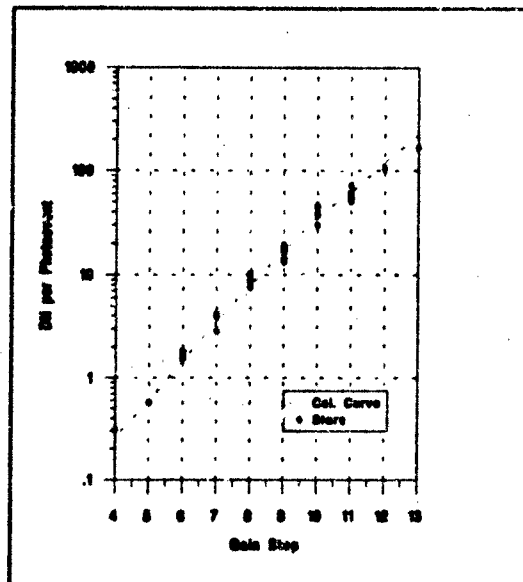


Fig. 57 - Gain conversion factors calculated using plume-camera star measurements

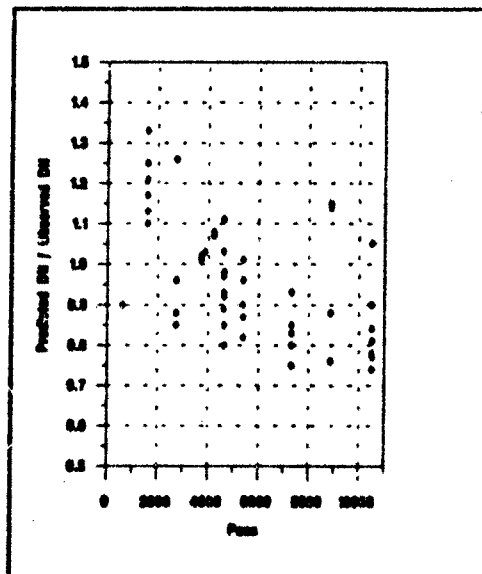


Fig. 58 - Ratio of predicted DN to observed DN vs pass number

### Derived Net Quantum Efficiency Functions (Without Door Mirror)

The net quantum efficiency functions applicable for observations made without the UVPI door mirror can be easily derived from those using the door mirror:

$$\eta_{l,w}(\lambda) = \eta_{l,w/d}(\lambda) \cdot r(\lambda) \quad (\text{photoevents per photon}), \quad (29)$$

where  $r(\lambda)$  is the wavelength-dependent reflectivity of the door mirror. Table 25 shows the tracker-camera net quantum efficiency function without the door mirror. Table 26 shows the plume-camera net quantum efficiency functions without the door mirror.

Table 25 - Tracker Camera Net Quantum Efficiency (Without Door Mirror)

Wavelength (nm)	NQE (PE / photon)	Wavelength (nm)	NQE (PE / photon)
255	9.186E-06	355	1.838E-02
260	5.404E-04	360	1.719E-02
265	1.663E-03	365	1.717E-02
270	3.660E-03	370	1.675E-02
275	5.401E-03	375	1.651E-02
280	6.708E-03	380	1.711E-02
285	8.140E-03	385	1.752E-02
290	8.174E-03	390	1.681E-02
295	1.002E-02	395	1.728E-02
300	1.111E-02	400	1.731E-02
305	1.289E-02	405	1.642E-02
310	1.377E-02	410	1.662E-02
315	1.127E-02	415	1.508E-02
320	1.313E-02	420	1.508E-02
325	1.641E-02	425	1.511E-02
330	1.595E-02	430	1.484E-02
335	1.401E-02	435	1.275E-02
340	1.032E-02	440	1.010E-02
345	1.355E-02	445	1.645E-03
350	1.576E-02	450	8.041E-05

### 5.3. UVPI Response Function Errors

The spread of star-measurement-based estimates of the gain conversion factors about the directly measured gain conversion factors represents a spread in the on-orbit measurements of the total instrument responsivity. The spread probably results from a combination of causes, including errors in the IUE and OAO spectra used to predict photoevents, uncharacterized pass-to-pass variations, changes in the net quantum efficiency functions with time, and changes in the gain conversion factors with time. Since the exact source of errors cannot be determined, and since data tapes produced by the UVPI project contain instrument measurements in units of photoevents per second, it is convenient to associate all of the errors with the gain conversion factors in order to determine a limit on the error in photoevent per second values. It should be noted that the error bars derived below are most appropriately applied to



Table 26 - Plume-Camera iNet Quantum Efficiency (Without Door Mirror)

Wavelength (nm)	PC-1	PC-2	PC-3	PC-4
195			5.026E-05	
200			1.053E-04	
205			1.771E-04	
210			2.676E-04	
215	5.980E-20		3.786E-04	
220	1.077E-05		5.794E-04	
225	2.693E-05		8.806E-04	
230	5.387E-05		1.262E-03	4.652E-19
235	6.645E-05		1.706E-03	8.379E-05
240	1.436E-04		2.016E-03	4.760E-04
245	2.765E-04		2.232E-03	1.394E-03
250	6.320E-04		2.319E-03	2.478E-03
255	1.345E-03		2.200E-03	3.474E-03
260	2.728E-03		1.971E-03	4.876E-03
265	3.922E-03		1.371E-03	5.306E-03
270	4.355E-03		9.169E-04	6.568E-03
275	3.809E-03		5.206E-04	8.690E-03
280	2.735E-03		2.815E-04	9.240E-03
285	1.515E-03		1.493E-04	9.220E-03
290	7.383E-04		1.004E-04	8.392E-03
295	3.447E-04	8.088E-19	4.186E-05	7.525E-03
300	1.494E-04	3.644E-05		6.374E-03
305	6.820E-05	1.242E-03		5.381E-03
310	3.770E-05	1.092E-03		4.318E-03
315	1.077E-05	6.193E-04		3.490E-03
320	3.591E-06	1.422E-05		2.653E-03
325				1.875E-03
330				1.229E-03
335				6.936E-04
340				2.901E-04
345				8.379E-05
350				2.268E-06
355				

irradiance values derived from UVPI measurements, not to photoevents alone. With this in mind, a simplified discussion of the estimated errors in the conversion from digital number to photoevents per second is presented in this section.

As an example, assume that a calibration star is observed during the same pass as the observation of a target of interest, e.g., a rocket plume. The number of plume-induced photoevents observed within a frame, at a given pixel, can be related to both the predicted number of photoevents for the calibration star and the digital number observed for that star by

$$P_k = Q_k \cdot \left( \frac{P_i^*}{Q_i^*} \right) \quad (\text{PE}), \quad (30)$$

where,

- $P_i^*$  is the predicted number of photoevents for a calibration star,
- $Q_i^*$  is the measured DN for the calibration star after background subtraction and nonuniformity correction
- $Q_k$  is the measured DN for the target on the  $k$ th pixel after background subtraction and nonuniformity correction, and
- $P_k$  is the estimated number of photoevents from the target on the  $k$ th pixel.

The ratio  $\left( \frac{P_i^*}{Q_i^*} \right)$  equates to the gain conversion factor  $1/G_i$ , based on a single calibration star measurement taken during a plume observation pass. It is actually the ratio of two random variables for which first and second order statistics are known from experimental data. If we assume that both  $P_i^*$  and  $Q_i^*$  can be described by using random variables with a Gaussian distribution, then the mean and standard deviation of this ratio can be obtained.

In practice, the mean and standard deviation of the PE to DN ratio is based on measurements of several calibration stars over the full range of UVPI camera gains. The numerator has a standard deviation that implicitly incorporates the IUE satellite error plus any error in the net quantum efficiency curves for the UVPI. A nominal unbiased error for IUE star data is 5 - 10% of the mean value. The denominator has a standard deviation and mean that are directly estimated from in-flight observations of calibration stars. The estimated gain conversion factor error is determined by measuring the deviations of individual calibration star measurements about a mean calibration curve (see Figs. 56 and 57).

Table 27 shows estimates of the error associated with the gain conversion factors for both plume and tracker cameras. The deviation values shown are for  $1/G_g$ , with units of photoevents per DN and, therefore, represent estimated errors in photoevent and radiometric values derived from UVPI measured DN. The average deviation values represent a best estimate of gain conversion factor errors. The maximum deviation values give a worst-case estimate. Since these values were calculated by using calibration star data gathered throughout the mission (see Fig. 58), the errors incorporate any changes in instrument responsivity over time.

Table 27 - Estimated Error in  $G_s^{-1}$  for Plume and Tracker Cameras

Camera/Filter	Average Deviation from Mean Calibration Curve	Maximum Deviation from Mean Calibration Curve
Plume, Filter 1	10.5%	17.3%
Plume, Filter 2	15.9%	33.3%
Plume, Filter 3	9.9%	25.2%
Plume, Filter 4	13.5%	24.7%
Tracker	15.6%	26.0%

#### 5.4. Out-of-band Spectral Response

Most of the tracker camera's efficiency is localized in the in-band spectral region defined. For many radiators, such as the stars selected for calibration of the instrument, most of the photoevents counted arise from radiation in the in-band spectral region. In the case of sources that peak in the infrared, however, the relatively low efficiency out-of-band can still lead to a significant response in the tracker camera; in some cases this overwhelms the in-band response. Table 28 and Fig. 59 show the net quantum efficiency of the tracker camera without the door mirror, both in-band and extended to longer wavelengths. The long wavelength values are based on a combination of laboratory measurements and conservative estimates based on manufacturer's data. Extended net quantum efficiency curves for observations using the door mirror are not available. Mirror reflectivity information is not available for wavelengths shorter than 240 nm. Details are presented in a report by Loral Electro-Optical Systems [13].

Figure 59 shows that there is a second peak in the net quantum efficiency, a factor of approximately 1000 below the in-band peak, at about 700 nm. To determine the percentage of photoevents coming from the out-of-band spectral region, the total response of the camera can be broken into two components:

$$P_{tot} = \int_{i.b.} \Phi(\lambda) \cdot \left( \frac{\lambda}{hc} \right) \cdot \tau \cdot \eta(\lambda) d\lambda + \int_{o.b.} \Phi(\lambda) \cdot \left( \frac{\lambda}{hc} \right) \cdot \tau \cdot \eta(\lambda) d\lambda. \quad (31)$$

A measure of the out-of-band response can be defined:

$$\frac{P_{o.b.}}{P_{tot}} = \frac{\int_{o.b.} \Phi(\lambda) \cdot \left( \frac{\lambda}{hc} \right) \cdot \tau \cdot \eta(\lambda) d\lambda}{\int_{i.b.} \Phi(\lambda) \cdot \left( \frac{\lambda}{hc} \right) \cdot \tau \cdot \eta(\lambda) d\lambda + \int_{o.b.} \Phi(\lambda) \cdot \left( \frac{\lambda}{hc} \right) \cdot \tau \cdot \eta(\lambda) d\lambda}. \quad (32)$$

As an example of the UVPI out-of-band response, or redleak, Table 29 tabulates  $P_{o.b.}/P_{tot}$  for blackbody radiators at various temperatures.

Table 28 - Tracker-Camera Extended NQE (Without Door Mirror)

Wavelength (nm)	PE / Photon	Wavelength (nm)	PE / Photon	Wavelength (nm)	PE / Photon	Wavelength (nm)	PE / Photon
250	1.00E-07	435	1.28E-02	620	1.13E-08	810	1.89E-05
255	1.00E-05	440	1.01E-02	625	9.45E-09	820	1.43E-05
260	5.38E-04	445	1.64E-03	630	7.66E-09	830	3.05E-05
265	1.66E-03	450	8.03E-05	635	6.39E-09	840	2.03E-05
270	3.65E-03	455	1.59E-05	640	5.00E-09	850	2.26E-05
275	5.39E-03	460	6.85E-06	645	3.79E-09	860	2.52E-05
280	6.70E-03	465	2.70E-06	650	2.94E-09	870	1.54E-05
285	8.13E-03	470	1.48E-06	655	2.39E-09	880	1.48E-05
290	8.16E-03	475	1.14E-06	660	1.61E-09	890	2.16E-05
295	1.00E-02	480	1.38E-06	665	1.18E-09	900	1.86E-05
300	1.11E-02	485	6.64E-07	670	8.45E-10	910	1.62E-05
305	1.28E-02	490	2.57E-07	675	6.74E-10	920	1.55E-05
310	1.38E-02	495	6.19E-07	680	5.47E-10	930	1.14E-05
315	1.13E-02	500	2.35E-07	685	5.04E-10	940	9.82E-06
320	1.31E-02	505	2.27E-07	690	4.65E-10	950	8.97E-06
325	1.64E-02	510	4.18E-06	695	4.62E-10	960	6.98E-06
330	1.60E-02	515	9.82E-08	700	2.28E-09	970	5.72E-06
335	1.39E-02	520	9.27E-08	705	1.80E-08	980	5.96E-06
340	1.03E-02	525	8.67E-08	710	6.65E-09	990	5.83E-06
345	1.35E-02	530	8.11E-08	715	6.57E-08	1000	4.21E-06
350	1.57E-02	535	7.56E-08	720	1.29E-08	1010	3.27E-06
355	1.83E-02	540	7.03E-08	725	6.38E-08	1020	3.11E-06
360	1.72E-02	545	6.51E-08	730	6.30E-07	1030	2.94E-06
365	1.72E-02	550	6.01E-08	735	2.90E-05	1040	2.22E-06
370	1.67E-02	555	5.52E-08	740	2.86E-05	1050	1.64E-06
375	1.65E-02	560	5.05E-08	745	1.09E-05	1060	1.39E-06
380	1.71E-02	565	4.48E-08	750	4.37E-06	1070	1.28E-06
385	1.75E-02	570	4.03E-08	755	6.27E-06	1080	1.13E-06
390	9.91E-03	575	3.69E-08	760	1.73E-05	1090	9.36E-07
395	1.71E-02	580	3.35E-08	765	2.09E-05	1100	7.78E-07
400	1.71E-02	585	2.94E-08	770	1.24E-05	1200	1.00E-07
405	1.64E-02	590	2.71E-08	775	1.55E-05	1300	1.28E-08
410	1.66E-02	595	2.30E-08	780	2.37E-05	1400	8.98E-09
415	1.50E-02	600	2.10E-08	785	1.94E-05	1500	3.86E-11
420	1.50E-02	605	1.80E-08	790	1.52E-05	1600	6.71E-13
425	1.50E-02	610	1.51E-08	795	1.88E-05	1700	2.41E-15
430	1.48E-02	615	1.32E-08	800	2.70E-05	1800	2.72E-19

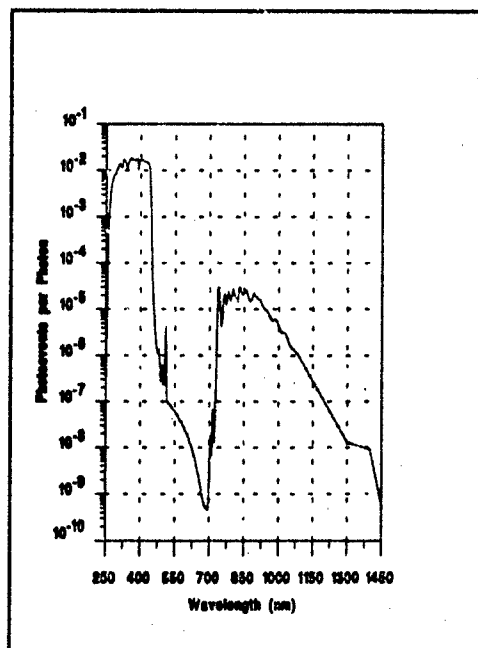


Fig. 59 - Tracker-camera extended net quantum efficiency (without door mirror)

Table 29 - Tracker-Camera Out-of-Band Contribution

Temperature (K)	Tracker Camera Approx. out-of-band response (%)
1800	95
2000	84
2100	77
2200	68
2300	58
2400	48
2500	40
2600	32
2700	26
2800	21
2900	17
3000	14
4000	2.7
5000	6.9
6000	0.5

The extended net quantum efficiency curves for each of the four plume-camera filters without the UVPI door mirror are tabulated in Tables 30 - 33. Extended net quantum efficiency estimates for observations with the door mirror in place are not available. Mirror reflectivity information is not available for wavelengths shorter than 240 nm. Table 34 tabulates  $P_{o.b.}/P_{tot}$  for blackbody radiators at various temperatures.

### 5.5. Noise Equivalent Radiance

Noise equivalent radiance (NER) is a useful measure of the detection threshold of a radiometric sensor system. Following the NER definition given in the Infrared Handbook [17], the UVPI NER is defined as the source radiance level that will result in a signal-to-noise ratio of 1 for a single pixel. In the case of UVPI, a single number does not fully characterize the detection threshold of the system because the NER is a function of integration time, spectral filter, camera gain level, number of images superposed, and the assumed source spectrum. Technically, the NER for each pixel is slightly different because the signal-independent noise associated with each pixel is slightly different. The NER values presented in this section are based on a spatial average value of the detector noise, and are accurate for all pixels at all but the very lowest gain settings where the signal-independent detector noise is most significant.

The following discussion is based on empirical estimates of the signal and noise within the UVPI cameras. Reference 18 provides a theoretical expression for the signal-power to noise-power ratio applicable to the microchannel plate image intensifier of the UVPI. A single pixel in the plume or tracker camera can be treated as a photoevent counting device. The SNR definition from which the empirical UVPI NER can be derived is:

$$SNR = \frac{M \cdot P}{\sqrt{M \cdot \sigma_n^2 + M \cdot \sigma_p^2}}, \quad (33)$$

where

- $M$  is the number of images superposed, which determines the integration time;
- $P$  is the mean number of signal-related photoevents collected in a pixel during the integration time;
- $\sigma_n$  is the signal-independent noise standard deviation for a single pixel, expressed in photoevents/image-pixel; and
- $\sigma_p$  is the signal-dependent photon shot noise standard deviation, expressed in photoevents/image.

Based on extensive measurements made on UVPI data (Section 3) the signal-dependent noise can be expressed in terms of the mean number of signal-related photoevents as  $\sigma_p = 1.6 \cdot \sqrt{P}$ . Note that this is 1.6 times the photon shot noise limit.

The signal-independent noise source is constant. When expressed in photoevents/image-pixel, its level depends on the camera gain setting used.

Table 30 - PC-1 Extended Net Quantum Efficiency (Without Door Mirror)

Wavelength (nm)	PE / Photon	Wavelength (nm)	PE / Photon	Wavelength (nm)	PE / Photon	Wavelength (nm)	PE / Photon
220	9.91E-06	305	6.74E-05	420	6.33E-10	590	1.94E-11
225	2.70E-05	310	3.83E-05	430	4.24E-10	600	1.62E-11
230	5.30E-05	315	1.13E-05	440	3.88E-10	610	1.46E-11
235	6.58E-05	320	2.84E-06	450	2.23E-10	620	1.21E-11
240	1.44E-04	325	1.83E-06	460	1.78E-10	630	1.01E-11
245	2.76E-04	330	1.07E-06	470	1.54E-10	640	7.25E-12
250	6.32E-04	335	5.28E-07	480	1.37E-10	650	5.25E-12
255	1.34E-03	340	1.78E-07	490	1.16E-10	660	4.04E-12
260	2.73E-03	345	8.76E-08	500	9.69E-11	670	3.03E-12
265	3.92E-03	350	2.56E-08	510	8.40E-11	680	2.10E-12
270	4.35E-03	355	1.39E-08	520	6.78E-11	690	1.54E-12
275	3.80E-03	360	1.02E-08	530	4.85E-11	700	1.13E-12
280	2.74E-03	370	6.24E-09	540	3.63E-11	800	4.85E-14
285	1.51E-03	380	3.80E-09	550	3.23E-11	900	4.04E-16
290	7.39E-04	390	2.05E-09	560	2.83E-11	1000	4.04E-18
295	3.45E-04	400	1.36E-09	570	2.43E-11	----	----
300	1.49E-04	410	8.61E-10	580	2.30E-11	----	----

Table 31 - PC-2 Extended Net Quantum Efficiency (Without Door Mirror)

Wavelength (nm)	PE / Photon	Wavelength (nm)	PE / Photon	Wavelength (nm)	PE / Photon	Wavelength (nm)	PE / Photon
300	3.67E-05	328	2.41E-07	460	7.99E-21	600	1.60E-21
302	4.07E-04	330	1.32E-07	470	7.58E-21	610	1.43E-21
304	1.19E-03	340	8.80E-09	480	6.78E-21	620	1.19E-21
306	1.29E-03	350	4.22E-10	490	6.38E-21	630	9.96E-22
308	1.26E-03	360	2.81E-10	500	5.99E-21	640	7.17E-22
310	1.09E-03	370	2.57E-10	510	5.19E-21	650	6.65E-22
312	9.08E-04	380	2.09E-10	520	4.79E-21	660	5.13E-16
314	8.46E-04	390	1.69E-10	530	3.99E-21	670	3.83E-13
316	3.90E-04	400	1.53E-13	540	3.59E-21	680	3.32E-11
318	6.35E-05	410	4.20E-21	550	3.19E-21	690	3.35E-10
320	1.40E-05	420	1.12E-20	560	2.79E-21	700	1.15E-09
322	3.74E-06	430	9.96E-21	570	2.40E-21	800	1.06E-14
324	1.10E-06	440	9.56E-21	580	2.27E-21	900	1.75E-17
326	4.74E-07	450	9.15E-21	590	1.92E-21	1000	2.33E-18

Table 32 - PC-3 Extended Net Quantum Efficiency (Without Door Mirror)

Wavelength (nm)	PE / Photon	Wavelength (nm)	PE / Photon	Wavelength (nm)	PE / Photon	Wavelength (nm)	PE / Photon
190	----	280	2.81E-04	380	1.58E-09	560	1.05E-11
195	4.95E-05	285	1.49E-04	390	9.64E-10	570	9.06E-12
200	1.05E-04	290	1.01E-04	400	5.63E-10	580	8.57E-12
205	1.78E-04	295	4.24E-05	410	3.43E-09	590	7.23E-12
210	2.67E-04	300	1.39E-05	420	2.53E-10	600	6.03E-12
215	3.79E-04	305	5.72E-06	430	1.89E-10	610	5.43E-12
220	5.79E-04	310	4.03E-06	440	1.62E-10	620	4.52E-12
225	8.74E-04	315	2.65E-06	450	1.39E-10	630	3.77E-12
230	1.27E-03	320	1.59E-06	460	9.06E-11	640	2.71E-12
235	1.71E-03	325	8.57E-07	470	7.19E-11	650	1.26E-12
240	2.02E-03	330	3.76E-07	480	5.13E-11	660	1.51E-12
245	2.23E-03	335	1.89E-07	490	3.62E-11	670	1.13E-12
250	2.32E-03	340	6.65E-08	500	2.26E-11	680	7.84E-13
255	2.20E-03	345	3.28E-08	510	1.96E-11	690	5.73E-13

Table 33 - PC-4 Extended Net Quantum Efficiency (Without Door Mirror)

Wavelength (nm)	PE / Photon	Wavelength (nm)	PE / Photon	Wavelength (nm)	PE / Photon	Wavelength (nm)	PE / Photon
230	----	310	4.32E-03	420	2.86E-10	560	2.04E-13
235	8.32E-05	315	3.50E-03	430	6.39E-10	590	7.83E-13
240	4.78E-04	320	2.66E-03	440	4.91E-10	600	2.70E-12
245	1.40E-03	325	1.88E-03	450	1.06E-09	610	3.46E-12
250	2.48E-03	330	1.23E-03	460	5.11E-10	620	2.88E-12
255	3.48E-03	335	6.94E-04	470	3.89E-10	630	2.81E-12
260	4.88E-03	340	2.91E-04	480	3.48E-10	640	1.84E-11
265	5.32E-03	345	8.32E-05	490	1.64E-10	650	1.33E-10
270	6.57E-03	350	3.24E-06	500	1.23E-10	660	2.05E-09
275	8.68E-03	355	5.87E-07	510	6.64E-11	670	7.62E-09
280	9.24E-03	360	1.44E-07	520	6.13E-11	680	3.72E-08
285	9.24E-03	370	2.63E-08	530	5.11E-11	690	1.16E-07
290	8.39E-03	380	9.59E-09	540	4.60E-11	700	1.29E-07
295	7.55E-03	390	3.47E-09	550	4.09E-11	800	3.07E-09



Table 34 - Plume Camera Out-of-Band Contribution

Temperature (K)	PC-1 %	PC-2 %	PC-3 %	PC-4 %
1800	1.4	24	7.0	74
2000	0.4	6.9	1.8	40
2100	0.2	3.8	1.0	27
2200	0.1	2.2	0.5	17
2300	---	1.3	0.3	11
2400	---	0.8	0.2	7.2
2500	---	0.6	0.1	4.7
2600	---	0.4	---	3.2
2700	---	0.3	---	2.2
2800	---	0.2	---	1.6
2900	---	0.1	---	1.1
3000	---	0.1	---	0.8

From this SNR expression, it can be shown that the mean number of signal-related photoevents/image in a pixel that will result in a SNR of 1 is given by

$$P_{SNR=1} = \frac{(1.6)^2}{2 \cdot M} \left( 1 + \sqrt{1 + \frac{4 \cdot M \cdot \sigma_n^2}{(1.6)^4}} \right) = \frac{1.28}{M} \left( 1 + \sqrt{1 + \frac{M \cdot \sigma_n^2}{1.64}} \right) \quad (\text{PE}) \quad (34)$$

Notice that for the case of only one superposed image,  $M = 1$ , and a negligible level of sensor noise,  $\sigma_n$ , the resulting sensitivity limit is 2.6 photoevents/image. As can be seen in Table 35, this is the case for single images at relatively high gain, where  $\sigma_n$  is indeed negligible compared with signal-dependent noise,  $\sigma_p$ . At high gain steps, superposition of  $M$  images decreases (improves) the noise equivalent signal,  $P_{SNR=1}$ , by approximately a factor of  $M$ . At low gain steps, the signal-independent detector noise dominates signal-dependent noise, and superposition of  $M$  images decreases (improves) the noise equivalent signal,  $P_{SNR=1}$ , by approximately a factor of  $\sqrt{M}$ . The noise equivalent signal can also be improved by performing spatial averaging, at the expense of a lower spatial resolution.

The NER is related to  $P_{SNR=1}$  by a multiplicative constant  $K_\Phi$ , i.e.,

$$NER = K_\Phi \cdot P_{SNR=1} = \frac{1.28 \cdot K_\Phi}{M} \left( 1 + \sqrt{1 + \frac{M \cdot \sigma_n^2}{1.64}} \right) \quad (\mu\text{W}/\text{sr} \cdot \text{cm}^2) \quad (35)$$

where  $K_\Phi$  is the radiometric calibration constant which converts from photoevents/image to  $\mu\text{W}/\text{sr} \cdot \text{cm}^2$ .  $K_\Phi$  is a function of the spectral filter used, the single image exposure time, and the assumed source spectrum.

Table 35 - Noise Equivalent Signal for Single Images

Gain Step	Tracker Camera Noise Equivalent Signal (PE/image-pix)	Tracker Camera Noise Equivalent Signal* (PE/sec-pix)	Plume Camera Noise Equivalent Signal (PE/image-pix)	Plume Camera Noise Equivalent Signal (PE/sec-pix)
0	848.97	25469.36	43.88	1316.27
1	442.27	13268.10	32.27	968.14
2	205.43	6163.04	18.36	550.76
3	97.99	2939.65	12.34	370.25
4	47.61	1428.41	8.21	246.35
5	21.58	647.52	4.58	137.38
6	12.16	364.88	3.04	91.19
7	7.19	215.74	2.66	79.66
8	4.21	126.34	2.58	77.38
9	3.14	94.23	2.56	76.93
10	2.74	82.20	2.56	76.83
11	2.60	78.06	2.56	76.81
12	2.57	77.12	2.56	76.80
13	2.56	76.86	2.56	76.80
14	2.56	76.83	2.56	76.80
15	2.56	76.81	2.56	76.80

\*Assuming 1/30th second integration time.

## 5.6. Extraneous Signals

### Out-of-Field Contributions

Scattering from sources beyond the FOV is a substantial problem for any UVPI data taken during the daytime in the limb or nadir directions. A high degree of off-axis scattering, which is not unexpected from a camera without baffles, severely modifies the background against which any radiometric measurement is being made. Typically for the plume camera, intensity factors of 50 to 100 times that expected are caused by large, bright, nearby light sources when viewing limbward or for nadir viewing. Similar effects are found for the tracker camera.

The most thorough examination of off-axis scattering was reported by Romick et al. [19] from Johns Hopkins University Applied Physics Laboratory (APL) who were also trying to evaluate the red-leakage effects to retrieve measurements of daytime clutter.

In assessing the effect of off-axis scattering, the APL group analyzed a daytime limb pass with successive plume and tracker camera images obtained as the limb was scanned from 85 to 160 km altitude with limb solar zenith angles between 75° and 85°. Between 85 and 110 km the background Rayleigh scattered signal is expected to decrease with increasing altitude in proportion to the decrease in molecular density that has a scale height of approximately 7 km. However, the observed plume camera intensity decreases with a scale height of 9 - 11 km. This slower decrease in intensity implies that the lower bright atmosphere, beyond the normal field of view, is contributing to the signal.

Off-axis scattering was found not to have a significant effect on the nighttime UVPI observations, including star and rocket plume observations.

### *Doughnut Shape in Tracker Camera*

Occasionally, a region of enhanced emission, approximately annular in shape, appears in the tracker camera. The shape tends to be distorted from a simple annulus. The amplitude from the brightened region can be as large as 5 DN. The effect is apparent only in the tracker camera.

Referring back to Fig. 6, when additional data reduction was done on special observations (such as nightglow observations), the doughnut, as it was usually referred to, was treated as another component of background. For example, in a report [20] describing nightglow data, it was estimated that the doughnut contributed less than 2 kilorayleighs compared to the nightglow peak intensity of 80 kilorayleighs.

In at least one set of data where gain levels were changed frequently, over short time intervals it was found that the doughnut appears to be gain-step independent. No data contradicting this have been found.

During ground tests, a doughnut-shaped image could be produced by using a small, light source in the out-of-focus nearfield of the telescope. In fact, the spiders supporting the primary mirror could be made visible through this process, which seemed to shadow-cast the primary mirror onto the image plane to produce the doughnut. Moving the source from side to side caused the annulus-shaped image to distort, as it is distorted in flight. This doughnut-shaped image, however, was not gain independent.

It has been speculated that a reflecting surface could scatter light, causing the doughnut shape seen in flight. It is hard to extend this concept, or any concept, to explain a gain-independent doughnut, however. Transmission through or past the MCP without electron gain might be possible for photons, but how they would then interact with the phosphor, or CCD directly, is not clear.

### **5.7. Response Transients**

The following three subsections address transients introduced into the data by mechanical, electrical, and software effects, which can affect the calibration and analysis of the UVPI images.

#### *Filter Wheel Rotation Effects*

The plume camera has four filters mounted on a wheel. The filter wheel rotates on command, but it cannot rotate continuously in one direction. The wheel movement allows the following filter transitions: PC - N to PC - (N + 1) for N = 1, 2, 3 and PC - N to PC - (N - 1) for N = 4, 3, 2.

Based on experience in flight, the filter wheel, on average, takes approximately 1.53 s to rotate to an adjacent filter position. This is the equivalent of 7 or 8 images when the normal image transmission rate is used or approximately 46 images when the zoom image transmission rate is used. While the filter wheel is moving, the filter wheel position indicator in the telemetry does not contain accurate filter wheel position information. Generally, an indication that filter wheel rotation may be occurring can be found by looking at the tracker camera integration time field in the telemetry. When a filter wheel rotation is occurring, the tracker camera integration time field value will be zero. In the routine processing of the UVPI data, frames for which the tracker-camera integration time field value is zero because of a filter wheel rotation are flagged in the image header. Also, because the filter wheel position indicator is telemetered at a low rate, a lag of several frames often occurs before movement to the new position is properly indicated. Although the filter wheel position indicator provides an incorrect filter position identification, the frames collected after movement has stopped can be good data frames.

### *Door Motion Effects*

The door covering the UVPI aperture moves on command. The telemetered door position indicator has a value of  $0^\circ$  when the door is completely closed, and  $137.52^\circ$  when the door is fully open. Transition in either direction between completely closed and fully open takes 27 to 28 s. Motion in either direction between either extreme and a midrange position (for which the door position indicator value is in the  $47^\circ$  to  $56^\circ$  range) takes 13 to 14 s. Motion within this midrange, which is used for both star and limb observations, generally takes approximately 1 s. Generally, an indication that door motion may be occurring can be found by looking at the tracker-camera integration time field in the telemetry. When door motion is occurring, the tracker-camera integration time field value will be zero. In the routine processing of the UVPI data, frames for which the tracker-camera integration time field value is zero because of door motion are flagged in the image header.

Because the door position indicator is telemetered at a low rate, a lag of several frames often occurs after door motion has stopped before the new position is properly indicated. Although the door position indicator provides an incorrect door position identification, the frames collected after movement has stopped can be good data frames.

### *Automatic Gain Control Response Effects*

The UVPI has significant response time in reacting to sudden changes of brightness in the camera's field of view (FOV). When a sudden change in brightness occurs, the AGC requests an appropriate gain change. The speed with which the requested gain change occurs for a camera is limited to one gain step per image transmitted or stored in the UVPI tape recorder. Therefore, the camera favored by the plume to tracker image ratio will be able to accomplish requested gain changes more rapidly. For example, if a 8:2 image ratio favoring the plume camera were selected, the plume camera could change gain by a maximum of 8 steps and the tracker camera by a maximum of 2 steps in the 2 s during which 10 images were transmitted at the zoom image transmission rate.

Observations during revolutions 597 and 10517 have been selected to show how a camera's gain changes as a dominant bright star enters or leaves its FOV. A bright star suddenly entering or leaving the FOV could be considered a step function, to which the AGC reaction could be viewed as a step response. The camera's response is shown by considering both the value of the brightest pixel of each calibrated image and the sum of the values in an  $N$  array of pixels around this brightest pixel.

During observation 10517, a bright star moves into the FOV of the tracker camera, then out of the FOV, and then back into the FOV in frames 5512, 5878 and 5992, respectively. During the same observation, the star moves into the FOV of the plume camera in frame 8170. The plume to tracker image ratio over this interval of frames is 2:8. Figure 60 shows the value for the brightest pixel; Fig. 61 shows the sum of the values for a 7 by 7 array of pixels centered on the brightest pixel, for tracker-camera frames 5453 through 5944. As the bright star moves into the FOV in frame 5512, the AGC requests a change in gain from step 9 to step 3. As the star comes more fully into the FOV in the next frame, a change in gain from step 8 to step 6 is requested. The gain settles at step 6 by frame 5542. The AGC and the camera reacted as designed by going from gain step 9 to gain step 6 and settling within 5 normal transmission rate images. Note that the frame number jumps by 6 for consecutive images at normal transmission rate because 6 frames are transmitted for each image. The fluctuations seen in the values of the brightest pixel and the pixel array are attributed to pixel registration and fluctuations in focal plane response.

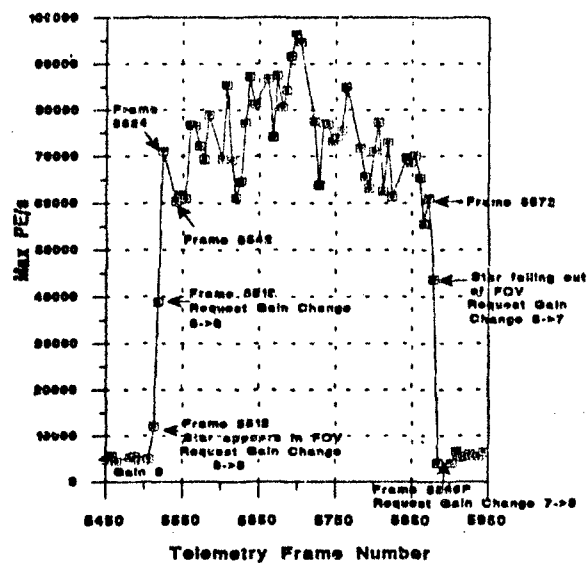


Fig. 60 - Tracker-camera step response to a star (PE/s for brightest pixel)

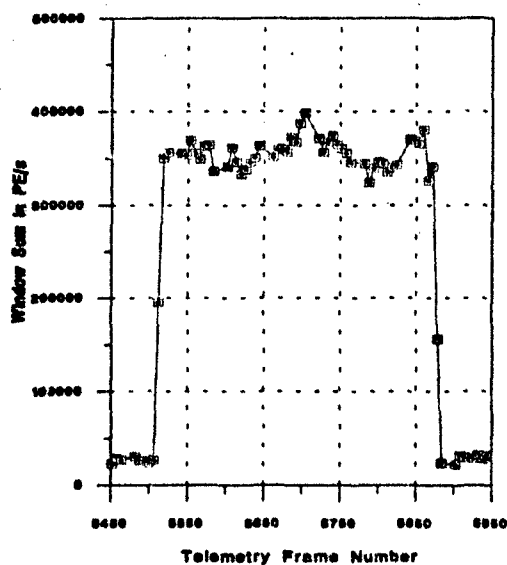


Fig. 61 - Tracker-camera step response to a star (PE/s for sum of pixels)

Figures 62 and 63 correspond to Figs. 60 and 61 except that the frame range is now 5962 through 6402. The star enters the left side of the FOV of the tracker camera in frame 5992, causing a request for a change in gain from step 9 to step 7. In the next frame the star has fully entered the FOV and gain step 6 is requested by the AGC. By frame 6022, the gain has stabilized at step 6. The overshoot at frame 5998 in Fig. 63 may be caused by the assumption of gain step 7 for data processing when step 8 may have been the correct step. The overshoot is not seen in Fig. 62 because of pixel saturation. Again, the AGC and camera reacted as designed, going from gain step 9 to gain step 6 and stabilizing in 5 images. Figures 62 and 63 each show a dip in values at frame 6358. This dip was caused by motion of the star's image to the edge of the FOV. The decrease was not sufficient to cause a gain change request, and the image was more fully within the FOV in the next frame.

Figures 64 and 65, respectively, show the brightest pixel and the sum of the values for a 25 by 25 array of pixels centered on the brightest pixel for the plume camera for frames 8050 through 3496. The star first appeared in the FOV of the plume camera in frame 8170. Prior to the arrival of the star's image in the FOV, the gain was at step 13. The gain stabilized at step 6 in frame 8355. This represents a 7-step gain change in 31 images for the plume camera. The tracker camera accomplished a 3-step gain change in 5 images. The relatively slower response of the plume camera to the AGC gain change request is explained by the 2.8 plume to tracker image ratio selected for these frames.

During observation 597, a bright star moves into the FOV of the plume camera in frame 4696 and exits at frame 4948. During this interval the plume to tracker image ratio was 1:1. Figures 66 and 67, respectively, show the brightest pixel and the sum of the values for a 11 by 11 array centered on the brightest pixel. The gain changes from step 13 to step 11 within a few frames, stays at step 11 for a few more frames, and then changes to step 10. After the star leaves the FOV, the gain changes from step 10 to step 13 within 4 frames. The fluctuations seen in the values of the brightest pixel and the pixel array are attributed to pixel registration and fluctuations in focal plane response.

## 6. ON-ORBIT AND LABORATORY-MEASURED RESPONSE FUNCTIONS

The final UVPI calibration results, version 3, have been presented in the preceding sections. The version 3 calibration is based on a combination of laboratory and on-orbit measurements. It has benefited from further analysis of sensor data since publication of rocket plume reports [8-11] and delivery of data tapes to the SDIO data centers. Before version 3, the UVPI calibration had progressed through two versions: version 1, the calibration performed entirely in the laboratory prior to launch, and version 2, the calibration used for UVPI data tapes and rocket plume reports. This section summarizes the history of the UVPI calibration process, compares the current version 3 calibration with the laboratory calibration, and provides simple constants for revising UVPI data tape and rocket plume report results based on version 2 to more accurate version 3 results.

### 6.1. History of Response Function Derivation

Table 36 shows the UVPI calibration history. It is important to realize that although several assumptions were made in the version 2 calibration used for data tapes and rocket plume reports, the overall responsivity of the UVPI, with units of DN per photon, was measured directly by using calibration stars. Assumptions concerning MCP collection efficiency and the correct amplitude of the PC-1 NQE function affect determination of photoevents, which is an intermediate result, but not the determination of source radiant intensity or radiance results. An important omission in the version 2 calibration is the lack of distinction between UVPI observations with and without the door mirror.

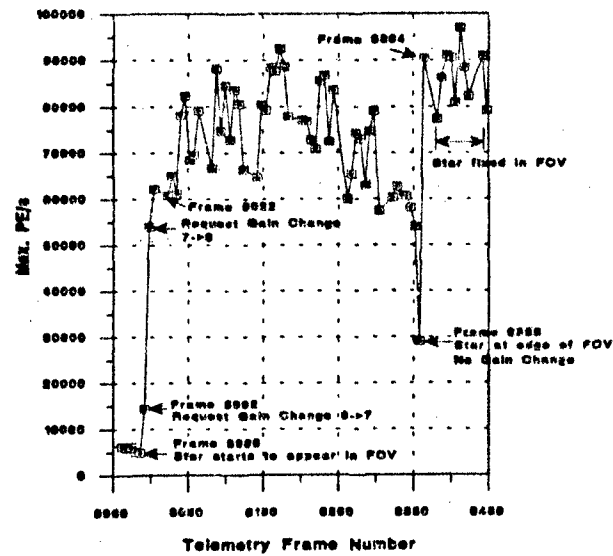


Fig. 62 - Tracker-camera step response to a star (PE/s for brightest pixel)

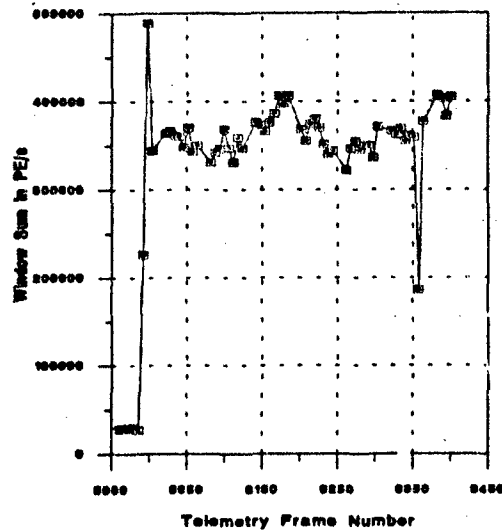


Fig. 63 - Tracker-camera step response to a star (PE/s for sum of pixels)

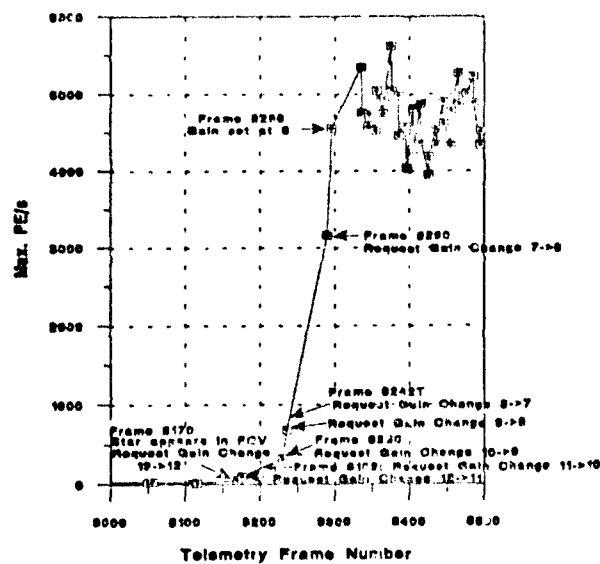


Fig. 64 - Plume-camera step response to a star (PE/s for brightest pixel)

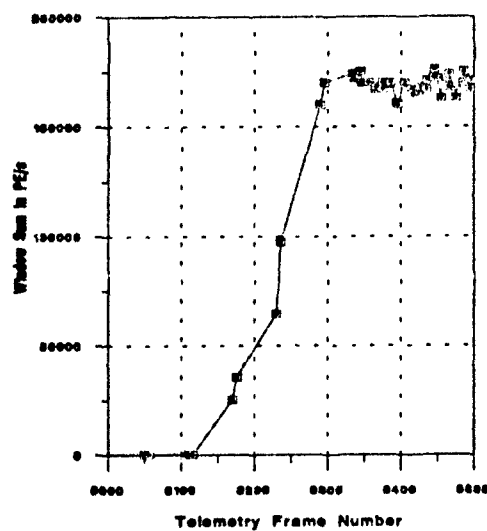


Fig. 65 - Plume-camera step response to a star (PE/s for sum of pixels)



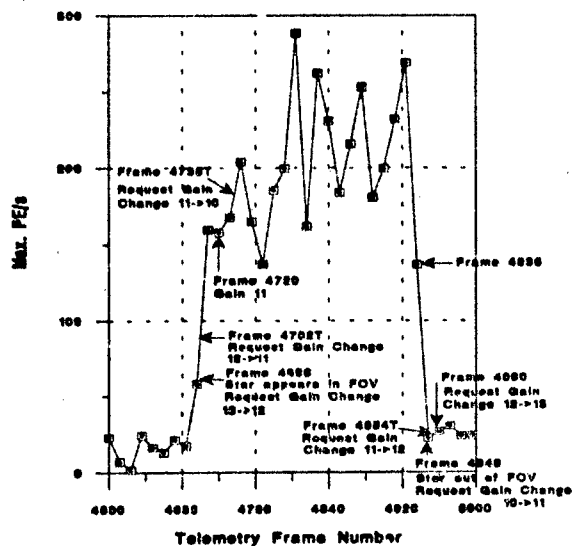


Fig. 66 - Plume-camera step response to a star (PE/s for brightest pixel)

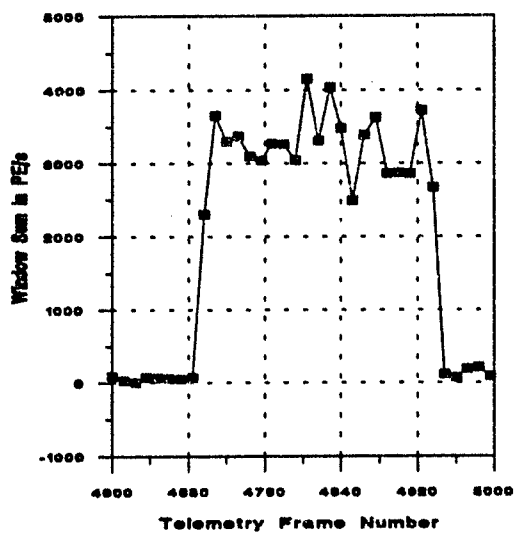


Fig. 67 - Plume-camera step response to a star (PE/s for sum of pixels)

Table 36 - UVPI Calibration History

Laboratory (Loral / ITT / NRL)	On-orbit Calibration Version 2 (used for data tapes and reports)	On-orbit Calibration Version 3 (revised calibration)
<b>Net Quantum Efficiency (Photoevents per Photon)</b>		
<ul style="list-style-type: none"> <li>Loral measured NQE directly assuming 100% MCP collection efficiency</li> </ul>	<ul style="list-style-type: none"> <li>derived from Loral's NQE shapes using IUE star spectra and UVPI star measurements</li> <li>assumed MCP collection efficiency of 75%</li> <li>the magnitude of the Loral PC-1 NQE curve was not adjusted to match star measurements, but the other NQE curves were adjusted</li> <li>same NQE curve was used for observations with and without the door mirror</li> </ul>	<ul style="list-style-type: none"> <li>derived from Loral's NQE shapes using IUE star spectra, UVPI star measurements, and improved gain conversion factor estimates</li> </ul>
<b>Gain Conversion Factor (DN per Photoevent)</b>		
<ul style="list-style-type: none"> <li>ITT measured shape of gain conversion factor</li> <li>sparse field measurements were made at NRL but were not analyzed</li> </ul>	<ul style="list-style-type: none"> <li>derived from ITT's gain conversion factor shape using IUE star spectra and UVPI star measurements</li> <li>assumed MCP collection efficiency of 75%</li> <li>assumed Loral's PC-1 NQE curve was correct</li> </ul>	<ul style="list-style-type: none"> <li>derived from ITT's gain conversion factor shape using on-orbit sparse field measurements</li> <li>NRL laboratory sparse field measurements were analyzed for comparison with on-orbit measurements</li> </ul>

The version 3 calibration requires no assumptions concerning MCP collection efficiency or NQE function amplitude. This is possible because the gain conversion factor is specified directly by ITT measurements of its shape and by sparse field measurements fixing its amplitude. The overall responsivity of the UVPI, i.e., the DN per second caused by the incident photons per second in the bandpass, is also specified directly using calibration star measurements. Therefore, the NQE function shapes can be adjusted to the correct amplitude with units of photoevents per photon. Also, the distinction between UVPI observations with and without the door mirror is made in the version 3 calibration.

The following sections show that the difference between results based on laboratory, on-orbit version 2, and on-orbit version 3 instrument responsivity is relatively small.

## 6.2. Comparison of Version 3 and Laboratory Calibration

This section compares the on-orbit version 3 and laboratory calibrations. Since the laboratory net quantum efficiency curves were measured without the UVPI door mirror in place, the on-orbit version 3 calibration without the door mirror is used for the comparison. Table 37 lists the laboratory and on-orbit version 3 net quantum efficiency curves for comparison. The laboratory curves shown are based on the assumption that the MCP collection efficiency, photoevents per photoelectron, is 100%. These curves, in conjunction with Loral's measurements of the plume camera total responsivity, DN per photon, at low gain steps and with NRL's sparse field analysis results, DN per photoevent, specify an actual MCP collection efficiency of approximately 60% for the plume camera. The tracker camera MCP collection efficiency cannot be derived from available laboratory data. However, it is assumed to be the same as for the plume camera. Therefore, the values listed in the laboratory columns should be multiplied by 0.6 to give a meaningful comparison.

Table 38 shows the gain conversion factors measured at gain step 15 for the tracker camera, and at gain step 13 for the plume camera. For both the laboratory and on-orbit calibration, the shapes of the gain conversion factors are identical for gain steps 13 and below in the plume camera, and for gain steps 15 and below in the tracker camera. Therefore, the amplitudes of the gain conversion factors at all these gain steps are also related by the constants shown in Table 38.

The laboratory and version 3 overall UVPI responsivity, with units of DN per photon, can now be compared by multiplying the net quantum efficiency at a given wavelength by the gain conversion factor at a given gain step and adjusting laboratory values for the 60% MCP conversion efficiency. Table 39 shows the result.

Error bars associated with the on-orbit calibration are about 10 to 15% for all plume-camera filters and for the tracker camera. Error estimates were not provided with the laboratory measurements; therefore, the percent changes shown in Table 39 must be considered with caution. Almost certainly PC-2, and probably the tracker camera, changed somewhat for unknown reasons. The on-orbit response functions for PC-2 and the tracker camera were determined by using several calibration star measurements. All consistently provided a significantly different total responsivity than that measured in the laboratory. The cause of the drop in PC-2's total responsivity is not understood. However, there is some indication that degradation of the filter occurred before launch. Laboratory PC-2 flat-field images have a cloudy appearance that is not evident in flat-field images observed with the other filters. No spectral filter degradation is indicated in tracker camera flat-field images, and the evident increase in the tracker camera's total responsivity is not understood.

## 6.3. Comparison of Version 3 and Version 2 Calibration

This section will compare the on-orbit version 2 and version 3 calibrations. Since the version 2 net quantum efficiency curve shapes did not include the UVPI door mirror, the version 3 calibration without the door mirror is used for the comparison. From the discussion of sparse field measurements in section 5.1, the version 3 tracker camera gain conversion factor measured on-orbit at gain step 13 is 222 DN per photoevent. The value used in the version 2 calibration was 143.6 DN per photoevent. Therefore, the version 3 value is 1.55 times larger than the version 2 value used for UVPI data tapes and rocket plume reports. This large increase in the amplitude of the gain conversion factor is accompanied by a similar, though not identical, decrease in the amplitude of the net quantum efficiency function. Table 40 shows the on-orbit version 2 and version 3 net quantum efficiency functions for comparison.

Table 37 - Comparison of Laboratory and On-orbit Version 3 NQE Functions

$\lambda$ (nm)	Laboratory (Photoevents / Photon)					Version 3 (without door mirror) (Photoevents / Photon)				
	Tracker	PC-1	PC-2	PC-3	PC-4	Tracker	PC-1	PC-2	PC-3	PC-4
195				9.99E-05					5.03E-05	
200				2.09E-04					1.05E-04	
205				3.52E-04					1.77E-04	
210				5.32E-04					2.68E-04	
215				7.52E-04					3.79E-04	
220		2.00E-05		1.15E-03			1.08E-05		5.79E-04	
225		5.00E-05		1.75E-03			2.69E-05		8.81E-04	
230		9.99E-05		2.51E-03			5.39E-05		1.26E-03	
235		1.23E-04		3.39E-03	1.23E-04		6.65E-05		1.71E-03	8.38E-05
240		2.67E-04		4.00E-03	7.00E-04		1.44E-04		2.02E-03	4.76E-04
245		5.13E-04		4.44E-03	2.05E-03		2.76E-04		2.23E-03	1.39E-03
250		1.17E-03		4.60E-03	3.64E-03		6.32E-04		2.32E-03	2.48E-03
255	1.00E-05	2.49E-03		4.38E-03	5.10E-03	9.18E-06	1.35E-03		2.20E-03	3.47E-03
260	5.88E-04	5.06E-03		3.92E-03	7.17E-03	5.40E-04	2.73E-03		1.97E-03	4.88E-03
265	1.81E-03	7.28E-03		2.72E-03	7.81E-03	1.66E-03	3.92E-03		1.37E-03	5.31E-03
270	3.98E-03	8.08E-03		1.82E-03	9.65E-03	3.66E-03	4.35E-03		9.17E-04	6.57E-03
275	5.88E-03	7.06E-03		1.03E-03	1.27E-02	5.40E-03	3.81E-03		5.21E-04	8.69E-03
280	7.30E-03	5.08E-03		5.59E-04	1.36E-02	6.71E-03	2.74E-03		2.82E-04	9.24E-03
285	8.86E-03	2.81E-03		2.97E-04	1.36E-02	8.14E-03	1.52E-03		1.49E-04	9.22E-03
290	8.90E-03	1.37E-03		1.99E-04	1.23E-02	8.17E-03	7.38E-04		1.00E-04	8.39E-03
295	1.09E-02	6.40E-04		8.32E-05	1.11E-02	1.00E-02	3.45E-04		4.19E-05	7.53E-03
300	1.21E-02	2.77E-04	1.36E-04		9.37E-03	1.11E-02	1.49E-04	3.64E-05		6.37E-03
305	1.40E-02	1.27E-04	4.66E-03		7.91E-03	1.29E-02	6.82E-05	1.24E-03		5.38E-03
310	1.50E-02	7.00E-05	4.10E-03		6.35E-03	1.38E-02	3.77E-05	1.09E-03		4.32E-03
315	1.23E-02	2.00E-05	2.32E-03		5.14E-03	1.13E-02	1.08E-05	6.19E-04		3.49E-03
320	1.43E-02	6.66E-06	5.32E-05		3.90E-03	1.31E-02	3.59E-06	1.42E-05		2.65E-03
325	1.79E-02				2.75E-03	1.64E-02				1.89E-03
330	1.74E-02				1.81E-03	1.59E-02				1.23E-03
335	1.52E-02				1.02E-03	1.40E-02				6.94E-04
340	1.12E-02				4.27E-04	1.03E-02				2.90E-04
345	1.47E-02				1.23E-04	1.36E-02				8.38E-05
350	1.71E-02				3.33E-06	1.58E-02				2.27E-06
355	2.00E-02					1.84E-02				
360	1.87E-02					1.72E-02				
365	1.87E-02					1.72E-02				
370	1.82E-02					1.67E-02				
375	1.80E-02					1.65E-02				
380	1.86E-02					1.71E-02				
385	1.91E-02					1.75E-02				
390	1.83E-02					1.68E-02				
395	1.88E-02					1.73E-02				
400	1.88E-02					1.73E-02				
405	1.79E-02					1.64E-02				
410	1.81E-02					1.66E-02				

Table 37 - (Cont'd) Comparison of Laboratory and On-orbit Version 3 NQE Functions

415	1.64E-02					1.51E-02				
420	1.64E-02					1.51E-02				
425	1.64E-02					1.51E-02				
430	1.61E-02					1.48E-02				
435	1.39E-02					1.28E-02				
440	1.10E-02					1.01E-02				
445	1.79E-03					1.65E-03				
450	8.75E-05					8.04E-05				

Table 38 - Comparison of Laboratory and On-Orbit Version 3 Gain Conversion Factors

Camera	Gain Step	Laboratory Gain Conversion Factor	On-Orbit Version 3 Gain Conversion Factor	Ratio (Ver. 3 / Lab)
Tracker	0-15	148.7	139.5	.938
Plume	0-13	261.0	222.0	.851

Table 39 - Comparison of Laboratory and On-orbit Version 3 Total Responsivity

Filter	$\lambda$ (nm)	Gain Step	Laboratory MCP Collection Efficiency	Laboratory (DN / Photon)	Version 3 (DN / Photon)	Percent Change
Tracker	300	15	60%	1.63	2.34	43.6
PC-1	280	13	60%	.798	.608	-23.8
PC-2	310	13	60%	.642	.242	-62.3
PC-3	265	13	60%	.426	.304	-28.6
PC-4	305	13	60%	1.24	1.19	-4.0

Table 40 - Comparison of On-Orbit Version 2 and Version 3 NQE Functions

$\lambda$ (nm)	Version 2 (Photoevents / Photon)					Version 3 (without door mirror) (Photoevents / Photon)				
	Tracker	PC-1	PC-2	PC-3	PC-4	Tracker	PC-1	PC-2	PC-3	PC-4
195				6.16E-05					5.03E-05	
200				1.29E-04					1.05E-04	
205				2.17E-04					1.77E-04	
210				3.28E-04					2.68E-04	
215				4.64E-04					3.79E-04	
220		1.50E-05		7.10E-04			1.08E-05		5.79E-04	
225		3.75E-05		1.08E-03			2.69E-05		8.81E-04	
230		7.50E-05		1.55E-03			5.39E-05		1.26E-03	
235		9.25E-05		2.09E-03	1.19E-04		6.65E-05		1.71E-03	8.38E-05
240		2.00E-04		2.47E-03	6.76E-04		1.44E-04		2.02E-03	4.76E-04
245		3.85E-04		2.74E-03	1.98E-03		2.76E-04		2.23E-03	1.39E-03
250		8.80E-04		2.84E-03	3.52E-03		6.32E-04		2.32E-03	2.48E-03
255	1.00E-05	1.87E-03		2.70E-03	4.93E-03	9.18E-06	1.35E-03		2.20E-03	3.47E-03
260	5.88E-04	3.80E-03		2.42E-03	6.92E-03	5.40E-04	2.73E-03		1.97E-03	4.88E-03
265	1.81E-03	5.46E-03		1.68E-03	7.54E-03	1.66E-03	3.92E-03		1.37E-03	5.31E-03
270	3.98E-03	6.06E-03		1.12E-03	9.32E-03	3.66E-03	4.35E-03		9.17E-04	6.57E-03
275	5.88E-03	5.30E-03		6.38E-04	1.23E-02	5.40E-03	3.81E-03		5.21E-04	8.69E-03
280	7.30E-03	3.81E-03		3.45E-04	1.31E-02	6.71E-03	2.74E-03		2.82E-04	9.24E-03
285	8.86E-03	2.11E-03		1.83E-04	1.31E-02	8.14E-03	1.52E-03		1.49E-04	9.22E-03
290	8.90E-03	1.03E-03		1.23E-04	1.19E-02	8.17E-03	7.38E-04		1.00E-04	8.39E-03
295	1.09E-02	4.80E-04		5.13E-05	1.07E-02	1.00E-02	3.45E-04		4.19E-05	7.53E-03
300	1.21E-02	2.08E-04	5.33E-05		9.05E-03	1.11E-02	1.49E-04	3.64E-05		6.37E-03
305	1.40E-02	9.50E-05	1.82E-03		7.64E-03	1.29E-02	6.82E-05	1.24E-03		5.38E-03
310	1.50E-02	5.25E-05	1.60E-03		6.13E-03	1.38E-02	3.77E-05	1.09E-03		4.32E-03
315	1.23E-02	1.50E-05	9.06E-04		4.96E-03	1.13E-02	1.08E-05	6.19E-04		3.49E-03
320	1.43E-02	5.00E-06	2.08E-05		3.77E-03	1.31E-02	3.59E-06	1.42E-05		2.65E-03

Table 40 - (Cont'd) Comparison of On-Orbit Version 2 and Version 3 NOE Functions

$\lambda$ (nm)	Version 2 (Photoevents / Photon)					Version 3 (without door mirror) (Photoevents / Photon)				
	Tracker	PC-1	PC-2	PC-3	PC-4	Tracker	PC-1	PC-2	PC-3	PC-4
325	1.79E-02				2.65E-03	1.64E-02				1.88E-03
330	1.74E-02				1.75E-03	1.59E-02				1.23E-03
335	1.52E-02				9.85E-04	1.40E-02				6.94E-04
340	1.12E-02				4.12E-04	1.03E-02				2.90E-04
345	1.47E-02				1.19E-04	1.36E-02				8.38E-05
350	1.71E-02				3.22E-06	1.58E-02				2.27E-06
355	1.90E-02					1.84E-02				
360	1.87E-02					1.72E-02				
365	1.87E-02					1.72E-02				
370	1.82E-02					1.67E-02				
375	1.80E-02					1.65E-02				
380	1.86E-02					1.71E-02				
385	1.91E-02					1.75E-02				
390	1.83E-02					1.68E-02				
395	1.38E-02					1.73E-02				
400	1.88E-02					1.73E-02				
405	1.79E-02					1.64E-02				
410	1.81E-02					1.66E-02				
415	1.64E-02					1.51E-02				
420	1.64E-02					1.51E-02				
425	1.64E-02					1.51E-02				
430	1.61E-02					1.48E-02				
435	1.39E-02					1.28E-02				
440	1.10E-02					1.01E-02				
445	1.79E-03					1.65E-03				
450	8.75E-05					8.04E-05				

UVPI data tapes were delivered to the SDIO data centers with pixel values reported in units of photoevents per second. This intermediate result, which is used directly to estimate photon shot noise but must be further processed to get useful radiometric results, must also be revised based on definitive sparse field analysis altering gain conversion factors. Since the gain conversion factor does not depend on the door mirror reflectivity, the same conversion factor is used for both with and without door mirror cases. Table 41 shows the conversion factors necessary to revise both plume- and tracker-camera photoevent rates from a version 2 to a version 3 basis.

Table 41 - Factors to Convert Photoevent Rate from a Version 2 to a Version 3 Basis

Camera	Multiplicative Conversion Factor (Version 2 to Version 3)
Tracker	1.15
Plume	1.55

The version 2 and version 3 overall UVPI responsivity, with units of DN per photon, can now be compared by multiplying the net quantum efficiency at a given wavelength by the gain conversion factor at a given gain step. Table 42 shows the results.

Table 42 - Comparison of Version 2 and 3 Total Responsivity

Filter	$\lambda$ (nm)	Gain Step	Version 2 (DN / Photon)	Version 3 (DN / Photon)	Percent Change
Tracker	390	15	2.21	2.34	5.9
PC-1	280	13	.547	.608	11.2
PC-2	310	13	.230	.242	5.2
PC-3	265	13	.241	.304	26.1
PC-4	305	13	1.10	1.19	8.9

The ratio of the fourth and fifth column values in Table 42 for a given camera and spectral filter is independent of gain step and wavelength. Also, since the shape of the version 2 and version 3 NQE curves without the door mirror are identical, the ratio of version 2 and version 3, without the door mirror, total responsivity is independent of the spectral energy distribution of the source. Therefore, all radiometric results (such as radiant intensity and radiance of rocket plumes) presented in UVPI reports for observations that did not involve the door mirror can be easily revised from version 2 to version 3 by multiplying by a simple filter-dependent conversion factor. The factors, which are the ratio of total responsivities shown in Table 42, are shown in Table 43.

The situation is more complicated for observations using the door mirror. Since the door mirror reflectivity is wavelength dependent, the shape of the version 3 NQE functions used for door mirror observations is slightly different from the shape of the version 2 NQE functions. The amplitude of the functions is nearly identical, however. Consequently, the conversion factors from version 2 to version 3 (with door mirror) are approximately equal to 1.0 with a slight dependence on the spectral energy distribution of the source. The conversion factors must be calculated on a case-by-case basis, and results for two typical cases are shown in Table 44. In general, the source spectrum dependence is insignificant for all filters except PC-3.



Table 43 - Factors to Revise Radiometric Values from a Version 2 to a Version 3  
(Without Door Mirror) Basis

Spectral Filter	Multiplicative Radiometric Conversion Factor (version 2 to version 3 without door mirror)
Tracker	.944
PC-1	.900
PC-2	.950
PC-3	.793
PC-4	.924

Tables 43 and 44 show that the conversion factors relating version 2 and version 3 total responsivity are in the 0.95 to 0.79 range for observations that do not use the UVPI door mirror, and are approximately equal to 1 for observations with the door mirror. These conversion factors can be used to revise version 2 radiometric results published in UVPI rocket plume reports (observed without the door mirror); to revise nadir viewing radiance results (observed without the door mirror); and to revise radiometric results for night glow, aurora, and day limb (observed with the door mirror). It is not surprising that the factors for converting from version 2 based to version 3 with door mirror based values are nearly one because the version 2 calibration was established using inflight measurements, but overlooking the effect of the spectral dependence of the door mirror's reflectivity. The factors for converting from version 2-based to version 3 without door mirror-based values given in Table 44 approximately parallel the spectral dependence of the door mirror's reflectivity shown in Fig. 53.

Table 44 - Factors to Revise Typical Radiometric Values from a Version 2  
to a Version 3 (With Door Mirror) Basis

Spectral Filter	Multiplicative Radiometric Conversion Factor (version 2 to version 3 with door mirror)	Multiplicative Radiometric Conversion Factor (version 2 to version 3 with door mirror)
	Flat Source Spectrum	5900 K Blackbody Source
Tracker	1.0	1.0
PC-1	1.0	.99
PC-2	1.0	1.0
PC-3	1.0	.96
PC-4	1.0	.99

## 7. SUMMARY

The purpose of this report is to describe the procedures followed in calibrating and characterizing the UVPI, to present final response functions for data reduction, and to provide conversion constants useful for revising UVPI data tapes and rocket reports. Major results are scattered throughout the report and may be difficult to separate from important, but secondary, details. A summary of primary results may prove useful. The summary will cover three major areas:

- final UVPI response functions;
- estimated errors in response functions; and
- conversion constants to revise UVPI data tapes and rocket plume reports.

The raw image data transmitted from the satellite is in the form of arrays of 8-bit binary numbers  $Q_k$  representing the intensity of light falling on the  $k$ th pixel of the CCD. These  $Q_k$  are converted into the number of photoevents,  $P_k$  occurring at the corresponding photocathode location during the image integration time. From section 2.2:

$$P_k = \frac{1}{G_k} \cdot Q_k = \frac{1}{G_k} \left[ \frac{Q_k - D_k}{U_k} \right] \quad (\text{photoevents}), \quad (36)$$

where

- $G_k$  is the gain conversion factor for gain step  $g$ , i.e., the value of  $Q_k$  for a single photoevent, assumed to be the same for all pixels  $k$ ;
- $D_k$  is the estimated dark value for the  $k$ th pixel;
- $U_k$  is the estimated nonuniformity correction factor for the  $k$ th pixel; and
- $Q_k$  is the normalized DN value after dark field subtraction and normalization for non-uniformities.

The pulse height distribution from the image intensifier will cause noninteger values for  $P_k$ . Hence,  $P_k$  values are treated as continuous variables. The conversion of CCD response peaks to integral photoevent counts is possible only for those images where the combination of the signal level and the instrument gain step are such that the probability of having overlapping photoevents is low.

The  $D_k$  are, in general, pass specific and were delivered with UVPI data tapes. As discussed in Section 3.1, a single nonuniformity matrix was delivered to be used in the calibration of all plume-camera images. Based on many observations using all four plume-camera filters, it is clear that spatial nonuniformities in the phosphor, MCP, photocathode, and CCD stay essentially constant throughout a given observation pass, and for all passes. However, nonuniformities associated with the filters themselves vary slightly in position. Therefore, filter-dependent blemishes, which change position unpredictably, are not included in the matrix.

The final version 3 gain conversion factors  $G_k$  were presented in Section 5.1, and are reproduced in Table 45.

To revise UVPI data tape and rocket plume report  $P_k$  values derived by using version 2 of the UVPI calibration to more accurate version 3 values, multiply the data tape and plume report values by the factors shown in Table 46, as discussed in Section 6.3.

Table 45 - Summary of Final, Version 3, Gain Conversion Factors

Plume Camera		Tracker Camera	
Gain Step	$G_g$ (DN/PE)	Gain Step	$G_g$ (DN/PE)
0	4.171E-02	0	2.199E-03
1	5.735E-02	1	4.227E-03
2	1.043E-01	2	9.131E-03
3	1.616E-01	3	1.928E-02
4	2.607E-01	4	4.025E-02
5	5.840E-01	5	9.199E-02
6	1.470E+00	6	1.725E-01
7	3.533E+00	7	3.230E-01
8	7.928E+00	8	7.068E-01
9	1.670E+01	9	1.380E+00
10	3.584E+01	10	2.655E+00
11	6.144E+01	11	5.631E+00
12	1.199E+02	12	1.172E+01
13	2.220E+02	13	2.937E+01
14	3.420E+02	14	5.265E+01
15	4.527E+02	15	1.395E+02

Table 46 - Factors to Convert Photoevent Rate from a Version 2 to a Version 3 Basis

Camera	Multiplicative Conversion Factor
Tracker	1.15
Plume	1.55

Errors introduced in the derivation of  $P_k$  from measured DN values fall into three categories:

- gain conversion factor estimate errors;
- dark field estimate errors; and
- use of incorrect nonuniformity matrix normalization for tracker-camera images transmitted at the normal 5 Hz rate.

The gain conversion factor errors, discussed in section 5.3, are summarized in Table 47. The values in the table actually represent errors in the total instrument responsivity, DN per photon. It is convenient to associate the errors entirely with the gain conversion factors, since this allows photoevent values delivered on UVPI data tapes to be corrected directly. It should be noted, however, that technically the error estimates shown should be applied to irradiance values derived from UVPI measurements, not to photoevents alone.

Table 47 - Summary of Estimated Error in  $G_k^{-1}$  for Plume and Tracker Cameras

Camera/Filter	Estimated Error in $1/G_k$
Plume, Filter 1	10.5%
Plume, Filter 2	15.9%
Plume, Filter 3	9.9%
Plume, Filter 4	13.5%
Tracker	15.6%

The error in  $P_k$  due to errors in the dark field estimate was discussed in Section 3.1. Some of the UVPI observations did not include adequate dark field measurements and, therefore, must be calibrated by using dark field estimates. An average dark field, based on data from many observations, is used as an estimate in such cases, introducing an error that is summarized in Table 48. This error is insignificant in most cases and, in particular, the  $P_k$  values presented in UVPI rocket plume reports are not affected.

Table 48 - Summary of Estimated Error in Calibrated Data From Dark Field Uncertainty

Errors Applicable to Passes With Inadequate Dark Field Measurements		
Gain Step	Estimated Plume Camera 1 $\sigma$ Error (PE/s)	Estimated Tracker Camera 1 $\sigma$ Error (PE/s)*
0	$8.61 \times 10^1$	$6.68 \times 10^3$
1	$6.28 \times 10^1$	$3.48 \times 10^3$
2	$3.46 \times 10^1$	$1.61 \times 10^3$
3	$2.23 \times 10^1$	$7.63 \times 10^2$
4	$1.37 \times 10^1$	$3.65 \times 10^2$
5	6.17	$1.60 \times 10^2$
6	2.45	$8.52 \times 10^1$
7	1.02	$4.55 \times 10^1$
8	$4.54 \times 10^{-1}$	$2.08 \times 10^1$
9	$2.15 \times 10^{-1}$	$1.06 \times 10^1$
10	$1.00 \times 10^{-1}$	5.54
11	$5.86 \times 10^{-2}$	2.61
12	$3.00 \times 10^{-2}$	1.26
13	$1.62 \times 10^{-2}$	$5.00 \times 10^{-1}$
14	$1.05 \times 10^{-2}$	$2.80 \times 10^{-1}$
15	$7.96 \times 10^{-3}$	$1.06 \times 10^{-1}$

\*Assuming 33.3-ms integration time.

Section 3.1 discussed the error in tracker-camera normal image rate images for which the  $P_k$  rate values delivered on UVPI data tapes need to be adjusted because of incorrect nonuniformity normalization. The tracker-camera normal image rate nonuniformity matrix used caused a systematic 4% error in the tracker camera normal image rate images delivered on UVPI data tapes. Therefore, all tracker-camera normal image rate calibrated values delivered on UVPI data tapes should be reduced by 4%. Most tracker camera rocket plume data are collected in zoom image rate, and thus are not affected by this error.

After  $P_k$  values have been derived, conversion to obtain radiometric values describing the source emission requires the wavelength-dependent calibration function, the net quantum efficiency, for the UVPI. Derivation of on-orbit net quantum efficiency functions is discussed in Section 5.2. The final version 3 net quantum efficiency functions for observations with the door mirror (nightglow, aurora, limb, stars) and without the door mirror (rocket plumes, nadir viewing) are summarized in Table 49.

Table 49 - Summary of Version 3 Net Quantum Efficiency Functions

$\lambda$ (nm)	Version 3 (with door mirror) (Photoevents / Photon)					Version 3 (without door mirror) (Photoevents / Photon)				
	Tracker	PC-1	PC-2	PC-3	PC-4	Tracker	PC-1	PC-2	PC-3	PC-4
195				2.11E-05					5.03E-05	
200				4.81E-05					1.05E-04	
205				8.75E-05					1.77E-04	
210				1.42E-04					2.68E-04	
215				2.15E-04					3.79E-04	
220		6.51E-06		3.50E-04			1.08E-05		5.79E-04	
225		1.73E-05		5.64E-04			2.69E-05		8.81E-04	
230		3.65E-05		8.56E-04			5.39E-05		1.26E-03	
235		4.75E-05		1.22E-03	5.99E-05		6.65E-05		1.71E-03	8.38E-05
240		1.08E-04		1.51E-03	3.57E-04		1.44E-04		2.02E-03	4.76E-04
245		2.18E-04		1.76E-03	1.10E-03		2.76E-04		2.23E-03	1.39E-03
250		5.26E-04		1.93E-03	2.06E-03		6.32E-04		2.32E-03	2.48E-03
255	7.84E-06	1.15E-03		1.88E-03	2.96E-03	9.18E-06	1.35E-03		2.20E-03	3.47E-03
260	4.78E-04	2.41E-03		1.74E-03	4.31E-03	5.40E-04	2.73E-03		1.97E-03	4.88E-03
265	1.49E-03	3.52E-03		1.23E-03	4.76E-03	1.66E-03	3.92E-03		1.37E-03	5.31E-03
270	3.33E-03	3.96E-03		8.35E-04	5.97E-03	3.66E-03	4.35E-03		9.17E-04	6.57E-03
275	4.96E-03	3.50E-03		4.78E-04	7.98E-03	5.40E-03	3.81E-03		5.21E-04	8.69E-03
280	6.21E-03	2.53E-03		2.61E-04	8.55E-03	6.71E-03	2.74E-03		2.82E-04	9.24E-03
285	7.56E-03	1.41E-03		1.39E-04	8.56E-03	8.14E-03	1.52E-03		1.49E-04	9.22E-03
290	7.62E-03	6.88E-04		9.36E-05	7.82E-03	8.17E-03	7.38E-04		1.00E-04	8.39E-03
295	9.35E-03	3.22E-04		3.91E-05	7.03E-03	1.00E-02	3.45E-04		4.19E-05	7.53E-03
300	1.04E-02	1.40E-04	3.41E-05		5.97E-03	1.11E-02	1.49E-04	3.64E-05		6.37E-03
305	1.22E-02	6.43E-05	1.17E-03		5.07E-03	1.29E-02	6.82E-05	1.24E-03		5.38E-03
310	1.31E-02	3.53E-05	1.04E-03		4.10E-03	1.38E-02	3.77E-05	1.09E-03		4.32E-03
315	1.07E-02	1.02E-05	5.89E-04		3.32E-03	1.13E-02	1.08E-05	6.19E-04		3.49E-03
320	1.25E-02	3.41E-06	1.35E-05		2.52E-03	1.31E-02	3.59E-06	1.42E-05		2.65E-03

Table 49 - (Cont'd) Summary of Version 3 Net Quantum Efficiency Functions

$\lambda$ (nm)	Version 3 (with door mirror) (Photoevents / Photon)					Version 3 (without door mirror) (Photoevents / Photon)				
	Tracker	PC-1	PC-2	PC-3	PC-4	Tracker	PC-1	PC-2	PC-3	PC-4
325	1.56E-02				1.78E-03	1.64E-02				1.88E-03
330	1.52E-02				1.17E-03	1.59E-02				1.23E-03
335	1.33E-02				6.60E-04	1.40E-02				6.94E-04
340	9.83E-03				2.76E-04	1.03E-02				2.90E-04
345	1.29E-02				7.98E-05	1.36E-02				8.38E-05
350	1.50E-02				2.16E-06	1.58E-02				2.27E-06
355	1.75E-02					1.84E-02				
360	1.63E-02					1.72E-02				
365	1.63E-02					1.72E-02				
370	1.59E-02					1.67E-02				
375	1.562E-02					1.65E-02				
380	1.615E-02					1.71E-02				
385	1.649E-02					1.75E-02				
390	1.579E-02					1.68E-02				
395	1.625E-02					1.73E-02				
400	1.627E-02					1.73E-02				
405	1.543E-02					1.64E-02				
410	1.562E-02					1.66E-02				
415	1.42E-02					1.51E-02				
420	1.42E-02					1.51E-02				
425	1.41E-02					1.51E-02				
430	1.38E-02					1.48E-02				
435	1.19E-02					1.28E-02				
440	9.40E-03					1.01E-02				
445	1.53E-03					1.65E-03				
450	7.48E-05					8.04E-05				

UVPI observations of rocket plumes were made without using the door mirror. As discussed in section 6.3, to revise UVPI rocket report radiometric values such as radiant intensity and radiance derived by using version 2 of the UVPI calibration to the more accurate version 3 values, the radiometric values in the rocket plume reports [8-11] should be multiplied by the factors shown in Table 50. Application of these conversion factors does not change the trends and conclusions presented in the rocket plume reports.

Table 50 - Factors to Revise UVPI Rocket Plume Report Radiometric Values from a Version 2 to a Version 3 (Without Door Mirror) Basis

Spectral Filter	Multiplicative Radiometric Conversion Factor (version 2 to version 3 without door mirror)
Tracker	.944
PC-1	.900
PC-2	.950
PC-3	.793
PC-4	.924

Observations made using the door mirror, such as aurora, nightglow, dayglow, and stars, must be corrected on a case by case basis since correction factors depend on source spectral shape. In general, as discussed in Section 6.3, the correction factors are very nearly equal to 1.0 in most cases.

#### REFERENCES

1. H.W. Smathers, D.M. Horan, J.G. Cardon, E.R. Malaret, M.R. Corson and J.E. Brandenburg, "Ultraviolet Plume Instrument Description and Plume Data Reduction Methodology," NRL Report 9531, May 1993.
2. H.W. Smathers, D.M. Horan, L.H. Reynolds, W. Ramsey and H.D. Wolpert, "Design and Description of the Ultraviolet Plume Instrument (UVPI)," *Proc. SPIE* **1158**, 196 (1989).
3. H.W. Smathers, G.R. Carruthers, W. Ramsey, G. Steiner and W. Louissaint, "Calibration and Performance of the Ultraviolet Plume Instrument (UVPI)," *Proc. SPIE* **1158**, 212 (1989).
4. A. Papoulis, *Probability, Random Variables and Stochastic Processes* (McGraw Hill, New York, 1965).
5. G.R. Carruthers, "Radiometric Imaging in the Ultraviolet," *Proc. SPIE*, **1109**, 2 (1989).
6. R. Gabliardi, *Introduction to Communications Engineering* (John Wiley & Sons, 1978).
7. C.L. Wyatt, *Electro-Optical System Design for Information Processing* (McGraw Hill, New York, 1991).
8. H.W. Smathers, D.M. Horan, J.G. Cardon, E.R. Malaret, M. Singh, T. Sorensen, P.M. Laufer, M.R. Corson, J.E. Brandenburg, J.A. McKay, and R.R. Strunce, Jr., "UVPI Imaging From the LACE Satellite, The Strypi Rocket Plume," NRL Report 9526, July 15, 1993.
9. H.W. Smathers, D.M. Horan, J.G. Cardon, E.R. Malaret, L. Perez, T. Tran, J.E. Brandenburg, and R.R. Strunce, Jr., "UVPI Imaging from the LACE Satellite, The Starbird Rocket Plume," NRL Report 9546, August 18, 1993.

10. H.W. Smathers, D.M. Horan, J.G. Cardon, E.R. Malaret, J.E. Brandenburg, R. Campion, and R.R. Strunce, Jr., "UVPI Imaging From the LACE Satellite, The Nihka Rocket Plume," NRL Report 9537, July 12, 1993.
11. H.W. Smathers, D.M. Horan, J.G. Cardon, E.R. Malaret, L. Perez, T. Tran and J.E. Brandenburg, "UVPI Imaging from the LACE Satellite, The Low-Cost Launch Vehicle (LCLV) Rocket Plume," NRL Report 9545, September 24, 1993.
12. H.L. VanTrees, *Detection, Estimation, and Modulation Theory* (John Wiley & Sons, New York, 1968), pp. 36-39.
13. L. Reynolds, "Documenting the UVPI Spectral Properties," Loral Electro-Optical Systems Memo UVPI-0633, December, 1991.
14. G. Sonneborn, N.A. Oliverson, C.L. Imhoff, R.E. Pitt, and A.V. Holm, "IUE Observing Guide," IUE NASA Newsletter No. 32, p.1 (1987).
15. A.D. Code, A.V. Holm and R.L. Bottemiller, "Ultraviolet Photometry from the Orbiting Astronomical Observatory XXXIV, Filter Photometry of 531 Stars of Diverse Types," *Astrophys. J. Suppl.* **43**, 501 (1980).
16. M. Breger, "Catalog of Spectrophotometric Scans of Stars," *Astrophys. J. Suppl.* **32**, 7-87 (1976).
17. W.L. Wolfe and G.J. Zissis, eds., *The Infrared Handbook* (Environmental Research Institute of Michigan, 1978).
18. R.H. Kingston, *Detection of Optical and Infrared Radiation* (Springer-Verlag, New York, 1978), pp. 43-51.
19. G. Romick, D. Anderson, C. Chase, and P. Murphy, "UVPI Plume Camera Daytime Evaluation," Johns Hopkins University Applied Physics Laboratory, September 1992.
20. H.W. Smathers, D.M. Horan, M. Singh, J.G. Cardon, D.F. Bakeris and R.A. Swanson, "Satellite Observations with the UVPI Instrument," *Proc. SPIE* **1764**, 36 (1992).



## GLOSSARY

A/D	-	analog-to-digital
AGC	-	automatic gain control
APL	-	Applied Physics Laboratory, Johns Hopkins University
CCD	-	charge-coupled device
CFC	-	camera frame controller
DN	-	digital number
FOV	-	field of view
FPA	-	focal plane array
FWHM	-	full-width-half-maximum
Hz	-	Hertz
ICCD	-	intensified charge-coupled device
IUE	-	International Ultraviolet Explorer
LACE	-	Low-power Atmospheric Compensation Experiment
Mbps	-	megabits per second
MCP	-	microchannel plate
MTF	-	modulation transfer function
NER	-	noise equivalent radiance
NQE	-	net quantum efficiency
NRL	-	Naval Research Laboratory
OAO	-	Orbiting Astronomical Observatory
P-C-N	-	plume camera filter, $N = 1, 2, 3, 4$
PE	-	photoevent
PFA	-	probability of false alarm
PSF	-	point spread function
SDIO	-	Strategic Defense Initiative Organization
SNR	-	signal-to-noise ratio
UVPI	-	Ultraviolet Plume Instrument

END  
FILMED

DATE:

10-93

DTIC